



Glass-ceramic engineering: tailoring the microstructure and properties

Christian Rüssel^a, Wolfgang Wisniewski^{b,c,*}

^a Otto-Schott-Institut, Jena University, Fraunhoferstr. 6, 07743 Jena, Germany

^b Slovenian National Building and Civil Engineering Institute (ZAG), Dimičeva 12, 1000 Ljubljana, Slovenia

^c Institute of Materials Science and Engineering, Chemnitz University of Technology, Erfenschlager Str. 73, 09125 Chemnitz, Germany

ABSTRACT

Traditionally, glass-ceramics are inorganic non-metallic materials obtained by the controlled crystallization of a glass. A modern definition has widened this class of materials to solid materials containing at least one glassy and one crystalline phase. The glass is usually obtained by quenching a melt. Re-heating it to a temperature slightly above the glass transition temperature allows nucleation while an often applied second annealing step at a higher temperature causes most of the crystal growth. As in most materials, the composition and the microstructure of glass-ceramics widely governs their properties. The morphology, i.e., size, and aspect ratio of the crystal phases is of special significance and depends on the crystal structure and the occurring growth mechanism. The morphology is also affected by the chemical composition and the temperature/time schedule of the crystallization process, here components of minor concentrations can have a great effect. This review addresses the effects of nucleating agents, phase separation, crystal orientation alignment and stress introduction as tools to tailor the properties of glass-ceramic materials. Future developments in the field of glass-ceramics are discussed.

1. Introduction

Glass-ceramics [1] are solid materials containing at least one glassy and one crystalline phase. Extremes of this denomination are, e.g., laser crystallized glasses, where the vol% of the crystalline phase can be minimal, or fully crystalline materials grown from bulk glasses where an amorphous component, i.e., residual glass, has not been proven so far [2–13]. Since the pioneering work of Stookey in the 1950s [14], glass-ceramics have continuously been developed into a versatile group of materials [1]. The more traditional group of “classic glass-ceramics” are produced by first preparing a homogeneous glass, which is then heated to a temperature slightly above (up to a few 10 K) the glass transition temperature (T_g) where crystal nucleation occurs in many cases and the nucleation rate is highest [15,16]. The formed critical nuclei immediately start to grow [17–19] and the temperature is subsequently often increased to accelerate crystal growth. This temperature is either kept constant or undergoes further changes until the intended degree of crystallinity is reached [15–17]. A temperature increase after the nucleation step also increases the radius of the critical nucleus, meaning any crystals which did not grow beyond this radius are dissolved again [17,20,21].

The technologically most important variation of this process is currently to powder the glass, process the powder by, e.g., pressing it into an appropriate shape, and then sintering the specimen to produce “sintered glass-ceramics” [22–28]. A related approach is to produce glass microspheres, some of which show a nearly complete crystallization during production [22], and subsequently sinter them together [22–25,29]. Sintering should lead to a first densification while further crystal nucleation and growth take place after a

* Corresponding author at: Institute of Materials Science and Engineering, Chemnitz University of Technology, Erfenschlager Str. 73, 09125 Chemnitz, Germany.

E-mail address: wolfgang.wisniewski@mb.tu-chemnitz.de (W. Wisniewski).

fully (or nearly) dense body is obtained. Producing sintered glass-ceramics requires a careful optimization of the chemical composition, the grain size and grain size distribution, the shaping procedure and the temperature/time schedule.

It is noteworthy that the early work of Stookey [14] already featured nucleation achieved by a photochemical process in which Ce^{3+} and Ag^+ , both homogeneously dissolved in the glass, were irradiated by UV light and reacted to Ce^{4+} and metallic silver. The applied thermal treatment then led to the formation of silver clusters which acted as nucleation centres throughout the glass.

Glass-ceramics have become widely used as low thermal expansion materials for various applications such as cook top panels, telescope mirror blanks and various components in optics and photonics [30–33]. Machinable glass-ceramics, most of them containing mica or other phyllo(alumo)silicates, have been commercially available for decades [34–36] and can be rapidly machined by conventional diamond or hard metal tools. They are, e.g., utilized as rapid prototyping materials [37] or biocompatible bone replacement materials in plastic surgery [38–40].

Other glass-ceramics are applied as tooth replacement materials with tailored optical properties (adaptable translucency and colour to match the teeth of a patient) [41–44] and mechanical properties (high strength, high fracture toughness) [45–47]. In the past decade, a large variety of optical materials based on glass crystallization have been reported showing interesting luminescence [48–52] and up conversion [53–55] properties. The microstructure of these glass-ceramics was tailored using the formation of self-assembled diffusion barriers which hinder the growth of crystals beyond diameters of more than few ten nm [56–62]. This can minimize light scattering and the resulting glass-ceramics are transparent for visible and/or near infrared light [63,64].

Although not the focus of this review, an interesting field is the possibility to create anisotropic materials which show aligned crystals [65–68]. Nucleation in only a small part of a glass, e.g., at a surface, enables not only highly anisotropic crystal growth but also polarity selected crystal growth [69–75]. Among anisotropic growth, special attention must be paid to laser driven crystallization [76–82].

Another interesting field are glass-ceramics with special coefficients of thermal expansion (CTE). These can, e.g., be used as seals to join ceramics and/or metals stable at temperatures above 800 °C [83–88] and, e.g., applied in high temperature fuel cells [27,83–88].

The precipitation of crystalline phases whose CTEs do not match that of the residual glass enables the formation of internal stresses during cooling after crystallization and may widely govern the mechanical strength and fracture toughness [89]. Here, crystalline phases with CTEs much larger than that of the residual glass enable a tremendous improvement of the mechanical properties and even the preparation of glass-ceramics with mechanical strengths of more than 1 GPa [46,47]. These effects can be enhanced further by crystallizing phases which show phase transitions accompanied by a notable volume decrease during cooling [89]. This can increase the tensile stresses caused by the crystalline inclusion even more than through a mismatch in the CTEs. Recent studies on solid solutions whose phase transition temperatures and CTEs can be varied in a wide range through comparatively small changes of the chemical composition [83,90–92] should enable a more accurate tailoring of such stresses and hence the mechanical properties or the resulting glass-ceramics.

Tailoring glass-ceramics and their properties primarily depends on the glass composition, the crystallized phases and the formed microstructure. The size and the morphology of the precipitated crystals play a decisive role; it is, e.g., essential whether nanocrystals [49,56,57,59,60,62] are formed, the crystals assume approximately spherical, needle or plate-like shapes or the microstructure is formed by viscous fingering or dendritic growth [93–98]. Of course, the formed crystal lattice and its properties play an important part, but special attention must be paid to the morphology and the arrangement of the crystals amongst each other. Here interlocking also plays a crucial role, e.g., with respect to crack propagation and fracture toughness [99–102]. One important advantage of glass-ceramics over sintered ceramics is that the primary glass is usually transparent and hence can be inspected using optical/visual methods, meaning defects can be identified before crystallization.

Up into the 1990s, it was often assumed that “controlled crystallization” can only be achieved if a glass melt free of nucleation agents first undergoes a phase separation [103,104], i.e., the homogeneous glass melt forms two liquid phases with different chemical compositions. Such a phase separation indeed notably affects the crystallization process; first, the chemical composition changes and hence, the glass forming ability in one of the two phases decreases, giving rise to nucleation and subsequent crystal growth in it. Secondly, crystal growth usually stops or notably decelerates when the boundaries of the respective liquid are reached. Following this mechanism, crystallizing droplets remain embedded in an amorphous matrix [105–110] and the size and shape of the crystalline body are restricted to those of the former droplet [111]. If there is only one dominant nucleus per droplet, the crystal shape is nearly spherical and almost independent from the occurring mechanism of crystal growth. Droplet phase separation can enable to precipitate crystals which would not crystallize from the homogeneous parent glass according to the phase diagram. Nevertheless, nano crystals can also be obtained in the case of phase separated glasses with interpenetrating structures [56].

The bulk of the literature concerning crystal nucleation and growth in glasses is focused on the so called “Classical Nucleation Theory” (CNT) [112,113], which is a purely thermodynamic approach and furthermore mostly related to isochemical systems where the chemical composition of the glass and crystal are identical. By analogy, crystal growth kinetics have predominantly been reported for isochemical systems. As all industrially produced glass-ceramics and most glass-ceramics with advantageous properties currently result from non-isochemical compositions, the above-mentioned considerations are of limited value when designing glass-ceramics with tailored properties. The isochemical systems considered by the classical theories common in glass science do not show phenomena such as phase separation, chemical gradients or crystal growth velocities which depend on the crystallographic directions.

One huge field in glass-ceramics research are bioactive compositions for biomedical applications [114,115] based on silicates or phosphates. These materials will not be discussed here as their microstructure is secondary to their application which mainly depends on their chemical composition. There is much literature in this field including some recent reviews [114,115].

This review discusses tools useful when designing glass-ceramics with advantageous properties, many of which were developed in the last two decades. A number of experimental/analytical methods were decisive for the progress in glass-ceramic research during this

time. First, the improvement of transmission electron microscopy (TEM), especially with aberration corrected microscopes, enabled to quantitatively analyse heterogeneities down to the sub nm range. This enabled to detect shells formed around growing crystals and the epitaxial growth of crystals on nm sized nuclei [116] using selected area electron diffraction (SAED), energy dispersive X-ray spectroscopy (EDXS) and extended electron energy loss fine structure spectroscopy (EXELFS). It also enabled to lower the radiation damage of sensitive, e.g., Li containing samples, which led to severe misinterpretations in the past. Second, the development of electron backscatter diffraction (EBSD) up to fully automated indexing, predominantly carried out in a scanning electron microscope (SEM), enables to scan samples and record millions of EBSD-patterns within one scan and a lateral resolution down to some ten nm. The significant information depth of these measurements is usually less than 80 nm [117,118]. Every recorded pattern contains crystallographic information concerning the analysed region, allowing, e.g., maps of the crystal orientations but also phase identification [119]. This not only enables to visualize the distribution of different crystal phases, but also a very precise texture analysis, e.g., at surfaces, and the proof of epitaxial relationships. Advanced electron microscopy is complemented by techniques using synchrotron radiation: anomalous small angle X-ray scattering (ASAXS) enables conclusions on nm sized inclusions, core shell structures and the attributed chemical compositions. X-ray absorption spectroscopy (XAS) allows conclusions, e.g., on the incorporation of all components, and their coordination numbers, into the glass and can monitor changes during the formation of nuclei, hence contributing towards understanding the nucleation process.

Abbreviations

AGSS åkermanite gehlenite solid solutions
 ASAXS Anomalous Small Angle X-ray Scattering
 B&W theory Brailsford and Wynblatt theory
 BFDH law Bravais-Friedel-Donnay-Harker law
 CNT Classical Nucleation Theory
 CPR Coordination Polyhedra Rule
 CTE Coefficient of Thermal Expansion
 d distance from the centre of the particle
 D diffusion coefficient
 E Young's Modulus
 EBSD Electron BackScatter Diffraction
 EDXS Energy Dispersive X-ray Spectroscopy
 EELS Electron Energy Loss Spectroscopy
 EiN Electrochemically induced Nucleation
 EXELFS Extended Electron Energy Loss Fine Structure Spectroscopy
 FEM Finite Element Method
 h Planck's constant
 I_{st} steady state nucleation rate
 IPF Inverse Pol Figure
 k_B Boltzmann's constant
 LAS lithium-alumo-silicate
 LS₂ lithium disilicate glass
 LSW theory Lifshitz, Slyozov and Wagner theory
 N_1 number of structural units per unit volume in the melt
 NMR Nuclear Magnetic Resonance
 MAS magnesium-alumo-silicate
 MAS-NMR Magic Angle Spinning Nuclear Magnetic Resonance
 m^* reduced fragility index
 P stress inside the spherical inclusion
 PBC theory Periodic Bond Chain theory
 PTR glasses Photo Thermal Refractive glasses
 r radius of the nucleus
 R radius of the inclusion
 r^* critical cluster size
 RT room temperature
 SAXS Small Angle X-ray Scattering
 SAED Selected Area Electron Diffraction
 SEM Scanning Electron Microscopy
 T_{Curie} Curie temperature
 T_g glass transition temperature
 T_l liquidus temperature
 T_t phase transition temperature
 TEM Transmission Electron Microscopy
 TTT-curves Temperature Time Transformation -curves
 U crystal growth velocity

UV ultra violet
 V_m molar volume
 XAS X-ray Absorption Spectroscopy
 YAG yttrium aluminium garnet
 ΔG Gibbs free energy for nucleus formation
 ΔG_a Gibbs free energy per unit volume
 ΔG_D Gibbs free energy for the transfer of a 'structural unit' from the melt to the crystal
 ΔG_{\max} Gibbs free energy of cluster formation
 ΔG_v Gibbs free energy change per unit volume
 ΔH_v enthalpy change per unit volume at T_l
 ΔV volume change between the two phases
 ΔV_t volume change due to a phase transition
 ϵ_r relative dielectric constant
 σ interfacial energy per unit area
 σ_r radial stress
 σ_t tangential stress
 η viscosity
 μ Poisson's ratio
 ρ density
 ξ structural order parameter
 ξ_e the equilibrium value of the structural order parameter
 $\zeta = \xi/\xi_e$

2. Crystal Morphologies and Crystal Structure

Glass crystallization is often considered to be a two-step process composed of nucleation and crystal growth. Although this approach is useful for many cases, it should always be kept in mind that these steps are not really separated processes. The number of formed nuclei in a given glass composition during thermal treatment is a function of temperature and time. The highest nucleation rates are usually achieved at temperatures 5 to 50 K above T_g . Sometimes, the nucleation rate is small during isothermal treatment, but increases with time until a steady state value is reached. During subsequent crystal growth, usually carried out at higher temperatures, the crystals often show very different crystal growth velocities along different crystallographic directions which leads to different morphologies. The growth morphology is usually not determined by thermodynamics, i.e., the different interfacial energies of different crystallographic planes (which would lead to the Wulff shape), but due to the growth kinetics. The morphology of the crystals is also affected by spatial limitations set by phase separation or by the formation of core shell structures which function as growth barriers.

2.1. Classical Nucleation Theory (CNT) and Crystal Growth Velocity

Classical Nucleation theory

The CNT is based on the thermodynamic theory of heterogeneous systems developed by J. W. Gibbs [120] and later applied to vapour condensation by M. Volmer & A. Weber [121,122] as well as R. Becker & W. Döring [123] and also to the formation of crystalline nuclei by R. Kaisew & I. N. Stranski [124] as well as D. Turnbull & J. C. Fisher [125]. G. Tammann introduced a method to determine nucleation rates applicable for glasses where nucleation is achieved during a first step of thermal treatment while a second step at higher temperatures allowed the nuclei to grow to an "observable size" so that they can be counted using microscopic techniques [126,127]. An overview on the application of the CNT to glass crystallization is given in Ref. [29], including a history of its development. The CNT is based on thermodynamics and assumes that the nucleation rate is proportional to the driving force of glass crystallization, i.e., the reaction transforming a glass melt (below its liquidus temperature T_l) to a crystal of the same chemical composition, a.k.a. the Onsager Reciprocal Relation. The following assumptions are also made: The formed clusters/nuclei are spherical, isotropic and have a discrete surface. The chemical compositions of the formed crystal and the glass melt are identical, hence also match the residual glass, and thus composition changes do not occur during crystallization. The crystal structure of the nucleus is assumed to match that of a defect free, macroscopic crystal of the same phase. Hence, the change of its Gibbs free melting energy per unit volume ΔG_v is also identical. The interface energy between crystal and melt affects the total Gibbs free energy. The Gibbs free energy required for nucleus formation ΔG is then given by Eq. (1).

$$\Delta G = \frac{4}{3}\pi r^3 \Delta G_v + 4\pi r^2 \sigma \quad (1)$$

with r is the radius of the nucleus, ΔG_v is the Gibbs free energy change per unit volume and σ is the interfacial energy per unit area.

The first term describes the thermodynamic driving force for an infinitely large crystalline phase while the second describes the interfacial energy. The relation of ΔG_v versus the radius of a small crystal shows a maximum; the attributed radius is denoted as the critical cluster size r^* in Eq. (2).

$$r^* = \frac{2\sigma}{\Delta G_v} \quad (2)$$

If the cluster size exceeds r^* , it will grow while smaller clusters will shrink. The Gibbs free energy of cluster formation ΔG_{\max} attributed to r^* is the thermodynamic barrier for nucleation and given by Eq. (3):

$$\Delta G_{\max} = \frac{16\pi}{3} \frac{\sigma^3}{\Delta G_v^2} \quad (3)$$

Usually, ΔG_v is estimated from ΔH_v , the enthalpy per unit volume at T_i , as stated in Eq. (4) [128,129].

$$\Delta G_v = \frac{\Delta H_v(T_i - T)}{T_i} + \int_T^{T_i} \Delta C_p(T) dT - T \int_T^{T_i} \frac{\Delta C_p(T)}{T} dT \quad (4)$$

Here, $\Delta C_p(T)$ is the heat capacity difference between a crystal and a glass under a constant pressure as a function of the temperature. While ΔH_v and T_i can be measured, $\Delta C_p(T)$ is usually unknown. Many publications dedicated to calculating nucleation rates usually approximate $\Delta C_p(T)$ using Eq. (5), but for some cases, like $\text{NaCa}_2\text{Si}_3\text{O}_8$ [129], $\Delta C_p(T)$ has been determined and enabled to use Eq. (4) [128].

$$\Delta G_v = \frac{\Delta H_v(T_i - T)}{T_i} \quad (5)$$

The Gibbs free energy of cluster formation ΔG_{\max} is calculated using Eq. (6):

$$\Delta G_{\max} = \frac{16\pi}{3} \frac{\sigma^3}{(\Delta G_v)^2} \quad (6)$$

The interfacial energy per unit area σ is currently very difficult to determine experimentally and hence usually unknown; it may furthermore vary and depend on, e.g., the temperature as well as the nucleus size. The steady state nucleation rate I_{st} is given by Eq. (7):

$$I_{st} = \frac{2D}{a^4} \left(\frac{\sigma}{k_B T} \right)^{1/2} \exp \left[- \frac{\Delta G_{\max}}{k_B T} \right] \quad (7)$$

Here “a” is the size of a structural unit, k_b is Planck’s constant and D the diffusion coefficient. For temperatures near and below T_g , the structural relaxation of the nucleation process is no longer negligible and the Gibbs free melting energy per unit volume ΔG_v should be modified according to Eq. (8) [130,131].

$$\Delta G_v(\zeta) = \Delta G_{v,eq} \zeta \quad (8)$$

with $\zeta = \xi/\xi_e$ and ξ =structural order parameter and ξ_e =the equilibrium value of the structural order parameter. From the Eqs. (7) and (8) follows Eq. (9):

$$I_{st}(T, t) = \frac{2D}{a^4} \left(\frac{\sigma}{k_B T} \right)^{1/2} \exp \left[- \frac{\Delta G_{\max}(T) \zeta(t)}{k_B T} \right] \quad (9)$$

A maximum in the dependency of the nucleation rate on temperature is usually observed somewhat above T_g . At the temperature of this maximum and above, the steady state nucleation rates do not deviate significantly from the CNT, if diffusion coefficients and interfacial energies are fitted to the experimental data obtained at temperatures above the maximum [131]. Hence, stress relaxation and any other possible effects do not play an important role above this maximum. There are numerous refinements of the CNT which, e. g., take experimentally observed induction periods into account [29,112,127,132-137].

“Heterogenous nucleation” is a special topic as various phenomena are referred to by this term [138-140]. The first of these to be mentioned is nucleation at the surface. Here recent analysis has shown that nuclei often show a preferred orientation, i.e., show oriented nucleation [69]. Many glass systems solely show surface crystallization. Another type of “heterogeneous nucleation” is that following a liquid-liquid phase separation. The interfacial energy between the two liquids is much smaller than that between a crystal and a glass melt [110]. The subsequent crystallization is often reported to occur after nucleation at the glass/glass interface [110]. The third type of “heterogeneous nucleation” occurs after nucleation agents were added to a glass, resulting in the crystallization of a crystalline precursor on which the desired phase will grow. It has been proposed also to apply the CNT to heterogeneous nucleation by replacing ΔG_{\max} by $\Delta G_{\max} \Phi$ (with $\Phi < 1$) [139].

Crystal growth velocity

Three principles of crystal growth are related to a certain growth model: the normal model (growth in all directions), 2D surface nucleated growth and finally growth along screw dislocations (one dimensional growth) [141,142]. The following focus will be on the normal growth and that along screw dislocations expressed by Eq. (10):

$$U = \frac{fD(T)}{\lambda} \left(1 - \exp \left(- \frac{\Delta G}{k_B T} \right) \right) \quad (10)$$

with $f \approx 1$ [142] for normal growth and $0 < f < 1$ for growth via screw dislocations. λ is the jump distance, i.e., the characteristic length of the crystal building unit (usually the molecular diameter) and $D(T)$ is the temperature dependent diffusion coefficient. Substituting $D(T)$ with Eq. (10) results in Eq. (11) where C is a constant described by $C = f k_b / (3\pi\lambda^2)$.

$$U = \frac{f k_B T}{3\pi\lambda^2 \eta} \left(1 - \exp \left(- \frac{\Delta G}{k_B T} \right) \right) = \frac{CT}{\eta} \left(1 - \exp \left(- \frac{\Delta G}{k_B T} \right) \right) \quad (11)$$

It should be noted that the Eqs. (10) and (11) are not valid for growth via 2D nucleation on a “smooth” primary crystal.

Both the nucleation rate I_n and the crystal growth velocity U show maxima at temperatures between the glass transition temperature T_g and the liquidus temperature T_l as schematically illustrated in Fig. 1 a). The most frequently investigated system with respect to its nucleation rate and crystal growth velocity is the stoichiometric lithium disilicate system. Here, the experimental studies of the groups associated with P.F. James [143,144], M.C Weinberg [145], E.D. Zanotto [146–148], K. Matisida [149] and J. Deubener [150] are to be mentioned. Fig. 1 b) shows experimental nucleation rates and crystal growth velocities in a logarithmic plot for the isochemical crystallization of glass with the stoichiometric composition of lithium disilicate ($\text{Li}_2\text{Si}_2\text{O}_5$) [143–146,150,151]. The maximum of I_{st} is usually observed around T_g (-10 K below to some 10 K above T_g) [152]. The maximum of U is at a much higher temperature but, of course, below T_l . U can be notably positive at temperatures where I_{st} has not yet dropped to infinitesimally small values. If the crystal growth velocities are noticeably high when nucleation occurs, the nuclei formed during cooling will notably grow. This is generally relevant at small cooling rates and usually not desired for the preparation of glass-ceramics. U is negative above T_l and the crystals dissolve.

The literature concerning the CNT contains numerous alterations which, e.g., take induction periods for nucleation into account. A more detailed description of the CNT is reported elsewhere (see, e.g., [29,112]) and beyond the scope of the work presented here. It should be noted that nucleation and crystal growth can never be two separated steps because formed nuclei immediately start to grow [17]. Furthermore, Eq. (11) assumes that crystal growth velocities are the same in all directions and can hence, strictly speaking, only apply to spherical crystals. Furthermore, Eq. (11) assumes that the crystal growth velocities do not depend on time which is only valid for melts of exactly the same stoichiometry as the formed crystal. Otherwise, i.e., in basically all real melts, the melt composition changes during crystallization and with it the diffusion coefficient.

2.2. Spherical Crystal Volumes

There are two principal possibilities to obtain spherically shaped crystallized volumes: either the crystal growth velocity is the same for all directions or the volume a crystal may occupy is limited to a sphere. The latter may, e.g., occur if crystallization takes place inside a droplet resulting from phase separation [111,153] as outlined below or when crystals grow in melt droplets levitating in a gas stream [154] or flying through air [22]. The CNT describes an initially formed nucleus to be spherical. It should be noted that it is experimentally very difficult to distinguish whether a crystal only a few nm in diameter is spherical or faceted, i.e., shows a polygon structure. The morphology of such crystals is best studied in glasses from which noble metal clusters such as gold or silver, typically added in concentrations from 50 ppm to 1 %, can be precipitated to then form crystals smaller than 5 nm in diameter [155,156]. Although these metallic crystals have a cubic symmetry, they are already faceted and hence their crystal growth velocity was not homogeneous in all directions. Such crystals usually assume polygon shapes during further growth, like cubes or octahedra, as it is to be expected from cubic space groups. Ideally, a maximum crystal growth velocity along the $\langle 001 \rangle$ directions leads to a cube, while a maximum growth velocity along the $\langle 111 \rangle$ directions, i.e., perpendicular to the most densely packed layers, leads to an octahedron.

In principle, a spherical morphology is favourable if a crystal is only a few nm in size, as a sphere minimizes the interfacial energy between the crystal and its matrix. With an increasing size, and hence a decreasing percentage of surface atoms, this interfacial energy plays a decreasingly important part. Noble metal nanoparticles embedded in glass are of high importance because they act as effective

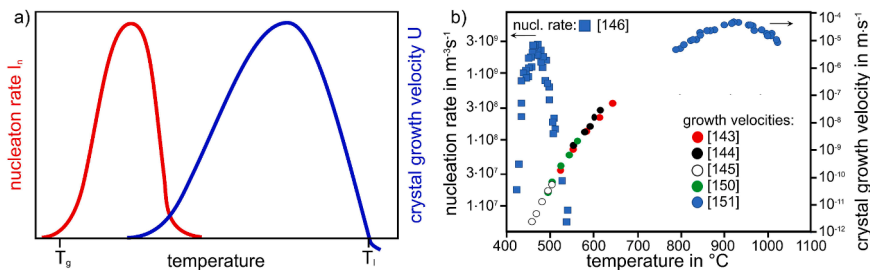


Fig. 1. Steady state nucleation rate and crystal growth velocity a) Schematic illustration of the steady state nucleation rate, I_{st} , and crystal growth velocity, U , as a function of the temperature. Please note that nucleation is possible below T_g , while crystals always dissolve above T_l where they show a negative growth velocity. b) Logarithmic plot of experimental nucleation rates and crystal growth velocities in glass with the stoichiometric $\text{Li}_2\text{Si}_2\text{O}_5$ composition summarized from the Refs. [143–146,150,151]).

nucleation agents in many systems and may hence trigger the volume crystallization of desired phases [155,156].

Crystallization within droplets of a phase separated glass may follow a different mechanism: many nuclei may initially form within one droplet and then grow to numerous crystals which all occur within the boundaries of the former amorphous droplet. Alternatively, only one nucleus is formed inside a droplet and rapidly grows until a notable part of the droplet is occupied [16,157,674], as shown in Fig. 2. The size of such crystals is limited by the droplet size which can be tailored by modifying the time and temperature schedule applied to achieve phase separation, further details are presented in chapter 3.4.

It should be noted that spherulites may also appear to be spherical crystals in microscopic images. They are, however, composed of numerous individual crystals with different morphologies and orientations (see Chapter 2.3.3).

2.3. Polygon Crystals

The growth of crystals with a polygon (multi-cornered) shape is often observed and most widely associated with the term “crystal” outside of the scientific community. Ideally, these shapes should be called polyhedra (multi-faced), but rounded features frequently occur or the corners extend to form tips. As they all show corners, but not only faces, “polygon” best describes their geometric morphology. In the case of cubic crystals or structures with only a small tetragonal distortion, the growth of cubes or octahedra are the most common cases. All crystal classes may exhibit a polygon growth morphology which may easily become rather complex due to growth defects such as twinning. Traditional polygons form if the crystal growth velocities along the main (low indexed) crystallographic directions are similar. Extremely different growth directions along low indexed directions lead to the formation of needles (one very fast direction) or plates (one very slow direction). Examples are presented in Fig. 3. The hematite hexagon in Fig. 3 b) is slightly darker on the bottom side because this area is covered by a thin layer of glass [158]. The needles featured in Fig. 3 d) are also polygon as they appear rhombical/ rectangular in a cross section unless they are cut almost parallel to their fast-growing c-axis [159].

Elongated morphologies of free growing crystals can have two principal reasons.

- (i) If the interfacial energy varies along different crystallographic directions, those planes perpendicular to the directions of fast crystal growth should have a smaller interfacial energy. Then the equilibrium shape of the formed crystals is that attributed to a minimum energy related to a constant volume, a.k.a. the Wulff shape.
- (ii) If the morphology is controlled by kinetics, symmetry elements such as glide planes and screw axis play an important part and growth may be affected by the formation of diffusion barriers in the matrix [159]. Differing crystal growth velocities depending on the crystal lattice are explained by the periodic bond chain (PBC) theory [163-165] and the Bravais-Friedel-Donnay-Harker (BFDH) law [166]. Once crystals or their growth fronts interact and hinder each other during growth, their morphology usually changes.

2.3.1. Needle-Shaped Crystals

So far, there are comparably few examples for needle-shaped growth from glass melts, the best investigated case being the growth of mullite from aluminosilicate melts. Mullite ($\text{Al}_{(4+2x)}\text{Si}_{(2-2x)}\text{O}_{(10-x)}$ with $0 \leq x \leq 1$) is not a stoichiometric compound, but shows a large variation in the chemical composition and crystallizes with the space group No. 55 (Pbam) [167]. The by far fastest growing axis is the

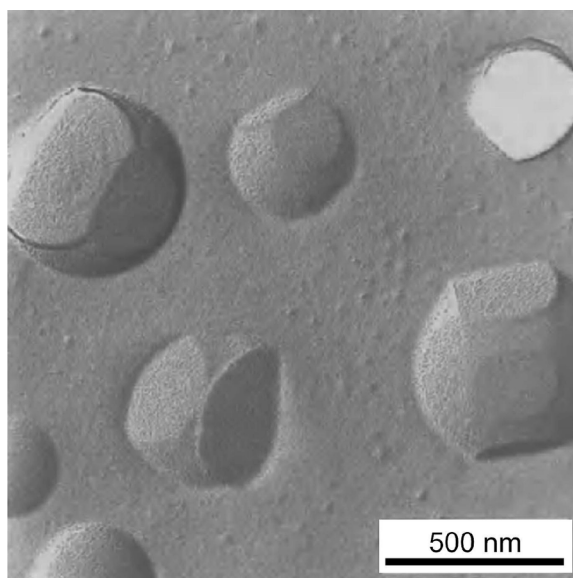


Fig. 2. SEM micrograph of apatite crystals grown in phosphate glass droplets, reprinted from Ref. [674] with permission from Elsevier.

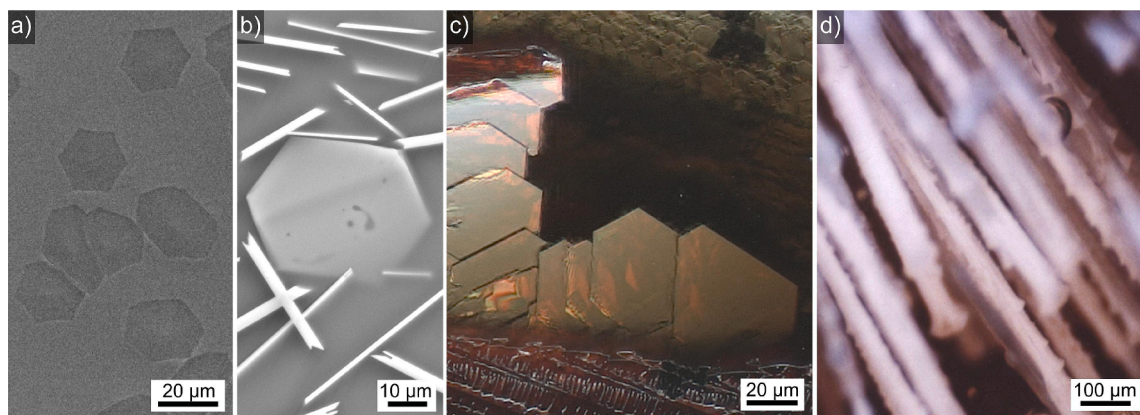


Fig. 3. Polygon crystals precipitated from glasses: a) SEM micrograph of hexagonal μ -cordierite at the immediate surface of a stoichiometric glass assumes a hexagonal shape if their c-axis is oriented perpendicular \pm ca. 30° to the surface [160]. b) SEM micrograph showing platelets of hexagonal hematite which appear as rods in a cross section unless they are oriented almost parallel to the surface [161]. c) Large hematite crystals show hexagonal plates at their boundaries in an optical micrograph where the transparent glass matrix allows a 3D impression [161]. d) Optical micrograph of mullite needles with a polygon cross section [159] crystallized from a $56.1 \text{ SiO}_2 \bullet 20.9 \text{ Al}_2\text{O}_3 \bullet 15.7 \text{ MgO} \bullet 7.3 \text{ TiO}_2 \bullet 0.03 \text{ Fe}_2\text{O}_3$ melt, reprinted from Ref. [162] with permission Elsevier.

crystallographic c-axis. An optical micrograph of a glass-ceramic with mullite needles crystallized from a glass with the composition $56.1 \text{ SiO}_2 \bullet 20.9 \text{ Al}_2\text{O}_3 \bullet 15.7 \text{ MgO} \bullet 7.3 \text{ TiO}_2 \bullet 0.03 \text{ Fe}_2\text{O}_3$ is presented in Fig. 3 d). Aspect ratios beyond 1:90 have been reported for the growth of mullite [168].

For the Wulff shape, the distances of certain crystallographic planes from the center of a crystal (strictly spoken, the lengths of the crystal plane normals passing the center) should be proportional to the respective specific interfacial energies [169]. Hence kinetic reasons must cause the extreme aspect ratios observed in mullite needles, because the interfacial energies crystal/surrounding glass melt were reported to be in a very narrow range from 0.2 to 0.4 N/m [29]. These cannot justify the differences in the crystal growth velocities necessary for the high aspect ratios observed after growth, illustrating why needle-shaped crystal growth cannot be explained by the Wulff shape. For the case of mullite growing in a glass melt, crystal growth is severely affected by the formation of SiO_2 -enriched diffusion barriers in their matrix [159].

Needle-shaped growth was also described for tetragonal crystals of the rutile type, e.g., from a glass in the system $\text{MgO}/\text{Al}_2\text{O}_3/\text{SiO}_2/\text{TiO}_2$ containing 4 mol% P_2O_5 [170]. The crystals were 300 nm long and 20 nm wide as is discernible in Fig. 4. Another example is the crystallization of SnO_2 from aluminoborate glass melts [171]. In both cases, tetragonal crystals with a rutile structure (space group $\text{P4}_2/\text{mnm}$ (136)) [172] grow fastest along their crystallographic c-axis reaching aspect ratios of up to 1:100.

Another case of needle-shaped growth is the crystallization of fluorapatite from melts in the systems $\text{SiO}_2/\text{Al}_2\text{O}_3/\text{CaO}/\text{P}_2\text{O}_5/\text{Na}_2\text{O}/\text{F}^-$ and $\text{SiO}_2/\text{Al}_2\text{O}_3/\text{CaO}/\text{P}_2\text{O}_5/\text{K}_2\text{O}/\text{F}^-$ described, e.g., in the Refs. [39,111,151,173,174] and [175]. Fluorapatite has the hexagonal space group $\text{P6}_3/\text{m}$ (176) [176] and shows rod- to needle-shaped growth where the crystallographic c-axis grows fastest [111]. It can, however, assume spherical shapes when grown inside phase separated droplets [111].

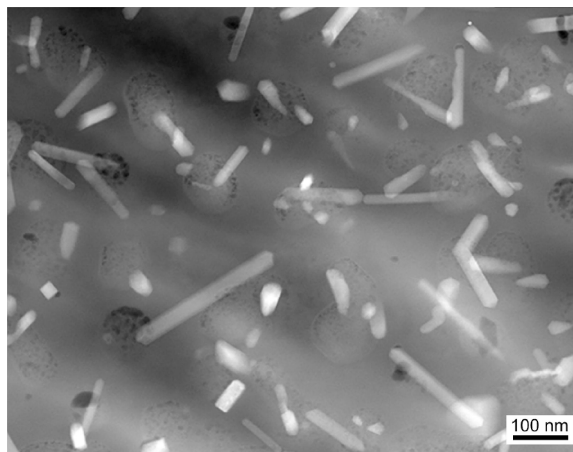


Fig. 4. TEM HAADF micrograph of rutile needles precipitated from a glass with the composition $5 \text{ Li}_2\text{O} \bullet 8 \text{ MgO} \bullet 11.5 \text{ Al}_2\text{O}_3 \bullet 56.5 \text{ SiO}_2 \bullet 4 \text{ TiO}_2 \bullet 4 \text{ P}_2\text{O}_5$. Reprinted from Ref. [170] with permission from Elsevier.

Further cases of glass-ceramics containing needle-shaped crystals are $\text{Li}_2\text{Si}_2\text{O}_5$ [177,178] and powellite (CaMoO_4) [179], which was crystallized from a glass in the system $\text{SiO}_2/\text{B}_2\text{O}_3/\text{Na}_2\text{O}/\text{CaO}/\text{Al}_2\text{O}_3/\text{MoO}_3/\text{Gd}_2\text{O}_3$ intended for the vitrification of nuclear waste. Needle-shaped Mg petalite ($2\text{Si}_2\text{N}_2\text{O}\cdot\text{MgO}\cdot\text{Al}_2\text{O}_3$) was reported to crystallize from an oxynitride glass containing ZrO_2 as a nucleation agent [180].

2.3.1.1. Plate-Shaped Crystals. Plate-shaped growth is frequently observed if, e.g., mica and related crystal phases, such as fluorophlogopite or muscovite crystallize [34-37,181-185]. To the best of our knowledge, the first glass-ceramics based on mica were reported in 1972 by G.H. Beall from Corning [186]. Later, strontium fluoro mica (G.H. Beall, 1973 [187]) and tetrasilic mica (D. Grossman, 1972 [36]) were described.

These layered phases also occur as natural minerals which usually incorporate OH^- (often denoted as “water”) into their crystal lattice. Fig. 5 a) shows fluoromica plates in a glass matrix while Fig. 5 b) presents hematite crystals, one of which is almost parallel to the surface [161] and hence discernible as a hexagonal plate.

Plate-shaped crystals frequently grow if the crystals have trigonal or hexagonal space groups [181] and the c-axis is usually perpendicular to the plate surface. Then the crystal growth velocity is large along the crystallographic a- and b-axes but small along the c-axis [182]. The aspect ratios may reach 1:100 [181] and depend on the chemical composition and the supplied temperature and time schedule. This has purely kinetic reasons and is not related to differing interfacial energies of various lattice planes. A highly distorted mica precipitated from a glass of the composition $57.3\text{ SiO}_2\cdot 11.5\text{ Al}_2\text{O}_3\cdot 14.8\text{ MgO}\cdot 2.6\text{ Na}_2\text{O}\cdot 2.5\text{ K}_2\text{O}\cdot 10.2\text{ F}\cdot 1.1\text{ Cl}^-$ first predominantly grows along the a- and b-axes during thermal treatment [182]. Much less distorted crystals subsequently grow rapidly at both plate surfaces. The large crystals have the same orientation as the highly distorted mica, implying an epitaxial relationship, but show a lower frequency of 100-twinning [183]. After some time of thermal treatment, the volume concentration of these crystals no longer increased, but their shapes continued to change. They became thicker, i.e., grew along the c-axis, but shrank along the a- and b-axes so that the crystals approached a blocky shape. This was denoted as a “crystallization pendulum” [184] and considered to be a type of “intracrystalline Ostwald ripening”, because the crystal arrangement changes its shape to minimize the interfacial energy, while the volume remains approximately constant. This is denoted as “intracrystalline” because only one crystalline body is involved in contrast to conventional Ostwald ripening although, strictly speaking, two mica phases are involved in the process. It can be assumed that the morphology of the crystals ultimately approaches an overall energetical minimum, i.e., their Wulff shape.

One of the first commercial phlogopite glass-ceramics was called MARCOR™ (Corning). The phlogopite composition does not form a glass using technically suitable cooling rates, which is why some excess SiO_2 and B_2O_3 were added [188]. The resulting crystallization process is fairly complex: first chondrodite ($2\text{Mg}_2\text{SiO}_4\cdot\text{MgF}_2$) is precipitated and subsequently transforms to norbergite ($\text{MgSiO}_4\cdot\text{MgF}_2$). Norbergite then reacts with the residual glass to form phlogopite and small quantities of mullite.

Other examples for plate-shaped growth are the hematite featured in Fig. 3 [161] and the negative thermal expansion phase $\text{BaAl}_2\text{B}_2\text{O}_7$ [189] which has the trigonal space group R32 (155) [190] and also grows fastest along its a- and b-axes [191].

2.3.1.2. Spherulitic Crystals. If multiple polygon crystals grow radially outwards from a common centre, they can form superstructures denoted as spherulites [192-196]. Here all crystals are initially oriented with the same crystallographic axis pointing away from the centre. If these structures grow homogeneously in all directions, they form a sphere. If, however, growth is inhomogeneous, the spherulite morphology can first become oval and then evolve into a dumbbell. Schematic 2D illustrations of such structures are presented in Fig. 6: a) ideal, b) ideal adjacent to, e.g., a surface or c) the dumbbell. If a 3D dumbbell [197,198] is cut along the line L1 in Fig. 6 c) and viewed perpendicular to its main growth direction, it looks just like an ideal spherulite. These cases can, however, be

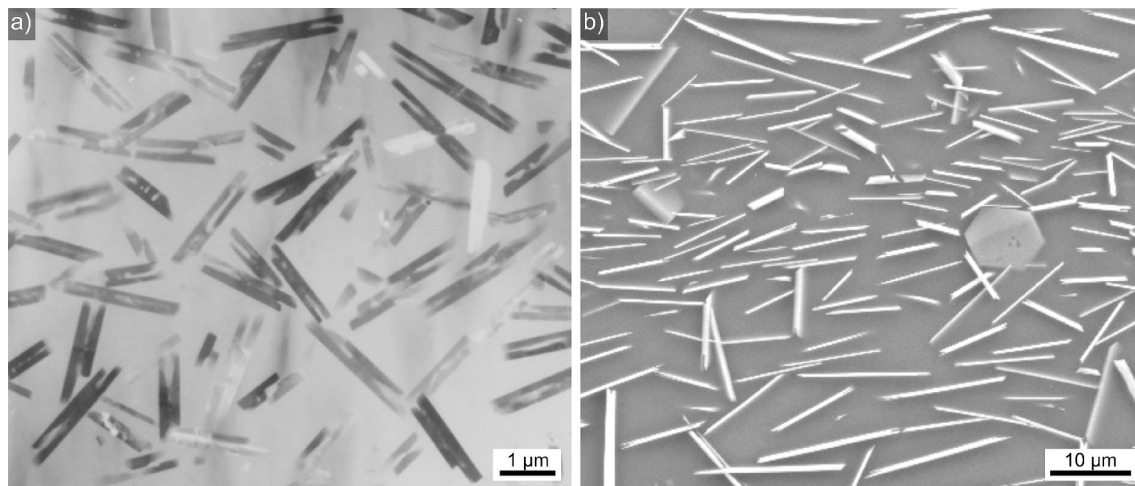


Fig. 5. a) Fluor mica crystallized from a $57.3\text{ SiO}_2\cdot 11.5\text{ Al}_2\text{O}_3\cdot 14.8\text{ MgO}\cdot 2.6\text{ Na}_2\text{O}\cdot 2.5\text{ K}_2\text{O}\cdot 10.2\text{ F}\cdot 1.1\text{ Cl}$ melt. Based on Ref. [182]. b) Hematite plates in a glass-ceramic, reprinted from Ref. [161] with permission from Elsevier.

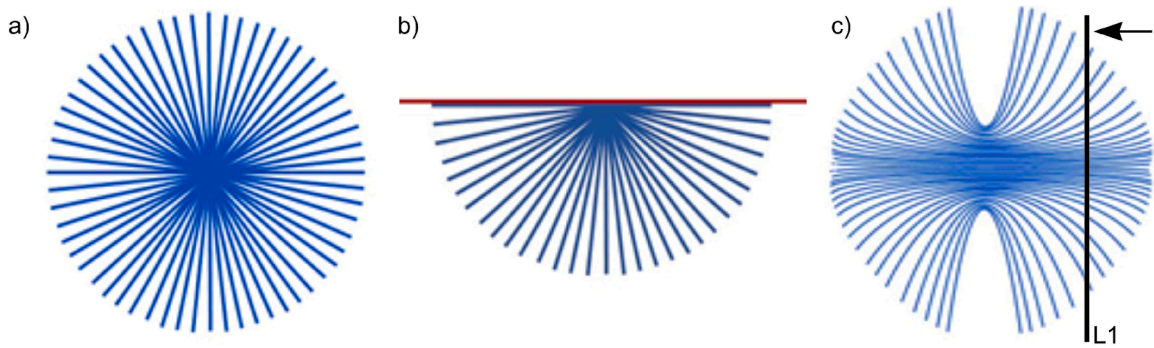


Fig. 6. Schematic illustrations of 2D spherulitic growth: a) ideal in free space, b) ideal adjacent to a surface and c) a dumbbell formed by asymmetric growth velocities. If a 3D dumbbell is cut along the cross section L1, it looks just like the ideal case featured in a). Based on Ref. [199].

separated by analyzing the crystallographic texture of the cross section using EBSD.

Examples of such non-ideal spherulitic structures in glass-ceramics are presented in Fig. 7. Fig. 7 a) shows the micrograph of a δ - $\text{Y}_2\text{Si}_2\text{O}_7$ dumbbell cut parallel to its fastest growth direction [195]. Such structures can be difficult to recognize if the prepared cross section is unfavourable as is the case in Fig. 7 b). As noted above, local orientation analysis can provide the necessary insight to identify the spherulitic superstructure.

Spherulitic morphologies are frequently observed in crystallized glasses, e.g., after the crystallization of $3 \text{ PbO} \cdot 2 \text{ SiO}_2$ by Carr and Subramanian [200] or $\alpha\text{-SrB}_4\text{O}_7$ by Zaitsev et al. [201]. Spherulites of the barium silicates $\text{Ba}_2\text{Si}_3\text{O}_8$ were reported by Rouxel et al. [202]. Spherulites of Ba_2SiO_5 grew in glasses of the BaO/SiO_2 system with a small amount of additive of Al_2O_3 observed by Lewis and Smith [203]. Surface crystallizing willemite (Zn_2SiO_4) also formed spherulites [204]. A challenging technique is the surface crystallization of devitrite spherulites from commercial soda-lime-silicate glasses, which may act as optical diffusors as reported by Butt et al. [205]. The formation of LiNbO_3 [206] spherulites from melts with the composition $35 \text{ Li}_2\text{O} \cdot 25 \text{ Nb}_2\text{O}_5 \cdot 40 \text{ SiO}_2$ was observed by Vigouroux et al.

2.4. Viscous Fingering and Dendrites

The mechanisms leading to viscous fingering and dendritic growth are quite different from those described in the chapters 2.2 to 2.3.3 where the kinetics of crystal growth define the growth morphology. For viscous fingering and dendritic growth, diffusion and heat transfer are more decisive for the growth morphology than, e.g., the lattice symmetry. These mechanisms occur if a crystalline phase is precipitated and the growth front becomes unstable. In glass-ceramics, a phase with another chemical composition is usually

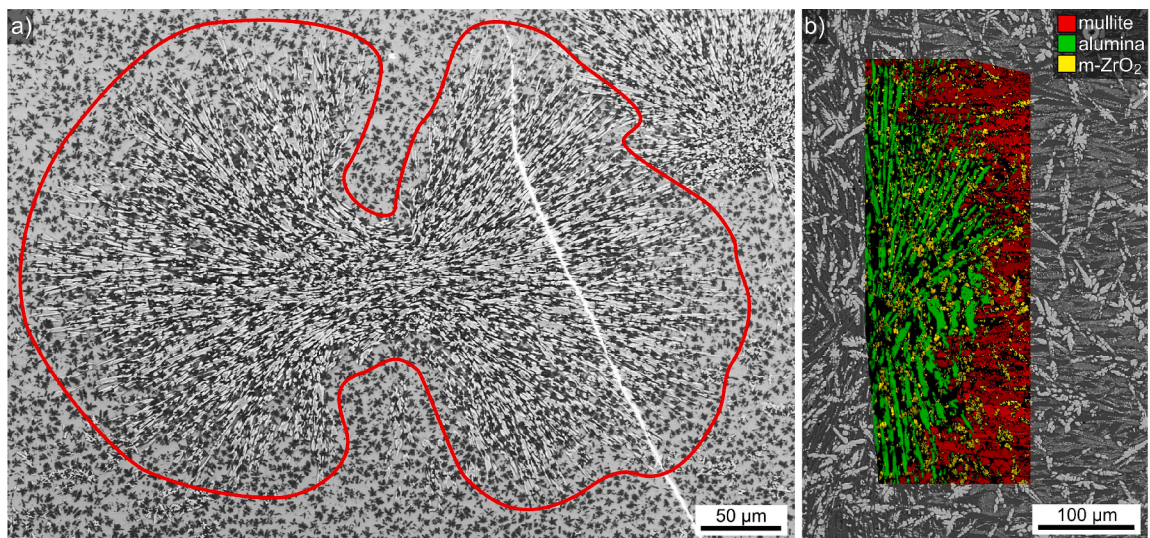


Fig. 7. Spherulitic growth: a) SEM-micrograph of a dumbbell-shaped δ - $\text{Y}_2\text{Si}_2\text{O}_7$ spherulite grown from a $17 \text{ Y}_2\text{O}_3 \cdot 33 \text{ Al}_2\text{O}_3 \cdot 40 \text{ SiO}_2 \cdot 2 \text{ AlF}_3 \cdot 3 \text{ Na}_2\text{O} \cdot 2 \text{ CeF}_3 \cdot 3 \text{ B}_2\text{O}_3$ mol% glass [195]. The red line is a guide for the eye to mark the spherulite perimeter. b) Phase map of an EBSD-scan performed on part of an alumina spherulite grown in an AZS-melt [196] and superimposed onto an SEM-micrograph of the area.

formed at the same time [94-98].

First the case of diffusion should be considered: if a residual liquid phase is formed along with the crystal, components forming the crystal must diffuse through an amorphous diffusion layer to attach to the crystal. This should decelerate crystal growth, especially at some distance from the site of nucleation where one-dimensional diffusion is predominant. If instabilities at the growth front occur, the crystal growth mechanism changes and a thin branch can rapidly grow through the diffusion layer. The thickness of this small branch subsequently either increases by radial diffusion or it remelts to minimize the surface. This may lead to hierarchical structures where some segments separate from the main dendrite, either by mechanically breaking off or re-melting [207]. Fig. 8 a) shows a dendritic structure formed by a (cubic) Fe_3O_4 crystal precipitated from a $11.2 \text{ Na}_2\text{O} \bullet 7.0 \text{ MnO} \bullet 51.8 \text{ SiO}_2 \bullet 30 \text{ Fe}_2\text{O}_3$ glass [93]. The framed area is presented in greater detail in Fig. 8 b) to show the polygon origin from which thin branches grew outwards. The superimposed orientation map shows that all crystal segments show the same orientation, i.e., are connected, which only changes by up to 8° near a neighbour. Continuous orientation changes can result from overlapping thermal fields at the growth front [208] or crystal collisions during growth and may also be affected by mechanical deformation during cooling.

Dendritic structures are not always as easy to recognize as in Fig. 8, especially in the cross sections usually featured by SEM micrographs. In polished samples, dendritic structures are arbitrarily cut and sometimes the observed structures are difficult to attribute to one dendrite. While such morphologies have been erroneously denoted as “skeletal growth” or “cellular structure of growth” in the past [75], it must be acknowledged that dendritic morphologies have been recognized in crystallized glasses [209] long before their orientational connection was proven using EBSD [75]. Failing to recognize dendritic structures can cause extreme errors in microstructure analysis if, e.g., nucleation rates are based on treating each dendritic segment as an independent crystal representing a nucleation event. If dendritic structures occur, the different branches of the crystals ideally have the same orientation but many versions of disturbed dendritic growth have been described [210,211]. Hence orientation maps or Inverse Pol Figure (IPF) maps of EBSD-scans usually show a homogenous colour which may only change continuously as grain boundaries cannot occur within a dendrite. This allows a clear attribution of various crystal segments to one dendrite. Fig. 9 a) shows an IPF map superimposed onto an SEM micrograph of YAG crystals precipitated from a $28.8 \text{ SiO}_2 \bullet 41.2 \text{ Al}_2\text{O}_3 \bullet 9 \text{ Y}_2\text{O}_3 \bullet 1 \text{ CeF}_3 \bullet 20 \text{ CaO}$ glass [212]. Differing dendrites have different orientations and hence appear in different colours, the interlocking of dendrites is clearly discernible. If dendrites are limited to a spherical volume like the microsphere featured in Fig. 9 b) [22] they can quickly fill the available space. This introduces the possibility of producing spheres containing a single crystal orientation without the necessity of extreme chemical purity as it is likely to be required for single crystals resulting from flash crystallization [154]. Drawing dendrites from a melt can allow the production of macroscopic single crystals [213].

Dendritic structures have been reported in glass-ceramics from various glass systems. They were, e.g., often reported for magnetite, e.g., by R. Harizanova et al. [93,161], X. Wang et al. [214-216], X. Wence et al. [217] and Romera and Rincon [218]. Apart from dendritic fersite [75] and YAG [212,219], the precipitation of dendritic $\text{Pb}_{1-x}\text{Sr}_x\text{Nb}_2\text{O}_6$ and $(\text{Ca},\text{Na})(\text{Nb},\text{Ti})_2\text{Nd}_{0.67}\text{O}_6\text{F}$ were described by D.F. Han et al. [220] and K. Wu et al. [221]. Dendritic growth of tetragonal ZrO_2 was described by A.H. Heuer et al. [222] and J.C. Mauro reported LiNbO_3 dendrites [223]. Furthermore, the crystallization of dendritic quartz solid solutions was reported by A.X. Xu [224], that of Li_2SiO_3 by D.U. Tulyaganov et al. [225] as well as that of diopside [226,227], $\text{Sr}_2\text{MgSi}_2\text{O}_7$ [228] or $\text{Zn}_{0.7}\text{Mg}_{0.3}\text{Al}_2\text{O}_4$ [229] from silicate melts of special compositions. $\text{Li}_{1.4}\text{Al}_{0.4}\text{Ti}_{1.6}(\text{PO}_4)_3$ and fluoroapatite of dendritic morphology were crystallized from phosphate melts as reported by C. Davis et al. [230] and R. Hill et al. [231].

Viscous fingering is even less known in the glass-ceramics community and can be very difficult to recognize. It is well known from liquid-liquid interactions when a low viscosity fluid is pushed against a high viscosity fluid and the crystallization of organic

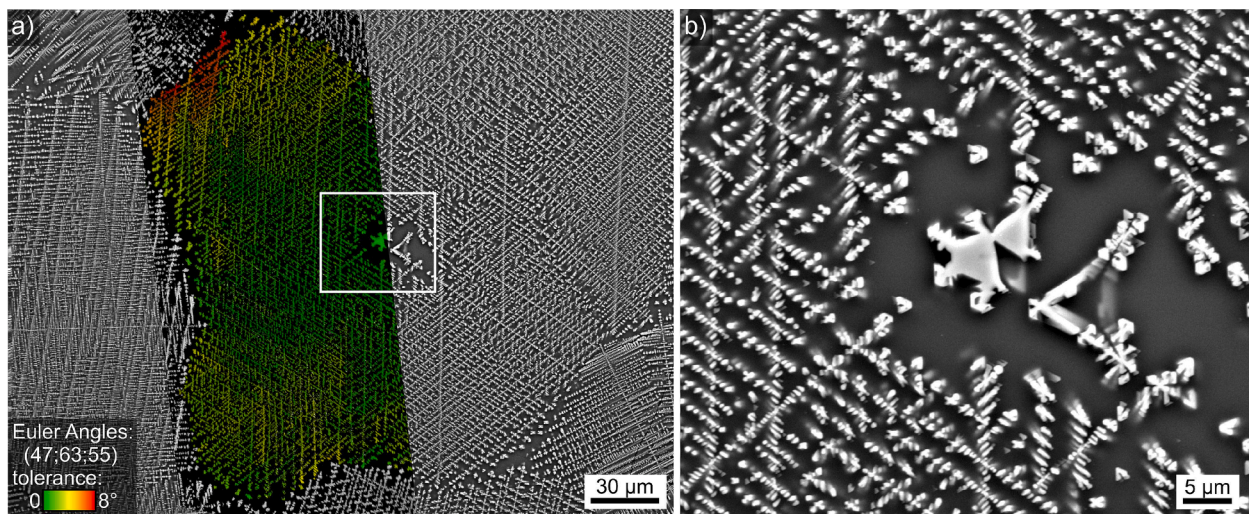


Fig. 8. Dendritic magnetite crystals precipitated from a $11.2 \text{ Na}_2\text{O} \bullet 7.0 \text{ MnO} \bullet 51.8 \text{ SiO}_2 \bullet 30 \text{ Fe}_2\text{O}_3$ glass. a) Orientation map of an EBSD-scan superimposed onto an SEM-micrograph. b) The framed area in greater detail. Based on Ref. [93].

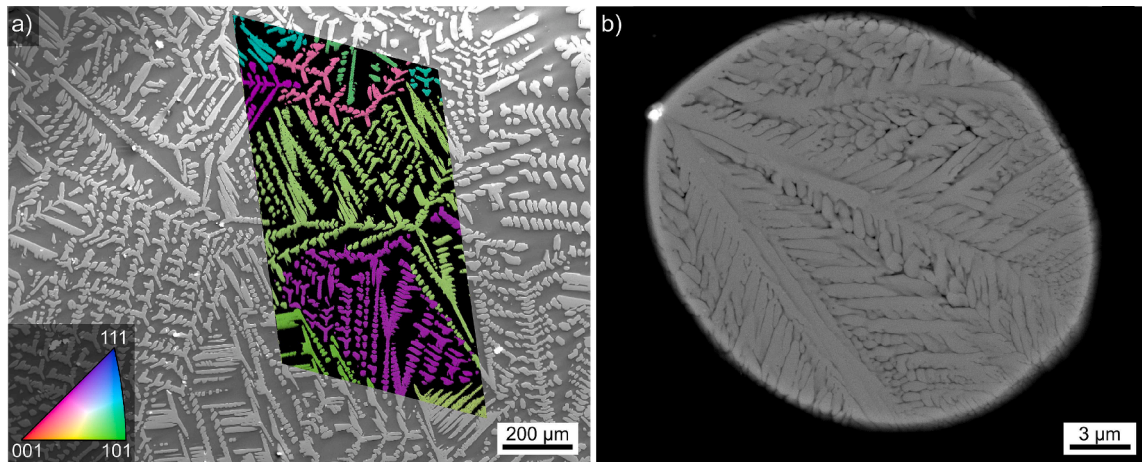


Fig. 9. YAG crystals precipitated from a $28.8 \text{ SiO}_2 \bullet 41.2 \text{ Al}_2\text{O}_3 \bullet 9 \text{ Y}_2\text{O}_3 \bullet 1 \text{ CeF}_3 \bullet 20 \text{ CaO}$ glass. a) IPF+IQ map of an EBSD-scan superimposed on an SEM micrograph, based on Ref. [212]. b) SEM micrograph of a microsphere containing YAG dendrites crystallized at high temperatures, based on Ref. [22].

compounds. Instabilities at the growth front are decisive for the morphology evolution in analogy to dendritic growth. Structures described as “flower like” in 1990 by W. Vogel [209] almost perfectly match the morphologies of viscous fingering in the Saffman-Taylor Experiment performed in a Hele-Shaw cell [95]. Whether these are indeed crystalline is currently unknown as neither the performed X-ray diffraction and nuclear magnetic resonance spectroscopy have the necessary spatial resolution [209] and the measured signal may originate from the dendrites also observed in the microstructure. Other glass-ceramics contain blackberry-shaped structures [209,232] resulting from a phase separation, i.e., a classic liquid-liquid interaction as for example featured in Fig. 10 a). Fig. 10 b) presents a cross section through such a structure and the morphological similarity to viscous fingering is apparent. BaTiO_3 of most likely plate-shaped morphology crystallized inside this structure and EBSD was used to prove that its fingers show differing crystal orientations [232]. SEM-micrographs of structures with related morphologies in phosphate glass-ceramics have been published [233-236].

Viscous fingering as an actual crystal growth mechanism is another matter, but the link to dendritic growth was proposed based on simulations by J. Nittman and H.E. Stanley in 1986 [237]. Later, applying EBSD to surface crystallizing Sr-fresnoite [208] showed a texture in a nm-scale microstructure that could result from a plane growth front of viscous fingering passing through a material. The expected effect that this growth mechanism occurs at slower growth velocities and shows different orientation relationships than dendritic growth of the same phase was later confirmed experimentally [94]. Comparable observations have only been made for the crystallization of $\text{Sr}_{0.75}\text{Al}_{1.5}\text{Si}_{0.5}\text{O}_4$ [12] to the best of our knowledge.

The formation of the connected microstructures resulting from dendritic growth or viscous fingering can have a tremendous effect

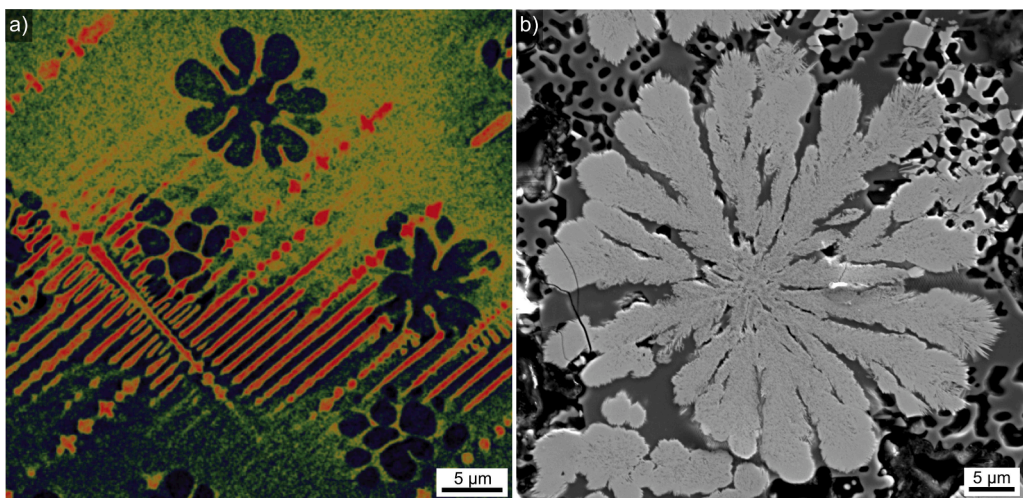


Fig. 10. Morphologies possibly resulting from viscous fingering: a) 2D image of silica-rich phase separations amongst dendritic powellite reconstructed from nano-computer tomography data reprinted from Ref. [676]. b) SEM-micrograph of a cross section through a crystallized blackberry-shaped phase separation containing BaTiO_3 , based on Ref. [232].

on physical properties like the electric conductivity of, e.g., magnetite containing glass-ceramics [238]. Interconnected crystals increase the electric conductivity by several orders of magnitude. Large dendritic structures have predominantly been observed in glasses and their melts when comparatively few nuclei are present, the period of time enabling crystal growth is sufficiently large and the concentrations of the components to be crystallized is not too small [93]. Dendrites generally coarsen with time to minimize their surface energy [239], an effect also observed when annealing fresnoite dendrites in a glass melt [213].

Dendrite formation has been the subject of numerous review papers [239-242] which also explain when dendrites are formed and when viscous fingering occurs [243]. The formation of dendrites from glass melts, however, was only mentioned casually in the literature apart from their analyses by EBSD and has not been reviewed so far. It seems likely that dendritic growth at comparatively low temperatures, i.e., not far above T_g , is triggered by the hindered diffusion. By contrast dendritic growth at high temperatures near T_i , where the viscosity is some orders of magnitude lower, is probably triggered by the limited heat transfer. As a general rule large, coarse dendrites form at higher temperatures and growth velocities than small, fine-branched dendrites.

2.5. Nano Crystals

The formation of nanocrystals from glass melts was achieved centuries ago, for example to prepare the well-known “gold ruby glasses” [244-246]. Of course, the origin of their red colour was not understood at the time as it is caused by a precipitation of nano-sized metallic Au crystals and was later explained by the Mie Theory. These glasses contain Au^+ , which is homogeneously dissolved in the glass melt. The glasses usually also contain Sb^{3+} , As^{3+} or Sn^{2+} which are polyvalent, i.e., occur in glass melts in different oxidation states. This leads to the redox equilibrium shown in Eq. (12) for the example of Sb where decreasing temperatures shift this equilibrium to the right. Hence, the formation of metallic Au is favoured during cooling and forms clusters either spontaneously or by specific thermal treatments at temperatures around T_g [244].



In analogy, glasses containing Ag [247] or Cu [248] show the same phenomenon and respectively show yellow or red colours. Other examples for nano-sized precipitations are so called “striking glasses” which contain CdS, CdSe, CdTe or solid solutions of them [249-252], respectively causing yellow and orange to red colours. In analogy, photochromic or other photosensitive glasses also show nanocrystals of silver halides or copper halides [253-256]. All these examples result from adding small concentrations of the respective elements (50 to 1000 ppm) which then form nano crystals ranging from 5 to 50 nm in size. The preparation and chemical reactions leading to the formation of such nano-crystals are widely understood. In most cases, the as melted glasses are colourless and the colours develop during thermal treatments at temperatures in the range from their respective T_g to few ten K above it.

Precipitating silver halide or copper halide nano crystals, i.e., crystals based on AgCl, AgBr [257,258], CuCl or CuBr [259-261], enables to produce photochromic glasses which show reversible darkening when illuminated and are usually based on borosilicate glasses. Their preparation route is similar to the precipitation of noble metal or CdS and related crystals: the glass is thermally treated slightly above T_g . However, the silver halides are liquid at this point as their melting points are $<500^\circ\text{C}$ and their melting point

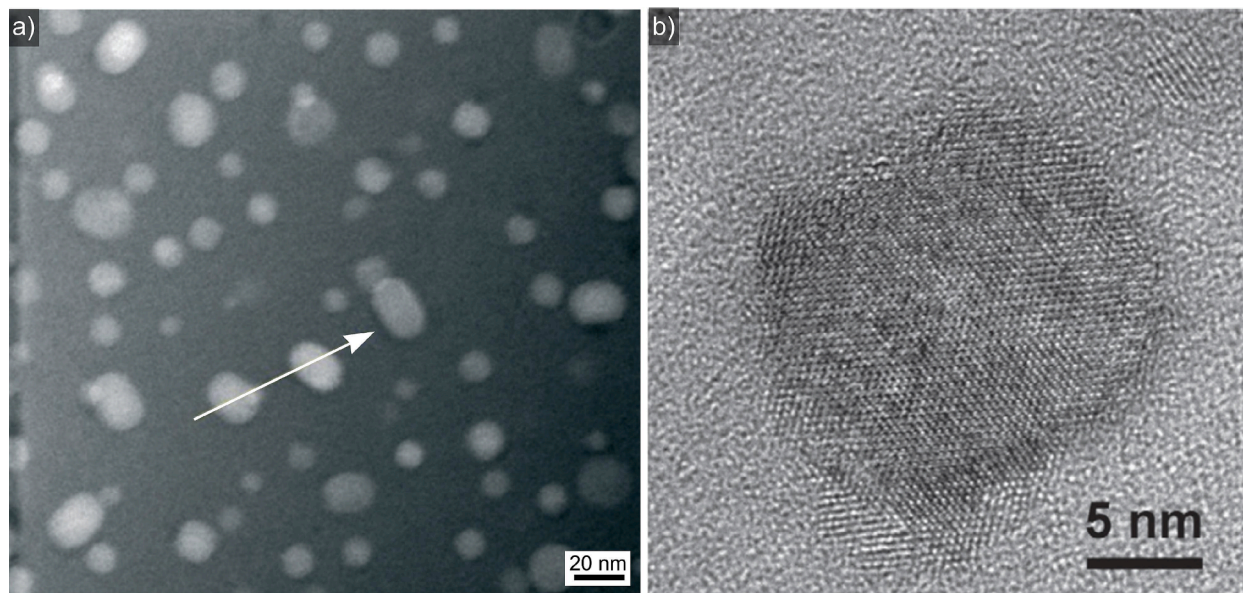


Fig. 11. TEM micrographs of fluoride nano crystals precipitated from glass. a) $KLaF_4$ crystals precipitated from a glass with the composition $70 SiO_2 \cdot 7 Al_2O_3 \cdot 16 K_2O \cdot 7 LaF_4$, based on Ref. [62]. b) $NaLaF_4$ crystal precipitated from a $70 SiO_2 \cdot 7 Al_2O_3 \cdot 8 K_2O \cdot 8 Na_2O \cdot 7 LaF_4$ glass in a higher magnification, reprinted from Ref. [61] with permission from Elsevier.

decreases with decreasing inclusion size following the Gibbs-Thomson Eq. (13) [260,262]:

$$\frac{\Delta T}{T_m} = \frac{(2\sigma V_m)}{(r\Delta H_m)} \quad (13)$$

where ΔT is the decrease of the melting temperature, T_m , V_m and H_m are the respective melting temperature, molar volume and melting enthalpy of infinitely large crystals and σ is the surface energy. In the case of copper halides, the effect can be measured using high temperature UV-vis spectroscopy because the exciton bands disappear above the melting point [260,261].

If larger concentrations of nanocrystals are to be precipitated, the situation is quite different. According to Chapter 2.1., the formation of comparatively high quantities of nano-crystals is possible if the nucleation rate is maximum while the crystal growth velocity is still low at the chosen temperature. As the crystal growth velocity cannot be negligible at temperatures slightly above T_g , the formed nuclei immediately start to grow. Hence, the nuclei formed first grow to a larger size than later formed nuclei, causing a fairly broad crystallite size distribution. It becomes broader with increasing nucleation time if the crystal growth velocity is time independent and, in most cases, does not lead to satisfying results as the largest crystals scatter light even when crystal volume concentrations only reach a few percent.

After some time, the volume concentration of the precipitated particles approaches a maximum. Then Ostwald ripening causes small particles to shrink while large particles grow further, leading to a particle size distribution matching the well-known theory of Lifshitz, Slyozov and Wagner (LSW theory) [263]. If the crystalline volume concentration exceeds 1 % in such a system, the size distribution becomes broader than the LSW distribution and better matches the Brailsford and Wynblatt (B&W) theory [264].

Hence other strategies must be utilized to achieve a narrow crystal size distribution and a comparatively large crystal volume concentration. If diffusion barriers homogeneously form around all directions of a growing crystal, its growth velocity will drastically decrease and effectively stop. Fig. 11 a) shows KLaF_4 nano crystals precipitated from a melt with the composition $70 \text{ SiO}_2 \cdot 7 \text{ Al}_2\text{O}_3 \cdot 16 \text{ K}_2\text{O} \cdot 7 \text{ LaF}_4$ [62]; some of these crystals (white arrow) show an elongated shape. Fig. 11 b) shows a high-resolution TEM micrograph of a NaLaF_4 crystal crystallized from a glass with the composition $70 \text{ SiO}_2 \cdot 7 \text{ Al}_2\text{O}_3 \cdot 8 \text{ K}_2\text{O} \cdot 8 \text{ Na}_2\text{O} \cdot 7 \text{ LaF}_4$ with discernible lattice planes. It is surrounded by a thin layer enriched in SiO_2 (not discernible in Fig. 11), which acts as a diffusion barrier [61] as will be explained in detail in chapter 3.5.

Glasses have also been reported to contain heterogeneities with diameters $< 2 \text{ nm}$. SAXS measurements performed on an oxy-fluoro silicate glass showed two types of heterogeneities to occur after thermal treatment, both surrounded by a silica enriched shell [265]: CaF_2 crystals of about 25 nm in diameter as well as tiny heterogeneities with diameters of 1.6 nm enriched in CaF_2 . SAXS studies of a multi component lithium aluminosilicate glass with TiO_2 and ZrO_2 as nucleating agents revealed heterogeneities with diameters of 0.8 nm enriched in both TiO_2 and ZrO_2 immediately after cooling the melt [266]. Further thermal treatments enriched the heterogeneities in TiO_2 and ZrO_2 and led to crystallization detected using XRD in both cases stated above. However, these XRD results do not prove that the initial heterogeneities were crystalline.

Another notable case is a microstructure stated to be composed of “paracrystals” formed by cooling a glass with the composition $\text{Ca}_3\text{Al}_2\text{Si}_3\text{O}_{12}$ melted at 1000°C , all under a pressure of 15 GPa [267]. TEM studies showed these “paracrystals” to have diameters from 1 to 2 nm. It seems likely that the high pressure and temperature led to the crystallization of a phase later transformed to one or more crystalline phases once the pressure was removed for sample preparation. Another group reported the “...transient appearance of a crystalline nucleus with a size of $\sim 1 \text{ nm}$ over a few seconds” detected by high temperature TEM in a glass of the system $\text{SiO}_2/\text{TiO}_2$ prepared by a sol-gel method [268]. Although the Refs. [267] and [268] report cases where the glasses did not pass the status of a thermodynamically stable state (i.e., the melt above T_i) at ambient pressure, the observed crystal sizes may be viewed as hints towards the appearance of clusters with a sub-critical size.

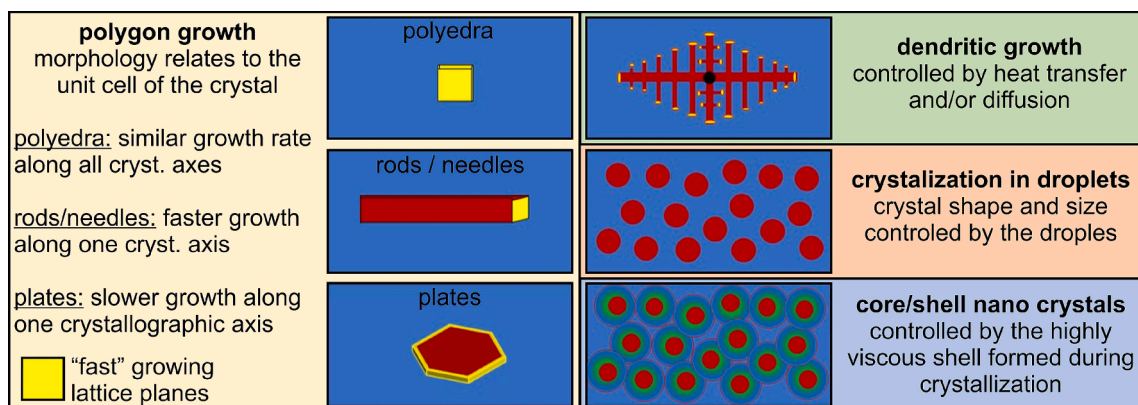


Fig. 12. Comparative overview of the technologically most relevant crystal growth morphologies in glass-ceramics.

2.6. Comparison of growth morphologies

The technologically most important crystal growth morphologies in glass-ceramics are compared with each other in Fig. 12. As outlined above, all crystal phases can show all presented morphologies given the right conditions. Polygon growth can be recognized by polyhedra, rods and needles or plates. Polyhedra form when all growth occurs along all crystallographic axes with similar velocities. The much/extremely faster growth of one crystallographic axis leads to the formation of rods/needles. If, however, one crystallographic axis grows much slower than the others, the resulting crystal forms a plate. The outer boundaries of these polyhedra can reflect the unit cell, but twinning, 3D diffusion at tips versus 2D diffusion at faces and unfortunate cross sections can severely modify their visual impression in micrographs.

Dendrites form when the growth fronts become instable at higher growth velocities. “Slow” dendritic growth leads to fine dendrites whereas “faster” dendritic growth leads to coarser dendrites. Cross sections where all the features of one dendrite are connected with each other are extremely rare as the cut plane must almost perfectly align with one dominant growth direction. They are, however, easily identified by EBSD (see Fig. 9 a)) as they are single crystals, meaning all segments of one dendrite show the same crystal orientation. Crystallization inside droplets after phase separation leads to crystals matching the shape of the droplet. Spherical or polygon growth completely fill the droplet, but if a sphere is large enough, the right conditions can also cause a dendrite to form with an overall droplet shape as shown in Fig. 9 b). The highly viscous shell formed during the growth of core/shell nano crystals limits the growth velocity at a very early stage, so that these crystals generally assume a spherical morphology before their growth is effectively stopped.

3. Tools to Tailor the Microstructure

This chapter describes tools which enable to tailor the microstructure of glass-ceramics and hence have an important effect on the resulting physical properties. There are multiple principles how the microstructure can be affected by the chemical composition and the supplied preparation techniques. Various additives in relatively small concentrations may promote or suppress phase separation or nucleation and can lead to the formation of diffusion barriers. The applied temperature/time schedule is decisive for both nucleation and crystal growth, for the volume concentration of the crystalline phases and in many cases also affects the type of phases formed. The crystallization of glass melts always occurs at an elevated temperature requiring subsequent cooling. Most glass-ceramics are multi-phase materials composed of at least one crystalline and one amorphous phase with differing CTEs. Hence internal stresses form during cooling and cannot relax below the T_g of the residual glass. These stresses may reach even higher values if the crystalline phase shows phase transitions below T_g accompanied by a volume effect [46,84,89,269,270], which widely affect the mechanical properties of such glass-ceramics [89]. However, too high stresses lead to the formation of cracks and must hence be avoided. Last but not least, techniques leading to, e.g., localized nucleation or the viscous deformation of a melt, during or after crystallization, can provide very special structures such as a crystal orientation and even polarity alignment. However, they are of limited technological relevance so far and hence beyond the scope of this review.

3.1. Chemical Composition, Phase Diagrams and Glass Formation

Most commercial glass-ceramic compositions are systems containing 7 to 14 components, which is why phase diagrams for them are not available. In some cases, useful information can be extracted from related three-component phase diagrams, but the phases which should crystallize from a thermodynamic point of view often fail to form in experiments where thermodynamically less advantageous phases sometimes crystallize. The simplest examples feature high temperature modifications precipitated at temperatures where the low temperature phases should still be stable, as, e.g., observed during the crystallization of BaSi_2O_5 glasses [271,272]. Another example is the formation of various $\text{Y}_2\text{Si}_2\text{O}_7$ polymorphs from glasses within the basic system $\text{Y}_2\text{O}_3/\text{Al}_2\text{O}_3/\text{SiO}_2$ [119,195,273-

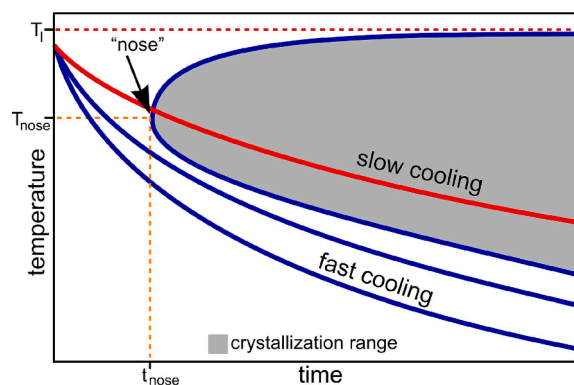


Fig. 13. Schematic TTT-diagram to judge the cooling rate necessary to avoid crystallization which occurs if the supplied temperature -time schedule enters the crystallization range, e.g., follows the red curve. Based on Ref. [287].

[276] all crystallized at approximately the same temperature. Most notable is the almost simultaneous but independent formation of four $\text{Y}_2\text{Si}_2\text{O}_7$ polymorphs at the immediate surface of a glass annealed at only 900 °C [277] although $\alpha\text{-Y}_2\text{Si}_2\text{O}_7$ is the only thermodynamically stable polymorph below 1225°C according to the literature [278] which was critically evaluated in Ref. [277].

Some phase diagrams contain stable miscibility gaps above T_1 as, e.g., observed for rare earths/ SiO_2 or alkaline earths/ SiO_2 [278-282]. Metastable phase separations, i.e., phase separations where two liquid phases of different chemical compositions are formed below T_1 , do not describe a thermodynamically stable state and hence do not appear in most phase diagrams. Nevertheless, metastable phase separations are drawn into special diagrams to visualize the compositions formed at the respective temperatures. This can be helpful and also provides hints whether droplet or interpenetrating structures may be formed. However, the latter information is not beyond doubt because the structures may change with time or upon cooling.

Phase diagrams are a description of thermodynamically stable phases. As glass is not thermodynamically stable, it is not surprising that a strict correlation of phase diagrams and glass formation does not exist. Strictly speaking, phase-diagram based conclusions on the general chemical compositions possibly formed in a glass using suitable cooling rates cannot be drawn. Nevertheless, the tendency for glass formation within a given chemical system is comparatively high for near eutectic compositions where the T_1 is comparatively low and hence the viscosity at a temperature slightly above the T_1 is relatively high.

A melt may crystallize during cooling depending on the cooling rate. A smaller cooling rate generally narrows the range of chemical compositions allowing glass preparation in a system. This behaviour is sometimes visualized in so called temperature-time-transformation (TTT)-curves, where the temperature is plotted against the time [283-285]. Fig. 13 presents a schematic TTT-curve where the gray region marks the crystallization range, which is specific to each glass composition. If the cooling rate exceeds a certain limit, the time dependence of the temperature (blue lines) does not enter the grey region in Fig. 13 and the melt does not crystallize.

For many glasses, the temperature attributed to the so called “nose” in Fig. 13 is about 0.78 of the liquidus temperature, i.e. $T_{\text{nose}} = 0.78 T_1$ [286]. The critical cooling rate required to obtain a glass is then given by Eq. (14) [286]:

$$\left(\frac{dT}{dt}\right) \approx \frac{T_1 - T_{\text{nose}}}{t_{\text{nose}}} \quad (14)$$

In simple glass compositions, i.e., where the coordination numbers of each component neither depend on their concentration nor on the temperature, the cooling rate above which a glass is obtained becomes higher if the network connectivity decreases. Then the grey region in the TTT-diagram of Fig. 13 becomes larger. Si atoms in oxidic glasses prepared under ambient pressure are always coordinated fourfold with bridging and/or non-bridging oxygens. The established nomenclature denotes such Si atoms coordinated with four bridging oxygens as Q^4 , while Si atoms coordinated with 3, 2, 1 and 0 bridging oxygens are respectively denoted as Q^3 , Q^2 , Q^1 and Q^0 [288]. In simple alkali silicate glasses, the arrangement of the non-bridging oxygens is approximately distributed randomly. Increasing temperatures shift the distribution even closer to the model of random distribution [289-292]. This means that the probability of an additionally introduced alkali ion causing a non-bridging oxygen coordinated to a Q^0 , Q^1 , Q^2 , or Q^3 unit is proportional to the respective Q^n concentration. This structural concept is in agreement with the viscosity depending on the network modifier concentrations [292] as well as with solid state NMR investigations [289-292] which enable to quantify the Q^n units. It has, however, not been proven for all possible network modifying components and it does not apply to other glass systems, e.g., alkaline earth meta phosphate glasses. In the latter glasses, nearly all PO_4 -groups are linked to two other PO_4 groups, i.e., PO_4 groups linked to three or only one other PO_4 group are scarce and long chain structures [293,294] with only very few crosslinks are formed. The formation of chain structures can also be observed in the rheological behaviour as shear stress leads to shear thinning due to an alignment of the chains [295,296]. In the statistic arrangement described for meta silicate glasses such as $\text{Na}_2\text{O}\cdot\text{SiO}_2$, numerous Q^1 and Q^3 units also exist next to the Q^2 units. Here the chains are highly cross-linked and are not as long as in meta phosphate glasses.

A statistic arrangement of the non-bridging oxygens enables to calculate a mean network connectivity. These considerations were first applied by M. B. Myers and E. J. Feltz as early as 1967 [297] to chalcogenide glasses [298-301], later to amorphous Si and Ge [302], but can generally be applied to any glass network. One of their main applications was the explanation of the glass transition [302-304] and the ionic conductivity [299,305-308,437,473]. The chemical durability, especially of bioglasses, was also correlated with the network connectivity [309,310]. A high mean network connectivity leads to a “rigid” network while a low connectivity leads to a “floppy” network. The threshold for the network connectivity is 2.4 below which a “floppy network” is obtained [311,312]. This means that an average concentration of bridging oxygen per network former atom below 2.4 leads to an overall floppy network in which the mobility and diffusivity should be high. The fragility of a glass network [313,314] also depends on the network connectivity, which can be best illustrated if the glass viscosity is described by the Adam-Gibbs model stated in Eq. (15):

$$\eta = \eta_0 e^{\frac{B}{TS_{\text{ex}}}} \quad (15)$$

with η_0 and B = constant and S_{ex} being the excess entropy. The reduced fragility index m^* is defined by Eq. (16):

$$m^* = \left. \frac{d[S_{\text{ex}}(T)/S_{\text{ex}}(T_g)]}{d(T/T_g)} \right|_{T \rightarrow T_g} \quad (16)$$

D. L. Sidebottom reported that a variety of glass compositions, spanning chalcogenide, borate and phosphate glasses, with a network connectivity of 2 show a large m^* value of about 4 [315]. The value of m^* decreases with an increasing network connectivity until it

reaches a value of about 1 at a network connectivity of 2.4.

Networks with a connectivity >2.4 nevertheless contain tiny floppy regions with a high mobility. In principle, nucleation during cooling may occur in the floppy parts of the network or at the border between the floppy and rigid regions and is followed by crystal growth [316–323]. This has especially been shown for the crystallization of fluorides [317,323]. As the temperature curves of nucleation and crystal growth usually do not overlap much, the nucleation temperature is usually too low for discernible crystal growth during a fast cooling such as when casting a glass melt. Crystal growth is strongly affected by the crystal structure and in many cases not only an effect of the diffusivity of glass melt components; otherwise, e.g., the growth of needles would not occur, as will be pointed out below. The glass stability decreases with increasing network modifier concentrations. It should be noted, however, that the classification of glass components into network formers and network modifiers is only a rough estimation that cannot give more than a first hint of the crystallization behaviour.

“Glass stability diagrams” are frequently presented in the literature, usually for three component systems. The most comprehensive collections of three component diagrams so far have been published by M. Imaoka et al. for silicate [324], borate [325] and tellurite systems [326]. It should be noted that the “glass formation ranges” strongly depend on the supplied experimental conditions, e.g., the cooling rates, for which strict and widely accepted standards do not exist. They are mostly related to laboratory experiments, where a melt is removed from a furnace and cooled below T_g within a few minutes. Using other techniques, such as rapidly quenching the glass melt by water cooled copper twin rollers [327,328], notably increase the “glass formation range”. Hence, the glass formation ranges determined in different laboratories are of limited comparability. Nevertheless, they allow a rough estimate in which composition ranges glasses form. Ultimately, any liquid can become an amorphous solid if the cooling rate is high enough.

There are remarkable differences concerning the glass formation ranges in binary oxidic systems. For the binary $\text{Na}_2\text{O}/\text{SiO}_2$ and CaO/SiO_2 systems, glass formation is reported to occur up to Na_2O or CaO concentrations of 42 mol%, which is attributed to a network connectivity of 2.55 [324] and not far from the percolation threshold of 2.4. For the binary $\text{Li}_2\text{O}/\text{SiO}_2$ and BaO/SiO_2 systems, glass formation was reported up to concentrations of 61 mol% Li_2O and 60 mol% BaO where continuous networks no longer exist. In many cases, the glass forming ranges are larger if more than one network modifier occurs. Increasing the number of components in glasses with the same network connectivity usually decreases their tendency towards crystallisation because rearranging the glass structure into a crystal is simply less probable as components not incorporated into the crystal must be expelled via diffusion. The nucleation in glasses is furthermore widely affected by the occurrence of minor components which might lead to nucleation (nucleation agents) or, however, to a deceleration of the crystallization process (nucleation inhibitors).

3.2. Use of Nucleating Agents

While many basic glass compositions such as the $\text{MgO}/\text{Al}_2\text{O}_3/\text{SiO}_2$ system [147,160] show sole surface crystallization, this is not desired for most applications where isotropic properties are usually required. In order to achieve bulk crystallization, it is hence often useful to add components denoted as “nucleating agents” which trigger nucleation throughout the volume. Traditional nucleating agents are noble metals, predominantly Pt [329–338], added to the raw materials in concentrations ranging from 20 to 200 ppm. Fig. 14 shows an example where small Pt particles with adjacent $\text{Ba}_{0.5}\text{Sr}_{0.5}\text{Zn}_2\text{Si}_2\text{O}_7$ crystals precipitated from a glass of the composition $8\text{BaO}\cdot 8\text{SrO}\cdot 34\text{ZnO}\cdot 50\text{SiO}_2$ (+50 ppm Pt) [334]. Other noble metals such as Au or Ag can have a similar effect, but the

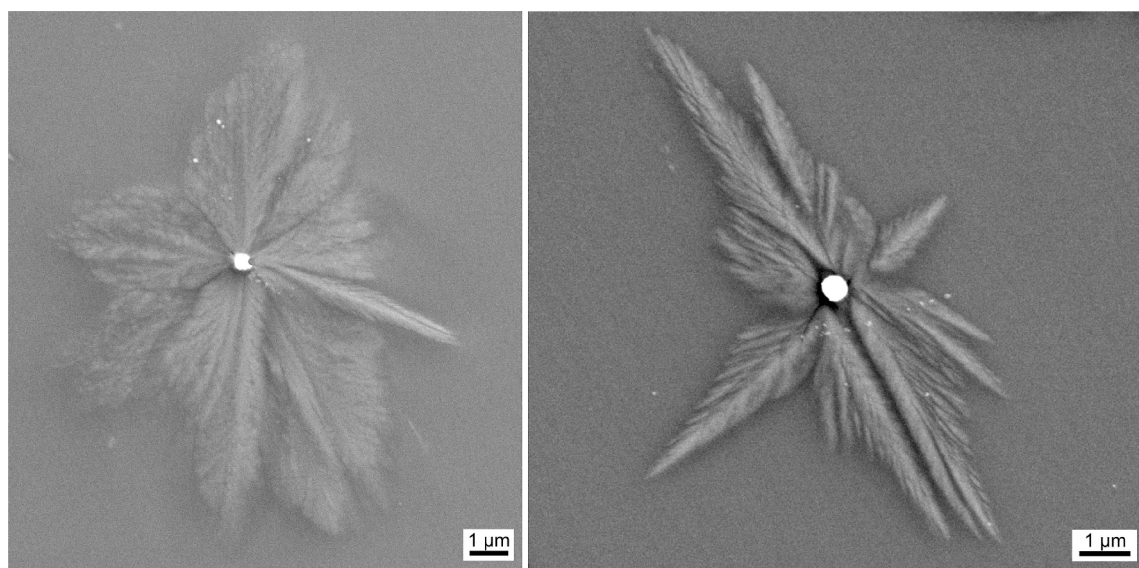


Fig. 14. SEM micrographs of $\text{Ba}_{0.5}\text{Sr}_{0.5}\text{Zn}_2\text{Si}_2\text{O}_7$ crystals grown around Pt nuclei in an $8\text{BaO}\cdot 8\text{SrO}\cdot 34\text{ZnO}\cdot 50\text{SiO}_2$ glass-ceramic containing 50 ppm of Pt. Reprinted from Ref. [334] with permission from Springer Nature.

necessary concentrations are often notably higher [339-343]. They are successful nucleating agents in a wide range of oxidic glass compositions and by far not as specific as the effect of oxidic nucleation agents which will be discussed below.

Usually, raw materials containing noble metals in their oxidized form such as AgNO_3 , PtCl_4 or HAuCl_4 are used. HAuCl_4 reacts to

Table 1

Oxidic nucleating agents which lead to bulk nucleation in the noted glass systems.

Glass System	Nucleation agent	Reference
Silicate glasses		
$\text{Li}_2\text{O}/\text{SiO}_2$	ZrO_2	[384,385]
	ZrO_2 , TiO_2 , P_2O_5	[383]
	Cr_2O_3	[397]
$\text{Li}_2\text{O}/\text{BaO}/\text{SiO}_2$	TiO_2 , ZrO_2 , V_2O_5 , Nb_2O_5	[403]
$\text{Li}_2\text{O}/\text{K}_2\text{O}/\text{ZnO}/\text{SiO}_2$	P_2O_5	[407,408]
$\text{Na}_2\text{O}/\text{CaO}/\text{SiO}_2$	ZrO_2	[386,387]
$\text{Na}_2\text{O}/\text{MgO}/\text{SiO}_2$	$\text{TiO}_2 + \text{ZrO}_2$	[409]
$\text{Na}_2\text{O}/\text{K}_2\text{O}/\text{SrO}/\text{BaO}/\text{SiO}_2$	TiO_2	[357]
$\text{CaO}/\text{SiO}_2/\text{ZrO}_2$	Cr_2O_3	[398]
$\text{Na}_2\text{O}/\text{Nb}_2\text{O}_5/\text{SiO}_2$	ZrO_2	[388]
$\text{PbO}/\text{ZrO}_2/\text{SiO}_2$	TiO_2	[358]
$\text{K}_2\text{O}/\text{BaO}/\text{Bi}_2\text{O}_3/\text{Ta}_2\text{O}_5/\text{CeO}_2/\text{SiO}_2$	ZrO_2	[410]
$\text{Li}_2\text{O}/\text{Bi}_2\text{O}_3/\text{ZrO}_2/\text{SiO}_2$	Cr_2O_3	[399]
Borosilicate glasses		
$\text{CaO}/\text{B}_2\text{O}_3/\text{SiO}_2$	ZrO_2	[411]
$\text{BaO}/\text{Fe}_2\text{O}_3/\text{B}_2\text{O}_3/\text{SiO}_2$	ZrO_2	[412,413]
Alumosilicate glasses		
$\text{Li}_2\text{O}/\text{Al}_2\text{O}_3/\text{SiO}_2$	ZrO_2	[355,382,414]
	TiO_2	[35,355,415]
	$\text{ZrO}_2 + \text{TiO}_2$	[401,402,416,417]
	$\text{SnO}_2 + \text{ZrO}_2$	[396]
	Ta_2O_5	[406]
	P_2O_5	[100,355]
$\text{Li}_2\text{O}/\text{CaO}/\text{Al}_2\text{O}_3/\text{SiO}_2$	ZrO_2 , TiO_2	[359]
$\text{Li}_2\text{O}/\text{CaO}/\text{MO}/\text{Al}_2\text{O}_3/\text{SiO}_2$	$\text{ZrO}_2 + \text{TiO}_2$	[116]
$\text{MgO}/\text{Al}_2\text{O}_3/\text{SiO}_2$	TiO_2	[89,352,361-367]
	ZrO_2	[41,47,89,360,378,389,390,394]
	$\text{ZrO}_2 + \text{TiO}_2$	[417,418]
	$\text{ZrO}_2 + \text{SnO}_2$	[419]
	CeO_2	[360]
	Nb_2O_5	[405]
$\text{CaO}/\text{Al}_2\text{O}_3/\text{SiO}_2$	ZrO_2	[420]
$\text{SrO}/\text{Al}_2\text{O}_3/\text{SiO}_2$	ZrO_2 , TiO_2	[367]
$\text{ZnO}/\text{Al}_2\text{O}_3/\text{SiO}_2$	ZrO_2	[368]
	ZrO_2 , TiO_2	[368]
$\text{CaO}/\text{MgO}/\text{Al}_2\text{O}_3/\text{SiO}_2$	Cr_2O_3	[400]
	TiO_2 , Cr_2O_3	[369]
	ZrO_2	[380]
$\text{R}_2\text{O}/\text{MgO}/\text{CaO}/\text{Al}_2\text{O}_3/\text{SiO}_2$	TiO_2 , Fe_2O_3 , Cr_2O_3	[353]
	ZrO_2 , TiO_2 , P_2O_5	[356]
$\text{R}_2\text{O}/\text{R}'_2\text{O}/\text{Al}_2\text{O}_3/\text{SiO}_2$	TiO_2 , ZrO_2 , SnO_2	[370]
$\text{ZnO}/\text{MgO}/\text{Al}_2\text{O}_3/\text{SiO}_2$	ZrO_2	[46]
	$\text{ZrO}_2 + \text{TiO}_2$	[421]
$\text{ZnO}/\text{Y}_2\text{O}_3/\text{MgO}/\text{Al}_2\text{O}_3/\text{SiO}_2$	ZrO_2	[379]
	$\text{ZrO}_2 + \text{TiO}_2$	[421]
$\text{Y}_2\text{O}_3/\text{MgO}/\text{Al}_2\text{O}_3/\text{SiO}_2$	ZrO_2	[390,391]
$\text{SrO}/\text{BaO}/\text{ZnO}/\text{SiO}_2$	ZrO_2	[392]
	$\text{ZrO}_2 + \text{TiO}_2$	[422]
	SnO_2	[395]
$\text{AO}/\text{Al}_2\text{O}_3/\text{SiO}_2/\text{B}_2\text{O}_3$ (A=Mg, Ca, Ba)	TiO_2 , ZrO_2 , Cr_2O_3	[371]
$\text{MgO}/\text{CaO}/\text{B}_2\text{O}_3/\text{Al}_2\text{O}_3/\text{ZrO}_2/\text{SiO}_2$	TiO_2	[372]
Alumoborate glasses		
$\text{BaO}/\text{Al}_2\text{O}_3/\text{B}_2\text{O}_3$	ZrO_2 , TiO_2	[373]
Fluorosilicate glasses		
$\text{MgO}/\text{Al}_2\text{O}_3/\text{SiO}_2/\text{F}$	TiO_2 , ZrO_2	[423]
$\text{MgO}/\text{Al}_2\text{O}_3/\text{SiO}_2/\text{F}$	ZrO_2 , V_2O_5	[404]
$\text{K}_2\text{O}/\text{MgO}/\text{Al}_2\text{O}_3/\text{B}_2\text{O}_3/\text{SiO}_2/\text{F}$	TiO_2	[374]
	TiO_2 , ZrO_2	[375]
$\text{K}_2\text{O}/\text{MgO}/\text{CaO}/\text{Al}_2\text{O}_3/\text{B}_2\text{O}_3/\text{SiO}_2/\text{F}$	TiO_2	[376]
$\text{CaO}/\text{SrO}/\text{BaO}/\text{Nb}_2\text{O}_5/\text{B}_2\text{O}_3/\text{SiO}_2/\text{F}$	ZrO_2 , Cr_2O_3 , CeO_2	[393]
Phosphosilicate glasses		
$\text{CaO}/\text{Al}_2\text{O}_3/\text{SiO}_2/\text{P}_2\text{O}_5/\text{F}$	TiO_2 , ZrO_2	[377]
$\text{K}_2\text{O}/\text{MgO}/\text{CaO}/\text{Al}_2\text{O}_3/\text{B}_2\text{O}_3/\text{SiO}_2/\text{P}_2\text{O}_5/\text{F}$	ZrO_2	[380]

Au⁺ during melting [244]. They are dissolved in water or acetone, added to the glass batch, and homogeneously distributed in the glass melt during the melting process. Tiny quantities of, e.g., Pt react to form the metal and (probably) physically dissolved oxygen. Alternatively, Pt⁴⁺ reacts with impurities such as Fe²⁺ which are then oxidized to, e.g., Fe³⁺. Au and Ag require the addition of compounds which undergo redox reactions with the oxidized metals during cooling, one typical compound is Sb, which occurs as Sb³⁺ and Sb⁵⁺ in glass melts. These compounds form an equilibrium with physically dissolved oxygen which shifts towards Sb³⁺ and O₂ with increasing temperatures (a.k.a. the “fining reaction” where the O₂ forms bubbles) [344]. At the maximum temperature applied during glass melting, antimony mainly occurs as Sb³⁺ in most glass compositions. The equilibrium stated in Eq. (17) occurs in the presence of Au⁺:



This equilibrium is at the left side of Eq. (17) at the maximum applied glass melting temperature and shifts to the right-side during cooling [156]. As the formation of metallic Au particles requires a nucleation process, kinetics play an important part. Especially during thermal treatment at temperatures slightly above T_g, such glasses obtain an increasingly red colour which is caused by the formation of Au particles with diameters ranging from 5 to 50 nm [156,345].

A detailed study of Ag nanoparticle formation [346] was performed by exposing a soda-lime silicate glass (float glass) to an ion exchange with an AgNO₃/NaNO₃ melt. The UV-vis and photoluminescence spectroscopy results enabled to conclude that Ag occurs as Ag⁰ atoms, after the Ag⁺ in the melt is reduced, and forms Ag-dimers which subsequently grow to Ag nanoparticles.

A special case of nucleation achieved by metallic nano particles are the photo thermal refractive (PTR) glasses. Here metallic Ag nanoparticles are formed by the photo reaction of Ce³⁺ and Ag⁺ stated in Eq. (18) which requires UV light.



The Ag nano particles subsequently form during a thermal treatment at temperatures slightly above T_g and cause a yellow coloration. They act as nuclei for the crystallization of NaF or CaF₂ crystals, preferably 50 to 100 nm in diameter, during a second thermal treatment at higher temperatures. There is much literature in this field [347-350] which includes the fabrication of Bragg gratings [348] and other optical devices.

The most frequently applied oxidic nucleation agents are TiO₂ [351-377] ZrO₂ [41,46,47,355,356,359-361,368,370-373,375,379-395], SnO₂ [370,395,396] and Cr₂O₃ [353,354,369,371,393,398-401] or mixtures of the above mentioned oxides [116,396,401,402], which should be added in concentrations of a few mol%. They seem to be fairly versatile and can be applied to various glass systems. V₂O₅ [403,404], Nb₂O₅ [403,405], Ta₂O₅ [406] and P₂O₅ [100,355,356,383,407,408] have also been reported to act as nucleation agents in some silicate glasses such as the Li₂O/BaO/SiO₂ system.

Table 1 provides an overview of glass systems and respectively suitable oxidic nucleation agents reported in the literature.

One of the most frequently studied systems has the base glass composition Li₂O•2 SiO₂, i.e., stoichiometric lithium disilicate Li₂Si₂O₅, in which ZrO₂ [383-385], TiO₂ [383], P₂O₅ [383,424,425] and Cr₂O₃ [397] have been reported to act as nucleating agents. Stoichiometric Li₂O•2 SiO₂ glasses nucleate in the bulk and do not show phase separation in contrast to other compositions containing the above-mentioned nucleating agents. Stoichiometric Li₂O•2 SiO₂ glasses are used as a model glass system with respect to the fundamentals of nucleation and crystal growth and the effect of minor additive concentrations. Apart from that, this glass system is investigated because glass-ceramics based on it exhibit the high strength, translucency and chemical durability required for some dental applications. For example, the commercial Li₂O•2SiO₂ based material “Empress 2™” was reported to show a fracture toughness of 3.3 MPa•m^{1/2} and a flexural strength of 400 MPa or more [42,178,426]. A typical molar composition for a dental glass-ceramic based on Li₂O•2 SiO₂ is 22.96 Li₂O•2.63 K₂O•2.63 Al₂O₃•71.78 SiO₂ (in mol%) where the molar SiO₂/Li₂O ratio is much larger than in the stoichiometric Li₂O•2SiO₂ base glass. Some glass compositions containing 1 to 3 mol% of the nucleating agents TiO₂, ZrO₂ or P₂O₅ show phase separation into a Li₂O- and an SiO₂-rich phase when cooled with rates common for laboratory experiments [383]. The first crystalline phase formed during thermal treatment (at 700 to 800 °C) when adding P₂O₅ and/or ZrO₂ is lithium metasilicate (Li₂SiO₃), while adding TiO₂ leads to the formation of both Li₂SiO₃ and Li₂Si₂O₅. At 900 °C, mixtures of Li₂SiO₃ and Li₂Si₂O₅ are formed after adding P₂O₅ and ZrO₂, while adding TiO₂ solely causes Li₂Si₂O₅ to form. The initial formation of Li₃PO₄ [424] and subsequent crystallization of Li₂SiO₃ and Li₂Si₂O₅ was reported in another P₂O₅ containing composition (30 Li₂O•60 SiO₂•2 ZnO•3 K₂O•1 CaO•4 P₂O₅). This highlights that the nucleating agent type may have a great effect not only on the required temperature/time schedule but also on the phases formed during thermal treatment. This was also shown for the composition 26.0 Li₂O•3.0 K₂O•3.0 Al₂O₃•68.0 SiO₂ where thermal treatment at 700 to 900 °C solely caused Li₂SiO₃ to form, while solely Li₂Si₂O₅ was formed at 900 °C in a similar composition containing only 1 mol% P₂O₅ (26.0 Li₂O•2.5 K₂O•2.5 Al₂O₃•68.0 SiO₂ 1 P₂O₅) [425]. Two very different explanations for the effect of P₂O₅ in this system are given in the literature: the first is that P₂O₅ triggers a phase separation and nucleation is then said to occur at the interface between the two amorphous phases. The second states that Li₃PO₄ is initially formed and the other phases grow epitaxially onto these nuclei.

Nucleation agents for borosilicate glasses have been studied to a much lesser extent, probably because such glass-ceramics are not produced commercially so far to the best of our knowledge. Nevertheless, ZrO₂ is also a favorable nucleation agent in borosilicate glasses [411-413].

Other frequently studied systems are aluminosilicate glasses where the two base systems Li₂O/Al₂O₃/SiO₂ [116,351,355,382,396,401,402,406,414-416] and MgO/Al₂O₃/SiO₂ [41,46,47,277,352,361,378,379,389,390,394,405,417-419,427] have received special attention including detailed studies using high resolution TEM. The Li₂O/Al₂O₃/SiO₂ system is of high scientific and commercial interest because it enables to prepare glass-ceramics with zero thermal expansion. The base system is

modified by comparatively small concentrations (<3 mol%) of various additives for most applications, usually by Sb_2O_5 as a fining agent and furthermore by Na_2O , CaO , BaO , MgO or ZnO [30–32,116,351,382,396,401,402,414–416], which may partially substitute Li_2O . This is primarily done to tune the thermal expansion behavior but also to adapt optical properties like the transparency, which is of special importance to applications like furnace windows. The $\text{MgO}/\text{Al}_2\text{O}_3/\text{SiO}_2$ system strictly requires the use of nucleation agents because the most favorable glass compositions otherwise solely show surface crystallization. Favorable nucleation agents reported in the literature are ZrO_2 , TiO_2 , CeO_2 and Nb_2O_5 as stated in Table 1. Using ZrO_2 as the nucleation agent is frequently described [41,47,378,394,399] because it is more effective than TiO_2 . EXAFS measurements report that glasses with the mol% composition $15.6 \text{ MgO} \bullet 8.4 \text{ Al}_2\text{O}_3 \bullet 74 \text{ SiO}_2 \bullet 1.9 \text{ ZrO}_2$ [394] contain sevenfold coordinated Zr^{4+} connected to Si (Mg, Al) polyhedra which then rearrange to tetragonal ZrO_2 nanocrystals in which Zr^{4+} is coordinated eightfold with oxygen. Using TiO_2 as a nucleation agent [89,352,361–366] usually leads to a primary phase separation and the formation of droplets enriched in TiO_2 , Al_2O_3 and MgO . Nano crystals in the solid solution system $\text{TiAl}_2\text{O}_5\text{--MgAl}_2\text{O}_4$ are then formed slightly above T_g [364,365] and trigger the formation of quartz solid solutions at higher temperatures. Phase separation could not be proven in slightly different compositions (22.2 MgO $22.2 \text{ Al}_2\text{O}_3$ 55.5 SiO_2 + 11.1 or 15.5 mol\% TiO_2) using NMR spectroscopy and TEM [366] although the same solid solution precipitated. Increasing the TiO_2 concentration (>7 mol%) leads to an increased concentration of fivefold coordinated Al^{3+} up to 21.7 %, more sixfold coordinated Al^{3+} and the formation of Ti–O–Al bonds between fivefold coordinated Ti^{4+} and higher coordinated Al^{3+} [362,363,366]. The main interest in this glass system is aimed at its mechanical properties, especially their high mechanical strength (up to 1 GPa), high hardness (up to 13 GPa) and high Young's Modulus (up to 150 GPa) [46,47].

If both TiO_2 and ZrO_2 are added to these base glasses, the first step during thermal treatment at a temperature slightly above T_g is the formation of amorphous droplets enriched in ZrO_2 , TiO_2 or Al_2O_3 . Then ZrTiO_4 crystals 3 to 4 nm in diameter precipitate inside the droplets [416] while the excess Al_2O_3 is pushed out and forms an amorphous shell [402]. Subsequently, quartz solid solutions crystallize first in both systems, sometimes epitaxial to the ZrTiO_4 nuclei [116]. Epitaxial growth on formed nuclei has been stated to occur in many glass systems for decades but was rarely proven. The recent improvements of TEM have enabled to prove the epitaxial growth of quartz solid solution crystals in both the $\text{Li}_2\text{O}/\text{Al}_2\text{O}_3/\text{SiO}_2$ and the $\text{MgO}/\text{Al}_2\text{O}_3/\text{SiO}_2$ systems using selected area electron diffraction. For example, the formation of one quartz solid solution crystal in the $\text{Li}_2\text{O}/\text{Al}_2\text{O}_3/\text{SiO}_2$ system requires 100 to 1000 ZrTiO_4 nano crystals [401]. The above-mentioned nucleation agents are nevertheless effective in the $\text{MgO}/\text{Al}_2\text{O}_3/\text{SiO}_2$ and $\text{Li}_2\text{O}/\text{Al}_2\text{O}_3/\text{SiO}_2$ systems. The $\text{MgO}/\text{Al}_2\text{O}_3/\text{SiO}_2$ system even allows the formation of quartz solid solution nanocrystals in the bulk [421]. There is some confusion in the literature concerning the nomenclature of quartz phases, we use the nomenclature proposed in Ref. [428] as it is suited to clarify the nomenclature. Hence transforming quartz solid solutions are denoted as “ α -quartz” for the low temperature phase and “ β -quartz” for the high temperature phase. Highly doped quartz solid solutions which do not transform are simply denoted as “quartz solid solutions”. For example, solid solutions highly doped with Li_2O and Al_2O_3 are β -quartz solid solutions whereas the composition $\text{Mg}_{0.5}\text{AlSiO}_4$ crystallizes to form an α -quartz solid solution [429,430] according to synchrotron XRD. Most quartz-related phases crystallized from MAS glasses are not as highly doped as $\text{Mg}_{0.5}\text{AlSiO}_4$ ($\approx 10 \text{ mol\%}$ of both MgO and Al_2O_3), do not show a phase transition and are hence just denoted as “quartz solid solutions”. If they are doped with $\leq 1 \text{ mol\%}$ MgO and Al_2O_3 , they do show a phase transition and are respectively denoted as α -quartz at low temperatures and as β -quartz at high temperatures.

ZrO_2 causes a fairly similar mechanism in $\text{Li}_2\text{O}/\text{Al}_2\text{O}_3/\text{SiO}_2$ glasses [414] as mixtures of TiO_2 and ZrO_2 : a liquid/liquid phase separation first forms tiny ZrO_2 and Al_2O_3 enriched droplets in which cubic or tetragonal ZrO_2 crystallizes with sizes of up to 3.5 nm and is surrounded by an Al_2O_3 enriched layer. If TiO_2 is the nucleating agent in $\text{Li}_2\text{O}/\text{Al}_2\text{O}_3/\text{SiO}_2$ glasses, the same principal mechanism causes amorphous droplets enriched in TiO_2 , Al_2O_3 and (if present) ZnO to form where TiO_2 then supposedly crystallizes as anatase [415] or pseudobrookite [431], depending on the composition. Although this phase is hard to detect by XRD in these samples because its peaks are extremely broadened due to the small crystallite size and overlap with peaks of the also present quartz solid solution, recent studies using SAED [415] proved the occurrence of anatase.

Reports describing the nucleating effect of additives in borate glasses do not exist to the best of our knowledge. In analogy to borosilicate glasses, few studies on the effect of nucleating agents on alumoborate glasses have been published so far. One example is the $\text{BaO}/\text{Al}_2\text{O}_3/\text{B}_2\text{O}_3$ system which mainly shows surface crystallization while only a few crystals form in the bulk [189,191]. Adding ZrO_2 or/and TiO_2 results in a fairly fine microstructure, proving that they act as nucleating agents in this system [373]. $\text{BaAl}_2\text{B}_2\text{O}_7$ is of particular interest because it is one of the few phases with a negative thermal expansion [189] and can be crystallized from glasses with the same stoichiometry in high volume concentrations [189,191].

Nucleation agents can also be applied to modify a bulk crystallized microstructure. For example, TiO_2 , ZrO_2 , Cr_2O_3 , CeO_2 or V_2O_5 have been used to achieve a more fine grained structure in fluoroalumosilicate glass-ceramics [377,380], predominantly produced to crystallize layered aluminosilicates such as mica or muscovite [374–376,404,423]. These glass-ceramics are of interest due to, e.g., their machinability which makes them suitable for rapid prototyping as they can be shaped using conventional hard metal tools. They are additionally biocompatible so another application is bone replacement in plastic/restorative surgery. The combination of biocompatibility and good machinability is favorable for plastic surgery [432–434]. Table 1 illustrates that there are numerous systems in which various nucleating agents lead to bulk crystallization. General rules which nucleation agent is successful for a particular glass composition cannot be given at this point, but TiO_2 and ZrO_2 (or a combination of both) are often the first choice for experimentation. SnO_2 also acts as a nucleation agent and can be combined with $\text{TiO}_2/\text{ZrO}_2$ or a combination of both. Sn occurs as Sn^{2+} and Sn^{4+} in glasses but only the formation of Sn^{4+} containing compounds such as SnO_2 , ZrSnO_4 or $\text{ZrTi}_{1-y}\text{Sn}_y\text{O}_4$ solid solutions [396,435] leads to nucleation. SnO_2 functions as a fining agent at high temperatures and hence the redox equilibrium $\text{Sn}^{4+}/\text{Sn}^{2+}$ is shifted to the reduced state with increasing temperatures. If As_2O_5 or Sb_2O_5 are present in addition to fining agents, another redox equilibrium following Eq. (19) is formed and is shifted to the left with decreasing temperatures from the highest applied melting temperature to the nucleation temperature [436].



Hence Sn predominantly occurs as Sn^{2+} at the nucleation temperature and the effect of SnO_2 is not as pronounced as might be expected. This is of special importance for aluminosilicate glasses, which require melting temperatures of 1600 °C or higher.

The success of adding of ZrO_2 and TiO_2 is visualized by the homogeneous microstructure in Fig. 15 which shows a bright-field TEM image of a $\text{Li}_2\text{O}/\text{Al}_2\text{O}_3/\text{SiO}_2$ based glass with numerous ZrTiO_4 crystals [416].

3.3. Use of Nucleation Inhibitors

The term “nucleation inhibition” is quite common in crystal engineering [438,439], but by far not as usual in glass science. To the best of our knowledge, the term “nucleation inhibitor” was first used concerning glass crystallization by J. H. Jean and T. K. Gupta [440,441]. Nucleation inhibitors are compounds which decrease the nucleation rate, and often the crystal growth velocity, while the induction period is frequently increased. They are usually added to a glass in comparatively small concentrations in the range of 0.5 to 2 mol%. The effect of nucleation inhibition in glasses should be related to a given viscosity, i.e., melts of the same viscosity are compared with respect to their nucleation rates. If these rates are notably smaller in the melt to which the compound was added, it can be denoted as a nucleation inhibitor for the given composition. It should be noted that a smaller nucleation rate at the same temperature should **not** be sufficient to describe a compound to be a “nucleation inhibitor”.

Typical compounds showing this effect in silicate glasses are La_2O_3 [442] and Al_2O_3 [442], but also ZrO_2 [443], TiO_2 [442], Nb_2O_5 [444,445], Ta_2O_5 [444,445], CeO_2 [446] and Y_2O_3 [446]. While it may seem surprising that the well-known nucleating agents ZrO_2 and TiO_2 can also act as nucleation inhibitors, it should be noted that, e.g., >4 mol% $\text{TiO}_2 + \text{ZrO}_2$ are necessary for an effective nucleation in the system $\text{MgO}/\text{Al}_2\text{O}_3/\text{SiO}_2$, while nucleation inhibition is achieved by additions ≤ 2 mol%. The above mentioned compounds increase the viscosity of a melt [442-446] and should hence decrease both nucleation rates and crystal growth velocities at a given temperature. As stated above, this alone is insufficient for nucleation inhibition. Nevertheless, the increase in viscosity may cause a smaller difference between the T_g and the T_l which results in smaller thermodynamic driving forces (ΔG_v , see Eqs. (1) to (4)). As the nucleation rate is usually highest at temperatures slightly above T_g , a decrease of this difference directly leads to a decrease of the nucleation rate at the same viscosity. This effect should be superimposed by numerous other effects such as the introduction of further components to a melt which should make nucleation, i.e., ordering the structure, more difficult. The extent of the latter effect strongly depends on the added compounds and their diffusivities. Table 2 summarizes nucleation inhibitors reported in the literature for various glass systems.

To the best of our knowledge, the first report describing a decrease of the nucleation rate by adding small concentrations of other compounds was published in 1930 by G. W. Morey for alumina added to soda-lime-silica glass [447]. A later report by K. Matsusita and S. Sakka from 1975 described the effect for borosilicate glasses [149]. DTA profiles were used to show that the temperature difference between the exothermic peak and the temperature attributed to a viscosity of 10^{10} dPas usually increases when 3 mol% MO_x were added to two glass compositions in the $\text{Li}_2\text{O}/\text{SiO}_2$ system.

Since then, numerous studies on the decelerating effect of additives on nucleation have been published. Table 2 shows that the $\text{Li}_2\text{O} \cdot 2\text{SiO}_2$ system has been intensively investigated using numerous additives such as Al_2O_3 [149,442], Y_2O_3 [446], La_2O_3 [149,442], TiO_2 [149,442], ZrO_2 [149,383,443], CeO_2 [446], Nb_2O_5 or Ta_2O_5 [444,445]. J. H. Jean and T. K. Gupta reported Al_2O_3 [440,441] and Ga_2O_3 [440] to act as nucleation inhibitors in the commercial borosilicate glass Corning 7740. Al_2O_3 [447,448] and B_2O_3 [448] were studied in commercial soda lime silicate glass compositions. Y_2O_3 [450] and La_2O_3 [448,450] were reported as nucleation inhibitors in the glass system $\text{ZnO}/\text{B}_2\text{O}_3/\text{SiO}_2$. La_2O_3 acts as nucleation inhibitor in glasses with the base composition $\text{Li}_2\text{O}/\text{Al}_2\text{O}_3/\text{SiO}_2$ which are

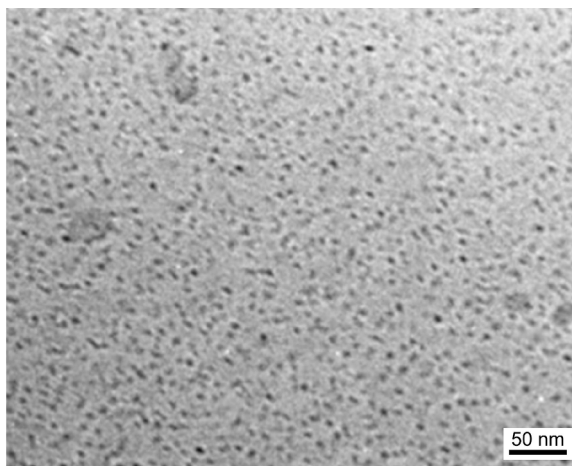


Fig. 15. Bright-field TEM image (75 keV) of a $3.5 \text{ Li}_2\text{O} \cdot 0.15 \text{ Na}_2\text{O} \cdot 0.2 \text{ K}_2\text{O} \cdot 1.15 \text{ MgO} \cdot 0.8 \text{ BaO} \cdot 1.5 \text{ ZnO} \cdot 20 \text{ Al}_2\text{O}_3 \cdot 67.2 \text{ SiO}_2 \cdot 2.6 \text{ TiO}_2 \cdot 1.7 \text{ ZrO}_2 \cdot 1.2 \text{ As}_2\text{O}_3$ glass cerammed at 750 °C for 1 h. Reprinted from Ref. [402] with permission from the American Chemical Society.

Table 2
Nucleation inhibitors for various glass systems.

Glass System	Nucleation Inhibitor	Reference
Li ₂ O/SiO ₂	Al ₂ O ₃ , La ₂ O ₃ , TiO ₂	[442]
	ZrO ₂	[383,443]
	Nb ₂ O ₅ , Ta ₂ O ₅	[444,445]
	CeO ₂ , Y ₂ O ₃	[446]
	Al ₂ O ₃ , In ₂ O ₃ , ZrO ₂	[149]
Borosilicate	Ga ₂ O ₃	[440]
	Al ₂ O ₃	[440,441]
Na ₂ O/Al ₂ O ₃ /SiO ₂	Al ₂ O ₃	[447]
	B ₂ O ₃ , Al ₂ O ₃	[448]
ZnO/B ₂ O ₃ /SiO ₂	La ₂ O ₃	[449,450]
	Y ₂ O ₃	[450]
Li ₂ O/Al ₂ O ₃ /SiO ₂	La ₂ O ₃	[451]
CaPO ₃	SiO ₂	[452]
Na ₂ O/MgO/CaO/P ₂ O ₅	TiO ₂	[453]
Fluoride phosphate	MgF ₂	[454]

commonly used for the preparation of zero thermal expansion glass-ceramics. In phosphate glasses, such as Ca metaphosphate, SiO₂ [452] is a known nucleation inhibitor, while in the Na₂O/CaO/MgO/P₂O₅ system TiO₂ [453,455] was reported to decelerate nucleation. In fluoride phosphate glasses, MgF₂ [454] acts as nucleation inhibitor.

The most frequently studied system Li₂O•2 SiO₂ [442–447] will now be discussed in greater detail to illustrate the experiments allowing to conclude on nucleation inhibition. Fig. 16 shows an optical (polarization) micrograph of a glass of the Li₂Si₂O₅ composition thermally treated in two steps; the first was performed to achieve nucleation while the second, a.k.a. the development, was performed to grow the crystals to an observable size [456].

Table 3 shows steady state nucleation rates of the stoichiometric Li₂O•2 SiO₂ glass compared to that glass with additions of 1 or 2 mol% Al₂O₃, TiO₂, ZrO₂, La₂O₃, Nb₂O₅, Ta₂O₅, Ce₂O₃ and Y₂O₃. The supplied temperatures were those attributed to a viscosity of 10¹³ dPa•s [442–446], i.e., the nucleation rates were determined for comparable viscosities (*not* the same temperatures). The nucleation rates are much smaller with the additives and further decrease if their concentration is doubled. The most effective nucleation inhibitor in this series is Y₂O₃. The cations in all these compounds have a valency of at least +3, but which component is most effective remains unknown so far as the literature contains insufficient data, especially not from different systems.

Adding Al₂O₃, ZrO₂ or La₂O₃ to glasses in the BaO/SiO₂ system enables to produce glasses with higher BaO concentrations and to subsequently prepare glass-ceramics containing, e.g., Ba₂SiO₄ or other barium silicates with high BaO concentrations by controlled crystallization. Such glass-ceramics are highly interesting because of their high CTEs, which are, e.g., required for crystallizing sealing glasses suitable for applications such as high temperature fuel cells [27,457–459, 27]. Al₂O₃ and La₂O₃ also serve as nucleation inhibitors in both the BaO/SrO/ZnO/SiO₂ system, e.g., used for low CTE crystallizing glasses [28], and the BaO/ZnO/SiO₂ system, e.g., used for high CTE crystallizing glass seals. They enable the preparation of glasses closer to the crystal stoichiometry of (Ba, Sr)Zn₂Si₂O₇ or BaZn₂Si₂O₇ [460–462] which would not form continuous networks as stoichiometric compounds, hence crystallize during quenching and thus do not enable a controlled crystallization.

The simplest approach to decelerate glass crystallization during cooling is increasing the network former concentration. However, this will also slow down crystal growth after nucleation. If, however, a specific CTE like “> 14•10⁻⁶ K⁻¹” is required for a seal with high

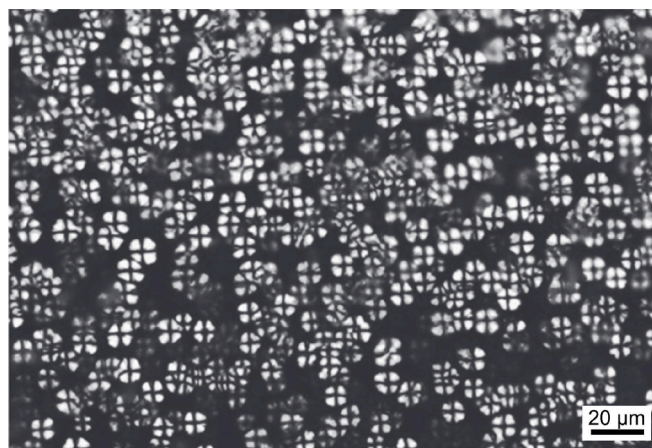


Fig. 16. Transmission optical microscopy image in cross-polarized contrast of a Li₂O•2SiO₂ glass thermally treated at 560 °C for 30 min, reprinted from Ref. [456] with permission from Elsevier.

Table 3Steady state nucleation rate as a function of the type and concentration of nucleation inhibitors at a viscosity of 10^{13} dPas.

Dopant	Concentration in mol%	Nucleation rate in $\text{mm}^{-3}\text{s}^{-1}$	Dopant	Concentration in mol%	Nucleation rate in $\text{mm}^{-3}\text{s}^{-1}$
none	0	16.90	La ₂ O ₃	1	0.75
Al ₂ O ₃	1	3.80		2	0.00
	2	0.50	Nb ₂ O ₅	1	0.95
TiO ₂	1	5.50		2	0.33
	2	1.36	Ta ₂ O ₅	1	0.93
ZrO ₂	1	0.86	Ce ₂ O ₃	1	3.30
	2	0.27		2	1.05
Y ₂ O ₃	1	0.33			

temperature alloys such as NiCrofer™ [83], the concentration of network formers must be kept small. Otherwise, the crystallized high CTE phase would have a too low volume concentration and the CTE of the material (crystal + residual glass) would be too small. In such cases, nucleation inhibitors can help to increase the glass forming region more effectively and hence solve the problem: nucleation is postponed without strongly affecting the crystal growth velocity nor the maximum degree of crystallization.

Another example where nucleation inhibitors may help is when a certain grain size fraction of a glass powder is used for sinter crystallization resulting in a certain mean crystal size. If the latter is too large for the desired application and, e.g., leads to insufficient mechanical properties, the logical step would be to reduce the grain size of the glass powder. However, now the glass powder may crystallize too fast and prevent a full densification via viscous flow. Adding nucleation inhibitors can solve this problem by suppressing crystallization until a full densification is achieved.

3.4. Effects of Phase Separation

Two main types of phase separation may generally occur: the first at temperatures above T_1 where two liquids of different chemical composition are thermodynamically stable. The second type occurs below T_1 and is denoted as metastable phase separation [463,464]. Here the two liquids of different chemical composition are not in a thermodynamic equilibrium because the thermodynamically stable state would be crystalline.

Glasses exhibiting stable phase separations have comparatively low viscosities [279-282], especially in comparison to glasses showing metastable phase separation. In the case of stable phase separation, the formed structures (e.g., droplets) can grow rapidly and may even show unstable growth fronts leading to the viscous fingering featured in Fig. 10. If the viscosity is low enough, a subsequent sedimentation into layers of differing composition is often observed as the liquids show different densities [465,466]. Cooling may then result in the formation of cracks between the layers due to the CTE mismatch. Glasses with stable phase separations are currently not suitable to prepare materials with advantageous properties. Interesting compositions for glass-ceramics show phase separation below T_1 , where the viscosity is usually high enough to prevent the formation of coarse structures and sedimentation. Sedimentation does not occur notably below T_1 , because the sedimentation velocity of a droplet is proportional to the square of its diameter and to the reciprocal viscosity. Phase separation below T_1 hence either leads to the formation of unconnected droplets embedded in a matrix as featured in Fig. 17 a) [467] or an interpenetrating microstructure as that presented in Fig. 17 b) [468]. The matrix in Fig. 17 a) is enriched in SiO₂ while the almost spherical droplets are enriched in Na₂O and B₂O₃ and vary from 50 to 180 nm in diameter. The size of the formed structures of the two glassy phases in Fig. 17 b) can be adjusted by the applied temperature/time schedule.

Sometimes multiple phase separations like that presented in the TEM-replica micrograph of Fig. 18 occur, especially, if a glass is

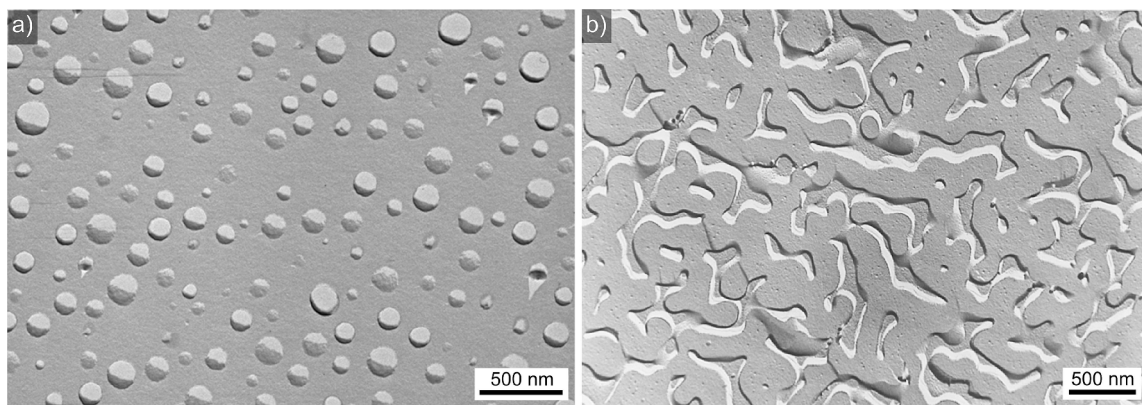


Fig. 17. TEM-replica micrographs of phase separated glasses. a) Droplet phase separation in a 3 Na₂O•37 B₂O₃•60 SiO₂ glass thermally treated at 680 °C for 5 h, reprinted from Ref. [475] with permission from John Wiley and Sons. b) Interpenetrating phase separation in a glass with the composition 6.5 Na₂O•33.5 B₂O₃•60 SiO₂, based on Ref. [468].

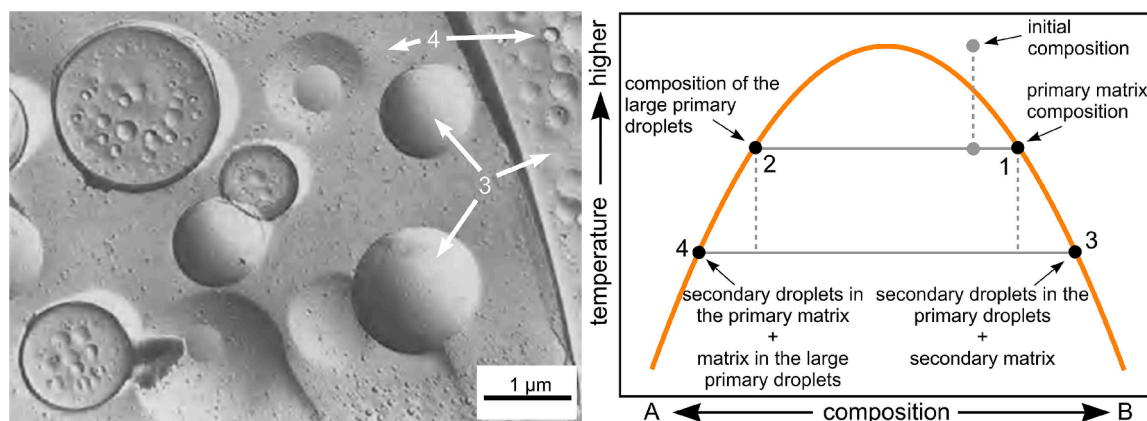


Fig. 18. TEM-replica micrograph of a multiple phase separated borosilicate glass and a schematic illustration of the miscibility gap and the phases formed during multiple phase separation. Left: reprinted from Ref. [675] with permission from Elsevier, right: redrawn based on Ref. [16].

cooled comparatively fast after it was thermally treated just below that critical temperature, below which metastable phase separation occurs. Further cooling to a temperature notably below the critical temperature results in the formation of small droplets both in the large droplets and in the matrix. The chemical developments are outlined in the principal phase diagram in Fig. 18. During cooling, the initial composition separates into the primary matrix composition 1, no longer present in the TEM-micrograph, and the large primary droplets of composition 2 still discernible in Fig. 18. After the second step of phase separation, the composition 3 is observed in the small secondary droplets inside the large droplets as well as the matrix. Composition 4 should occur in the small secondary droplets outside of the large primary droplets as well as the matrix inside the primary droplets. At such a temperature, the diffusivities are so high that they only allow the formation of two final compositions which each form a matrix as well as droplets due to the two-stage “multiple phase separation” illustrated in Fig. 18. Of course, these processes are not as discrete as outlined above and depend on the diffusion pathlengths: secondary phase separation does not occur near boundaries of the primary droplets because here the pathlengths are short enough to reach stable compositions during the primary phase separation. Strictly spoken, EDXS-maps or line scans should show chemical gradients around these boundaries. Multiple phase separations have been observed in different glass systems [469–472] and can be modified by supplying an appropriate temperature/time schedule [472].

For simple droplet phase separation, the droplets have either a higher or a lower viscosity than the matrix [16]. The by far best investigated glass system tending to phase separation is $\text{Na}_2\text{O}/\text{B}_2\text{O}_3/\text{SiO}_2$ [15,16,467,468,474–479]. Although this system is not suitable for the preparation of advantageous glass-ceramic materials, it is described here in detail because it is a favourable model system and allows some general conclusions.

The size of the formed structures can be increased by a thermal treatment below the highest temperature of the miscibility gap of the respective composition. It increases with time, in an initial stage proportional to $t^{1/2}$ and then follows the $t^{1/3}$ rule of Ostwald ripening if the droplets are embedded in a matrix of lower viscosity [16,480]. If the matrix viscosity is higher than the droplet viscosity, the exponent is smaller than $1/3$, i.e., the droplets grow much slower [475] due to the formation of a highly viscous shell around the SiO_2 depleted droplets [475,476]. For an interpenetrating microstructure, the exponent is larger than $1/3$ and may even approach unity [468], which is attributed to a Frenkel type behaviour, i.e., the coarsening takes place by viscous flow. The size and temperature of the miscibility gap can be tailored by the base glass composition and by additives. Replacing Na_2O by Li_2O opens the miscibility gap, while its replacement by K_2O closes the miscibility gap [477,481]. Small concentrations of Al_2O_3 will also close the gap [478]. Glasses in the $\text{Na}_2\text{O}/\text{B}_2\text{O}_3/\text{SiO}_2$ system are mainly utilized to prepare interpenetrating structures from which the $\text{Na}_2\text{O}/\text{B}_2\text{O}_3$ -rich phase is removed by chemical etching to produce the so called “Vycor glasses” which contain interconnected pore structures. They are either used as filters or the pores are filled with solutions or dispersions of nanocrystalline powders for analysis [482]. Alternatively, the pores can be collapsed by a thermal treatment to obtain a compact, transparent glass with an SiO_2 content $>96\%$ [479].

There are two principal possibilities for producing glass-ceramics from phase separated glasses: either the droplets or their matrix crystallize first. Droplet crystallization is more important as it enables to achieve crystals with approximately spherical morphology, independent of their growth mechanism, which show almost the same size as the initial droplets. Matrix crystallization [483] is advantageous, if a continuous crystalline phase is required, e.g., for ferroelectric glass-ceramics with a high ϵ_r . A certain concentration of network formers is necessary to melt such glasses. Phase separation occurs during cooling, or in an additional thermal treatment step, and, e.g., SiO_2 rich droplets are formed, consequently depleting the matrix in SiO_2 . Finally, a continuous ferroelectric phase encompassing the SiO_2 droplets is formed. This approach may facilitate the preparation of glass-ceramics with advantageous dielectric and piezoelectric properties. The microstructure is much more favorable than that resulting from a homogenous glass where ferroelectric crystals resulting from bulk nucleation are separated by amorphous SiO_2 . Here it should be mentioned that e.g. mechanical properties of glass-ceramics grown via viscous fingering have not been reported so far.

3.4.1. Effect of Phase Separation on Nucleation

The effect of phase separation on nucleation was controversially discussed in the 1960s and 1970s [480,484–486]. Three principal

hypotheses are currently taken into account [487]:

- (1) The boundary between the two amorphous phases plays a decisive role and is the locus where nucleation occurs.
- (2) The chemical composition changes are decisive and one formed composition, also somewhere along a gradient, is closer to that of the formed crystal than all others.
- (3) A nucleus of a composition different from that of the finally precipitated crystal is formed in one of the amorphous phases and triggers the crystallization of another phase or other phases.

The formation of a nucleus with a metastable composition or epitaxial growth on this nucleus is assumed with regard to hypothesis (3) [487].

It should be noted that the experiments concerning the effect of phase separation were mainly performed using isochemical or close to isochemical glasses. The most frequently studied $\text{Li}_2\text{O}/\text{SiO}_2$ system [148,480,484–489] does not allow detailed TEM studies due to its sensitivity to electron radiation damage. One observation is that coarser structures in phase separated glasses do not exhibit significantly different nucleation rates [110]. This is sometimes considered to be proof that the boundary between the two amorphous phases does not play a decisive role [110]. The existence of a metastable phase was only proven in a few other cases, possibly due to the inability to perform reliable TEM studies. Hypothetically, a very low nucleation rate combined with a high crystal growth velocity in a homogeneous glass would lead to a single nucleus causing a large crystalline volume concentration, easy to detect using XRD, and a crystallization peak in DSC measurements. By contrast, the formation of only one nucleus in a phase separated glass would lead to only one crystallized droplet which would be almost impossible to detect.

From our point of view, the most reasonable explanation for an enhanced nucleation due to phase separation is the existence of a large variety of chemical compositions, not only of the matrix, droplets, or interpenetrating structures, but also along chemical diffusion gradients, e.g., formed around droplets in the surrounding matrix. Nucleation can take place along these gradients at loci with favourable compositions; this explanation was also favoured in a recent review by E. D. Zanotto in 2020 [110]. It should be noted that many of the recent reviews (e.g., [486,487,490]) on the effect of phase separation on nucleation are dedicated to isochemical or near isochemical compositions. Compositions in which minor components crystallize were not the focus of these reviews.

As outlined above, phase separation can also be triggered by adding nucleating agents which first cause the formation of droplets enriched in the respective agent which subsequently crystallize in these droplets. This has been described for ZrO_2 and TiO_2 . The main target phase finally precipitates as a third step [382,416] (see Chapter 3.1). Further effects of nucleating agents on phase separation include its suppression or promotion. ZrO_2 was reported to suppress phase separation in the $\text{Na}_2\text{O}/\text{B}_2\text{O}_3/\text{SiO}_2$ system [491] but promote it, and the crystallization of lithium silicates, in the $\text{Li}_2\text{O}/\text{Al}_2\text{O}_3/\text{SiO}_2/\text{P}_2\text{O}_5$ system [492]. Hence, the effect of very common nucleating agents strongly depends on the respective glass composition.

3.4.1.1. Spherical Crystal Volumes by Phase Separation. Other phase separating systems are more suitable for the production of glass-ceramics with advantageous properties. For example, some Ca-phosphosilicate glasses doped with F⁻ form droplets enriched in CaO and P_2O_5 [153,491–493] in which fluorapatite can be crystallized by further thermal treatment. Fig. 19 a) and b) show micrographs of phase separated droplets and the subsequently precipitated apatite crystals with faceted shapes [111]. Tailoring the droplet sizes enables to control the crystal size as the latter approximately have the size of the droplets, they are formed from [111].

If multiple nuclei form and grow within a droplet as is discernible in Fig. 20 a) and b), they are denoted as “multi core particles” which have predominantly been reported in oxyfluoride glasses [49,50,60,109,494–497]. Here a droplet phase enriched in fluoride

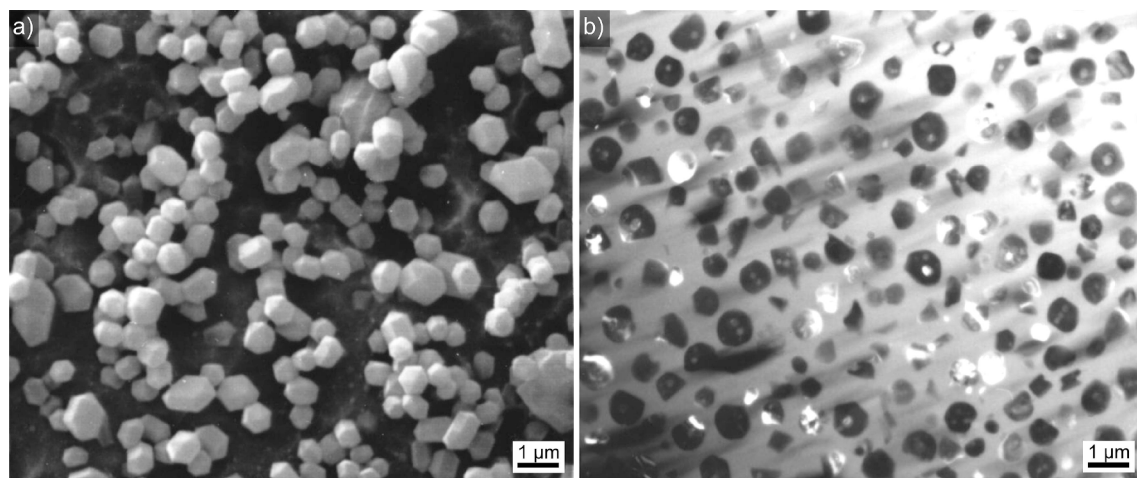


Fig. 19. Crystallization in amorphous droplets of phase separated glass. a) SEM micrograph of fluorapatite crystals precipitated from $\text{CaO}/\text{P}_2\text{O}_5$ enriched droplets of a glass with the composition $27.1 \text{ SiO}_2 \bullet 10.9 \text{ Al}_2\text{O}_3 \bullet 8.6 \text{ P}_2\text{O}_5 \bullet 19.4 \text{ CaO} \bullet 6.9 \text{ K}_2\text{O} \bullet 27.1 \text{ F}$, reprinted from Ref. [111] with permission from Elsevier. b) TEM-micrograph of the quenched and phase separated glass, reprinted from Ref. [111] with permission from Elsevier.

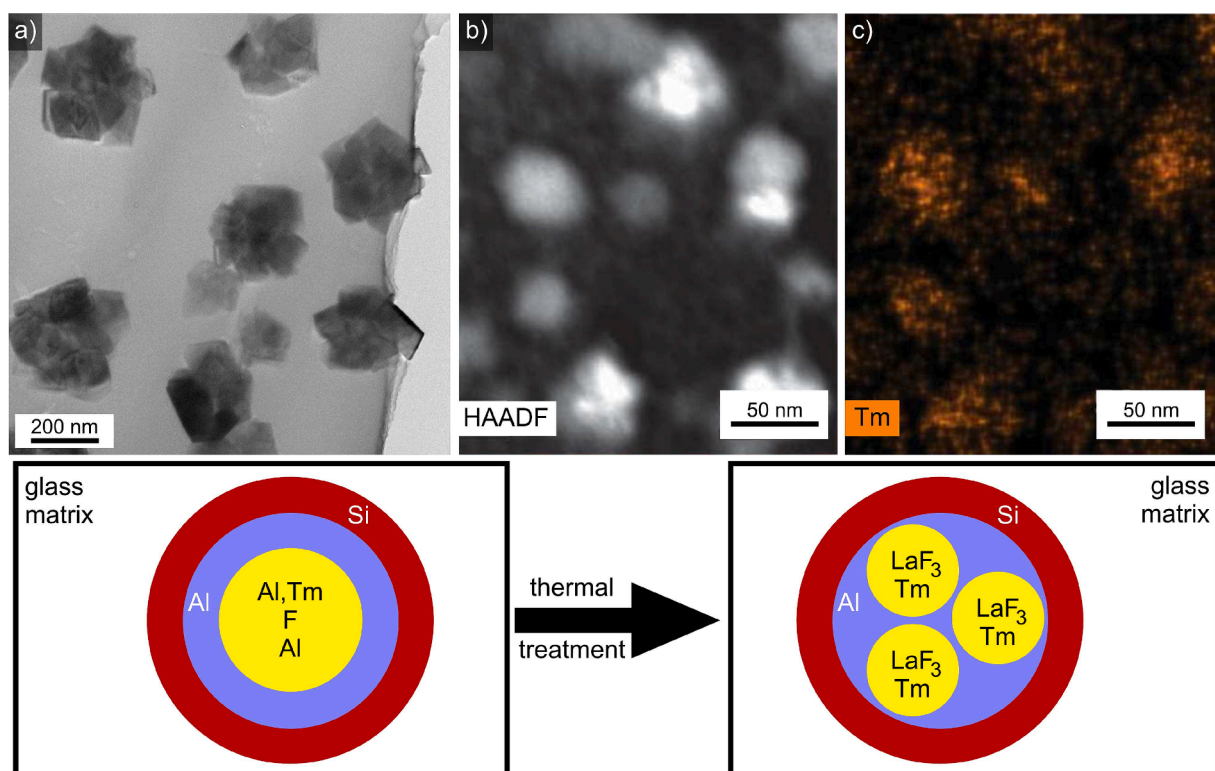


Fig. 20. Multicore particles grown after phase separation. a) TEM micrograph of magnetite multi core particles crystallized from a Fe-rich borosilicate glass, based on Ref. [501] b) TEM HAADF micrograph of $\text{LaF}_3/\text{TmF}_3$ multi core particles. c) TEM EDXS map of Tm in the same area. b) and c) are reprinted from Ref. [511] with permission from the Royal Society of Chemistry. A schematic based on Ref. [511] illustrating the formation of the multi core particles is presented below.

and, e.g., alkaline earth or rare earth oxides and a matrix enriched in silica is usually formed. Fluorides then crystallize in the droplet phase, sometimes in the form of nano sized single crystals [498]. Dopants such as Tm often accumulate in these crystals as shown in Fig. 20 c). D. Chen et al. reported that $\beta\text{-NaGdF}_4$ crystals formed in the droplets of an oxyfluoro silicate glass first formed multi-core particles which transformed into single crystals during further thermal treatment [495]. This could occur via Ostwald ripening or coalescence [499] and means any single crystals precipitated in droplets could have been initially multi-core particles. A schematic illustration of multicore particle formation is presented at the bottom of Fig. 20.

Ferrimagnetic phases precipitated from phase separated glasses are of special importance [499-502]. They can be formed from $\text{Na}_2\text{O}/\text{B}_2\text{O}_3/\text{Fe}_2\text{O}_3/\text{SiO}_2$ glasses [108,502] where droplets enriched in B_2O_3 and $\text{Fe}_2\text{O}_{3+x}$ are formed and crystallize to show numerous magnetite (Fe_3O_4) [502] nano crystals discernible in Fig. 20 a) [108,501-503]. Although the droplet size reached a few hundred nm in diameter, the individual crystals are much smaller. Each magnetite crystal contains a single magnetic domain and the samples show a very small hysteresis loop with a very small remanent magnetization if a magnetic field is applied [503]. Such materials have a wide application potential and have been proposed as catalysts [504,505], for biomedical applications, e.g., for hyperthermia [506-508], in magnetic resonance imaging, as ferrofluids, as gas-sensing materials [509] or as pigments [510].

Another example are glasses in the $\text{KF}/\text{ZnF}_2/\text{SiO}_2$ system which show droplet or interpenetrating structures after phase separation. Depending on the composition, ZnF_2 or KZnF_3 can be precipitated [56]. In both cases, the crystal size is fairly uniform and can be controlled by the size of the phase separation structures. Other phase separating oxyfluoride glasses are found in the system $\text{Na}_2\text{O}/\text{K}_2\text{O}/\text{BaF}_2/\text{BaO}/\text{Al}_2\text{O}_3/\text{SiO}_2$ where ErF_3 or SmF_3 additions as small as 0.05 mol% trigger a phase separation [512] not observed without them. Nano sized BaF_2 crystallizes during subsequent thermal treatment [512] and crystal growth is limited by the formation of SiO_2 enriched shells around them, independent of whether phase separation occurred or not. These crystals and their shells show a very narrow size distribution as proven by SAXS [513]. The effect of rare earth additives is similar in the $\text{Na}_2\text{O}/\text{K}_2\text{O}/\text{CaO}/\text{CaF}_2/\text{Al}_2\text{O}_3/\text{SiO}_2$ system where Tb^{3+} additions trigger the phase separation [41] and CaF_2 is crystallized to form the multicore particles presented in Fig. 20 b). A similar effect of small concentrations of rare earth elements on phase separation was also observed in the case of a glass with the base composition $59.3 \text{ SiO}_2 \bullet 12.3 \text{ CaO} \bullet 9.0 \text{ Na}_2\text{O} \bullet 5.3 \text{ K}_2\text{O} \bullet 3.7 \text{ Al}_2\text{O}_3 \bullet 0.02 \text{ Sb}_2\text{O}_3 \bullet 10.4 \text{ CaF}_2$ [109]. While the glass did not show phase separation without rare earths, adding only 0.1 mol% Tb_2O_3 led to phase separation as shown by TEM-replica micrographs. The phase separation observed after adding tiny quantities of rare earth fluorides is supposedly caused by an early clustering of rare earths [514-516] in the glass, detected by fluorescence spectroscopy including lifetime measurements and confirmed by molecular dynamics [515]. The clustering of rare earths in various glass compositions is also responsible for the so called

“concentration quenching” of the rare earth luminescence [517-519]. Adding the small concentration of only 0.05 mol% Sm_2O_3 to an oxide glass used to sinter crystallize $\text{Sr}_2\text{MgSi}_2\text{O}_7$ has been reported to increase in the mean crystallite size from 0.4 to 1.2 μm [520], but it is unclear whether this was caused by phase separation.

This field still contains surprising observations such as the $\text{Al}_2\text{O}_3/\text{K}_2\text{O}/\text{Na}_2\text{O}/\text{SiO}_2/\text{SrF}_2$ system where a glass with the composition $3.7 \text{ Al}_2\text{O}_3 \bullet 12.3 \text{ SrO} \bullet 5.3 \text{ K}_2\text{O} \bullet 8.0 \text{ Na}_2\text{O} \bullet 60.3 \text{ SiO}_2 \bullet 10.4 \text{ SrF}_2$ [513] shows phase separation leading to multi core particles, while other glasses in the composition series $(8 \text{ Al}_2\text{O}_3 \bullet 16 \text{ K}_2\text{O} \bullet 2 \text{ Na}_2\text{O} \bullet 74 \text{ SiO}_2) \bullet x \text{ SrF}_2$ (with $x = 0, 1, 2, 3, 4, 5$ and 6) do not exhibit phase separation at all [521].

3.4.1.2. Avoiding Spherical Crystal Volumes after Phase Separation. If droplets crystallize in phase separating systems, these domains usually assume more or less spherical morphologies composed either of single crystals, spherulites or aggregations of small crystals. The only way to avoid this is by preventing the formation of droplets, i.e., closing the miscibility gap. In some glass systems this can be achieved by comparatively small changes of the chemical composition, e.g., by adding small amounts of Al_2O_3 to glasses in the $\text{Na}_2\text{O}/\text{B}_2\text{O}_3/\text{SiO}_2$ system [478]. Adding Al_2O_3 or La_2O_3 may generally be a good first approach to address this issue in less well investigated systems.

There are systems where preventing phase separation is more complicated, especially those containing more than one network former. For example, CaO and P_2O_5 rich droplets form in the $\text{SiO}_2/\text{Al}_2\text{O}_3/\text{CaO}/\text{P}_2\text{O}_5/\text{Na}_2\text{O}/\text{K}_2\text{O}/\text{F}^-$ system during cooling and Ca-fluorapatite crystallizes during subsequent thermal treatments [111]. Ca-fluorapatite needles or rods should lead to advantageous mechanical properties, but the crystals precipitated in droplets are roughly spherical as shown in Fig. 19 and have to be avoided. However, chemical additives closing the miscibility gap in this system have not been reported to the best of our knowledge. Ref. [111] reports that rapid heating to 1200 °C, i.e., to a temperature where the glass no longer shows phase separation, leads to a dissolution of the droplets. Nucleation occurs nevertheless and the rod- or needle like apatite crystals shown in Fig. 21 subsequently grow, supposedly during heating [111].

3.5. Chemical Gradients Formed In Situ; Nano Crystallization

The chemical composition of a precipitated crystal and the melt match exactly in ideally isochemical systems. Hence the melt composition neither changes during nucleation nor during crystal growth and chemical gradients cannot form around growing crystals. This ideal case is basically impossible as no melt is ideally stoichiometric. There are several reasons why the crystal growth velocity depends on time: firstly, one component is always in excess as the composition is never ideally stoichiometric [522,523] which leads to a time dependent change of the crystal growth velocity. Secondly, the initial crystals do not show the ideal chemical composition, as described for the case of melts with the composition $\text{Na}_2\text{O} \bullet 2 \text{ CaO} \bullet 3 \text{ SiO}_2$ where the Na_2O concentration in the crystals is elevated [524,525]. This leads to a depletion of Na_2O in the vicinity of the crystals and hence to a deceleration of crystal growth. The crystals become stoichiometric in a later stage of crystallization. Furthermore, all melts contain some quantity of impurities, one of which is the omnipresent “water”, meaning OH^- groups. Water cannot be avoided by increasing the melting temperature, but its concentration can be minimized by bubbling the melt with dried gases and/or the addition of F^- [526]. Minimizing the water concentration is an important issue for the preparation of glasses and glass-ceramics intended for optical applications such as laser materials where water often leads to fluorescence quenching [526]. Amongst the phases assumed to add favourable properties if crystallized from glasses, only a few, such as mica or apatite, can incorporate water into their structure. Hence, water should be enriched at most growth fronts and can lead to the formation of pores once a local oversaturation is reached [527-529]. Although the diffusion coefficient of water is very high and comparable to that of Na^+ [287,530], this should result in a local decrease of the viscosity

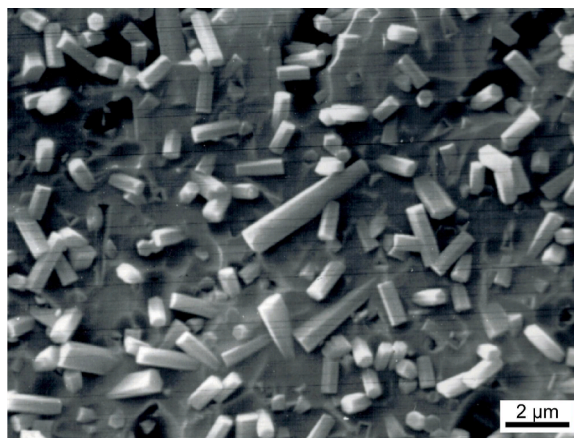


Fig. 21. SEM-micrograph of a glass-ceramic crystallized from a glass with the composition $27.1 \text{ SiO}_2 \bullet 10.9 \text{ Al}_2\text{O}_3 \bullet 8.6 \text{ P}_2\text{O}_5 \bullet 19.4 \text{ CaO} \bullet 6.9 \text{ K}_2\text{O} \bullet 27.1 \text{ F}^-$ produced by rapid heating to 1200 °C, reprinted from Ref. [111] with permission from Elsevier.

and hence most probably increases the diffusivity of all other glass components, in turn accelerating crystal growth. The accelerating effect of water on the crystal growth velocity has been described for various chemical systems [144,498,531–534].

Bubbling a glass with the composition $\text{Na}_2\text{O} \bullet 2 \text{CaO} \bullet 3 \text{SiO}_2$ increased the water concentration by a factor of 7.9 [498]. The effect of these different water concentrations is shown in Fig. 22: the maximum nucleation rate increased from 0.4 to $5.54 \bullet 10^5 \text{ mm}^{-3} \bullet \text{min}^{-1}$, whereas the temperature attributed to this maximum decreased from 603 to 574 °C. In both cases, the dependencies seem to be linear. The induction period of nucleation was also decreased and the crystal growth velocities were increased by about one order of magnitude (not shown in the Figure).

Bubbling a glass with the composition $\text{Li}_2\text{O} \bullet 2 \text{SiO}_2$ with steam led to an increase of the water concentration from 0.056 to 0.377 mol%, i.e., by a factor of 6.7 [144]. This resulted in a decrease of the T_g from 451 to 441 °C, a decrease of the temperature of the maximum nucleation rate from 468 to 452 °C, and the maximum nucleation rate increased by nearly one order of magnitude. The crystal growth velocities also increased by one order of magnitude.

Nevertheless, quite different effects may occur during crystal growth depending on the composition, especially if a melt of the target crystal composition would not form a glass upon cooling without additives. In these cases, the glass forming ability must be increased in order to enable a controlled glass crystallization, usually by increasing the relative concentration of network formers. If a crystal composed of network modifiers is precipitated, network formers are enriched at the growth front and increase the local viscosity, and hence the diffusivity of all glass components should decrease. Thus, the crystal growth velocity decreases with time, i.e., the effect is the opposite of that described for the water enrichment at the growth front. By contrast, if a crystalline phase enriched in network formers is precipitated, the viscosity should decrease and thus the diffusivities should increase, finally resulting in accelerated crystal growth.

In the 1990s, it was observed that alkaline earth fluoride nano crystals can be precipitated from some oxyfluoride glass compositions in a comparatively large volume concentration [535,536] while the glasses remain fully transparent [60,63,537]. These materials have a high application potential because rare earth ions can be incorporated in the nano crystals which gives rise to interesting luminescence properties [48,49,53–56,60,64,535–540]. This behaviour is caused by a self-organizing process: when F⁻ containing crystals grow in an oxyfluoride glass, F⁻ is removed from the melt which leads to an increase of the viscosity while the diffusivity of all components decreases [56,59,63,317], slowing down the growth velocity. A thermal treatment somewhat above the T_g of the oxyfluoride glass increases the viscosity to a value of 10^{13} dPas, i.e., the glass around each crystal has a T_g equal to the supplied temperature and crystal growth is no longer observed within the timescale of the performed experiments and the margin of error [56,59,63,317]. Hence, the crystals do not grow beyond a certain size. This is not only an effect of decreasing concentration gradients near the crystal, but predominantly an effect of decreasing diffusion coefficients in the SiO_2 rich layer around the crystals [56,57,59,317,427,511].

This is visualized in Fig. 23 a) for a glass with the composition $8.6 \text{Na}_2\text{O} \cdot 7.7 \text{K}_2\text{O} \cdot 10.6 \text{CaO} \cdot 12.5 \text{CaF}_2 \cdot 5.78 \text{Al}_2\text{O}_3 \cdot 54.8 \text{SiO}_2$ where the untreated glass has a T_g of 449 °C and the crystallization of CaF_2 increases the T_g to 552 °C after 80 h, i.e., slightly above the temperature supplied during thermal treatment at 550 °C. Prolonging the heat treatment did not result in a further increase of the T_g .

XRD patterns of these glass-ceramics are presented in Fig. 23 b) and show extremely broadened peaks indicating all CaF_2 crystals have mean sizes in the nm range. The mean crystallite size calculated from XRD line broadening [59,317] presented in Fig. 23 a) was constant within the margin of error after thermal treatments from 520 to 600 °C for times of 5 to 160 h. It should be noted that even increasing the crystallization temperature to 600 °C does not increase the mean crystal size in this system and the crystallized specimens were always fully transparent [59,317].

The formation of shells around growing crystal cores in glasses was first proven using a TEM equipped with an electron energy loss spectrometer (EELS) for the case of BaF_2 crystallization from an oxyfluoride glass [58] with a very narrow size distribution [541]. The core-shell structures around BaF_2 crystals were also proven using small angle X-ray scattering (SAXS) and ASAXS [542]. They were also detected around CaF_2 crystals [265].

Table 4 illustrates that the particle radius increases from 4.75 to 5.2 and 24.2 nm, if the crystallization temperature is increased

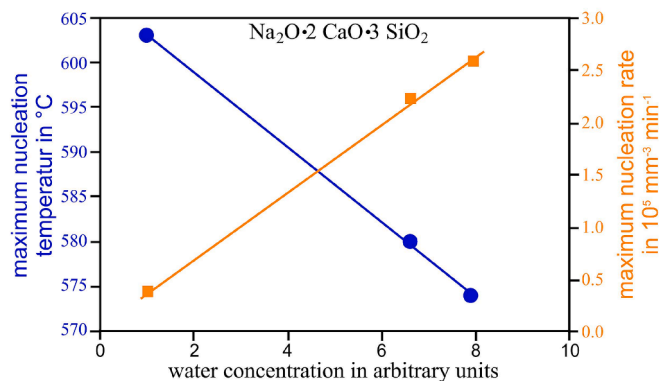


Fig. 22. Maximum nucleation rate and the temperature attributed to this maximum as a function of the water concentration in a glass with the composition $\text{Na}_2\text{O} \bullet 2 \text{CaO} \bullet 3 \text{SiO}_2$, based on data from Ref. [498].

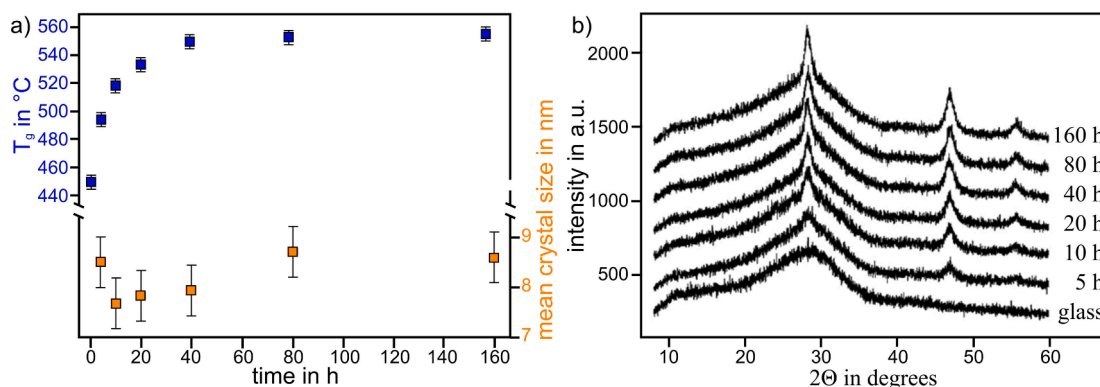


Fig. 23. Nanocrystallization of glasses with the composition $8.6 \text{ Na}_2\text{O} \cdot 7.7 \text{ K}_2\text{O} \cdot 10.6 \text{ CaO} \cdot 12.5 \text{ CaF}_2 \cdot 5.78 \text{ Al}_2\text{O}_3 \cdot 54.8 \text{ SiO}_2$. a) Mean crystal sizes calculated from the XRD-patterns in b) using the Scherrer equation as well as the T_g of the same glass crystallized for 5 to 160 h at 550 °C. b) XRD-patterns of these glass-ceramics after crystallization for 5 to 160 h at 550 °C. Based on Refs. [59] and [317].

Table 4

Particle radii and shell thicknesses assuming Gauss distributions fitted to SAXS and ASAXS curves for samples with the composition $69.6 \text{ SiO}_2 \cdot 7.5 \text{ Al}_2\text{O}_3 \cdot 15.0 \text{ K}_2\text{O} \cdot 1.9 \text{ Na}_2\text{O} \cdot 6 \text{ BaF}_2$ [542].

parameters	540 °C/20 h	600 °C/20 h	700 °C/2 h
particle radius in nm	4.75 ± 0.5	5.2 ± 0.5	24.2 ± 1.0
shell thickness in nm	2.35 ± 0.1	2.13 ± 0.1	1.82 ± 0.1

from 540 °C (20 h) to 600 °C (20 h) and 700 °C (2 h). It should be noted that 700 °C is above the T_g of the base glass without CaF_2 and is hence impossible to reach by removing F^- and Ca^{2+} from the glass so that the mechanism described above cannot freeze crystal growth at this temperature. The shell thickness decreases with increasing crystallization temperatures, probably due to a higher diffusivity of its components. Both the particle radii and the shell thicknesses are in agreement with the TEM observations, which showed the shell thickness to be about 2 nm [542].

Such core-shell structures were also found in LaF_3 glass-ceramics [511] and the $\text{KF}/\text{ZnF}_2/\text{SiO}_2$ system [56] where nano sized ZnF_2 or KZnF_3 precipitate. The crystallization of fluorides was accompanied by an increase of the viscosity in both cases. Precipitating transition metal fluorides has the advantage that they can be doped with other divalent transition metal ions, such as Ni^{2+} , which show a broad band emission in the near infrared range [64,538]. Table 5 summarizes the various glass systems from which fluoride nanocrystals were precipitated.

NaF can be crystallized from glasses in the $\text{Na}_2\text{O}/\text{K}_2\text{O}/\text{CaO}/\text{CaF}_2/\text{Al}_2\text{O}_3/\text{SiO}_2$ system which are usually doped with Ce^{3+} , Ag^+ , Sb^{3+} and/or Sn^{2+} [347–349,543]. Irradiating them with UV light leads to the crystallization of NaF which leads to a refractive index that is smaller in these regions than in the surrounding glass unaffected by crystallization. To the best of our knowledge, the precipitation of other alkali halides has not been reported in the literature. Other fluorides, such as alkaline earth or rare earth fluorides, have been intended to be crystallized in Na containing glasses, but NaF often crystallizes next to the desired phases or instead of them. In these cases, it may help to (partially) replace Na_2O by K_2O .

Table 4 shows that there are fairly numerous reports on the crystallization of alkaline earth fluorides. CaF_2 has been precipitated from oxyfluoride glasses without dopants [59,265,317,350] or with rare earth dopants such as Tm^{3+} [48], Er^{3+} [571] or Tb^{3+} [109] from glasses in the systems $\text{Na}_2\text{O}/\text{K}_2\text{O}/\text{CaO}/\text{Al}_2\text{O}_3/\text{CaF}_2/\text{SiO}_2$ or $\text{Na}_2\text{O}/\text{K}_2\text{O}/\text{CaO}/\text{ZnO}/\text{Al}_2\text{O}_3/\text{CaF}_2/\text{SiO}_2$. In analogy, a thermal treatment of $\text{Na}_2\text{O}/\text{K}_2\text{O}/\text{SrO}/\text{Al}_2\text{O}_3/\text{SrF}_2/\text{SiO}_2$ glasses enabled the precipitation of SrF_2 . The precipitation of BaF_2 from glasses in the $\text{Na}_2\text{O}/\text{K}_2\text{O}/\text{BaF}_2/\text{BaO}/\text{Al}_2\text{O}_3/\text{SiO}_2$ system has been reported [58,513,541,542] as well as that of Er^{3+} and Sm^{3+} doped BaF_2 [512]. BaLiF_3 was crystallized from $\text{LiF}/\text{BaF}_2/\text{Na}_2\text{O}/\text{Al}_2\text{O}_3/\text{B}_2\text{O}_3/\text{SiO}_2$ glasses [544] which should enable a simultaneous co-doping with divalent transition metal ions (at Li^+ sites) and rare earth cations at Ba^{2+} sites [544].

Nanocrystals containing rare earth metals as main components were even more frequently precipitated. Binary rare earth fluorides, in many cases doped with other rare earth ions, are to be especially mentioned because of their interesting luminescence properties. For example YF_3 doped with Eu^{3+} or Tb^{3+} was reported to crystallize from glasses of the $\text{NaF}/\text{YF}_3/\text{Al}_2\text{O}_3/\text{SiO}_2$ system [545,546], while LaF_3 [57,535,572] and ErF_3 [53] nanocrystals were respectively precipitated from glasses in the systems $\text{Na}_2\text{O}/\text{BaO}/\text{La}_2\text{O}_3/\text{AlF}_3/\text{Al}_2\text{O}_3/\text{SiO}_2$ or $\text{PbF}_2/\text{ErF}_3/\text{SiO}_2$. Glasses in the $\text{NaF}/\text{TbF}_3/\text{YbF}_3/\text{Al}_2\text{O}_3/\text{SiO}_2$ system were used to crystallize TbF_3 doped with YbF_3 [54], while YF_3 doped with YbF_3 was precipitated from the $\text{LiF}/\text{YbF}_3/\text{YF}_3/\text{Al}_2\text{O}_3/\text{SiO}_2$ system [547]. Thermal treatments of glasses in the MF_2 base system ($\text{M}=\text{Ca}, \text{Sr}, \text{Ba}$)/ $\text{GdF}_3/\text{Al}_2\text{O}_3/\text{SiO}_2$ resulted in the precipitation of GdF_3 doped with Yb^{3+} or Er^{3+} [548]. Another case is the precipitation of solid solutions containing Pb from glasses with the base composition $\text{PbO}/\text{CdO}/\text{PbF}_2/\text{CdF}_2/\text{YbF}_3/\text{B}_2\text{O}_3/\text{Al}_2\text{O}_3/\text{SiO}_2$ [539,549,550] or $\text{MgF}_2/\text{CaF}_2/\text{BaF}_2/\text{YbF}_3/\text{ErF}_3/\text{PbF}_2/\text{AlF}_3$ [536], where $(\text{Pb}, \text{Yb})\text{F}_x$ doped with Er^{3+} or Yb^{3+} were respectively crystallized.

The crystallization of ternary fluorides containing both alkali and rare earth ions as well as of fluorides containing both alkaline

Table 5
Nano crystalline fluoride crystals precipitated from various oxyfluoride glasses.

Chemical Composition	Phase	Dopant	Reference
Alkalifluorides			
Na ₂ O/K ₂ O/CaO/CaF ₂ /Al ₂ O ₃ /SiO ₂	NaF		[347-349,543]
Alkaline Earth Fluorides			
Na ₂ O/K ₂ O/CaO/Al ₂ O ₃ /CaF ₂ /SiO ₂	CaF ₂	-	[59,265,317]
Na ₂ O/K ₂ O/CaO/ZnO/Al ₂ O ₃ /CaF ₂ /SiO ₂	CaF ₂	-	[350]
Na ₂ O/K ₂ O/CaO/Al ₂ O ₃ /CaF ₂ /SiO ₂	CaF ₂	Tm	[48]
Na ₂ O/K ₂ O/CaO/Al ₂ O ₃ /CaF ₂ /SiO ₂	CaF ₂	Er	[444]
Na ₂ O/K ₂ O/CaO/Al ₂ O ₃ /CaF ₂ /SiO ₂	CaF ₂	Tb	[109]
Na ₂ O/K ₂ O/SrO/Al ₂ O ₃ /SrF ₂ /SiO ₂	SrF ₂		[496,521]
Na ₂ O/K ₂ O/BaF ₂ /BaO/Al ₂ O ₃ /SiO ₂	BaF ₂		[58,63,513,541,542]
Na ₂ O/K ₂ O/BaF ₂ /BaO/Al ₂ O ₃ /SiO ₂	BaF ₂	Er, Sm	[512]
LiF/BaF ₂ /Na ₂ O/Al ₂ O ₃ /B ₂ O ₃ /SiO ₂	LiBaF ₃		[544]
Rare Earth Fluorides			
NaF/YF ₃ /Al ₂ O ₃ /SiO ₂	YF ₃	Eu, Tb	[545,546]
LiF/YbF ₃ /YF ₃ /Al ₂ O ₃ /SiO ₂	YF ₃	Yb	[547]
Na ₂ O/BaO/La ₂ O ₃ /AlF ₃ /Al ₂ O ₃ /SiO ₂	LaF ₃		[57,60,535]
MF ₂ (M=Ca, Sr, Ba)/GdF ₃ /Al ₂ O ₃ /SiO ₂	GdF ₃	Yb, Er	[548]
PbF ₂ /ErF ₃ /SiO ₂ /	ErF ₃		[53]
NaF/TbF ₃ /YbF ₃ /Al ₂ O ₃ /SiO ₂	TbF ₃	Yb	[54]
PbO/CdO/PbF ₂ /CdF ₂ /YbF ₃ /B ₂ O ₃ /Al ₂ O ₃ /SiO ₂	(Pb,Yb)F _x	Er	[539,549,550]
MgF ₂ /CaF ₂ /BaF ₂ /YbF ₃ /ErF ₃ /PbF ₂ /AlF ₃	(Pb,Cd)F _x	Er+Yb	[536]
Transition Metal Fluorides			
KF/ZnF ₂ /SiO ₂	ZnF ₂		[56]
KF/ZnF ₂ /SiO ₂	KZnF ₃		[56,64,538]
Complex Rare Earth Fluorides			
LiF/GdF ₃ /Al ₂ O ₃ /SiO ₂	LiGdF ₄	Pr, Sm, Dy	[551]
Na ₂ O/NaF/Gd ₂ O ₃ /AlF ₃ /Al ₂ O ₃ /SiO ₂	NaGdF ₄	Sm	[49,540]
Li ₂ O/LiF/YF ₃ /Al ₂ O ₃ /SiO ₂	LiYF ₄		[552]
Na ₂ O/NaF/AlF ₃ /Al ₂ O ₃ /SiO ₂	NaLuF ₄	Tm,Tm+Yb	[553]
Na ₂ O/NaF/AlF ₃ /Al ₂ O ₃ /SiO ₂	NaLuF ₄	Yb, Er, Tm	[554]
Na ₂ O/CaO/NaF/LuF ₃ /Al ₂ O ₃ /SiO ₂	NaLuF ₄	Yb, Tb	[555]
Na ₂ O/NaF/YF ₃ /Al ₂ O ₃ /SiO ₂	NaYF ₄	Er, Yb	[556,557]
Na ₂ O/NaF/CaO/YF ₃ /Al ₂ O ₃ /SiO ₂	Na _{1.5} Y _{2.5} F ₉	Tb, Ce	[558]
Na ₂ O/NaF/YF ₃ /B ₂ O ₃ /SiO ₂	Na ₅ Y ₉ F ₃₂	Dy, Ce	[559]
Na ₂ O/NaF/YF ₃ /B ₂ O ₃ /SiO ₂	NaYbF ₄	Er, Ho, Dy	[560]
Na ₂ O/LaF ₃ /Al ₂ O ₃ /SiO ₂	NaLaF ₄		[61]
K ₂ O/ La ₂ O ₃ /LaF ₃ /Al ₂ O ₃ /SiO ₂	KLaF ₄	-	[62]
Na ₂ O/BaF ₂ /Gd ₂ O ₃ /Al ₂ O ₃ /SiO ₂	BaGdF ₅	Tb	[561]
Na ₂ O/BaF ₂ /GdF ₃ /B ₂ O ₃ /SiO ₂	BaGdF ₅	Eu	[562]
Na ₂ O/BaF ₂ /GdF ₃ /B ₂ O ₃ /SiO ₂	BaGdF ₅	Er, Yb	[562]
Na ₂ O/CaO/BaF ₂ /LuF ₃ /B ₂ O ₃ /SiO ₂	BaLuF ₅	Eu	[563]
BaF ₂ /YF ₃ /YbF ₃ /Al ₂ O ₃ /SiO ₂	Ba ₄ Y ₃ F ₁₇	Er	[564]
Complex Alkali Lead Halogenides			
Cs ₂ O/SrO/NaBr/PbBr ₂ /Al ₂ O ₃ /P ₂ O ₅ /SiO ₂	CsPbBr ₃	-	[565,566]
Na ₂ O/Cs ₂ O/ZnO/PbBr ₂ /NaBr/B ₂ O ₃ /SiO ₂	CsPbBr ₃	Dy	[567]
Cs ₂ O/ZnO/PbBr ₂ /NaBr/B ₂ O ₃ /SiO ₂	CsPbBr ₃	Tb, Eu	[568]
Na ₂ O/Cs ₂ O/ZnO/PbBr ₂ /KBr/Al ₂ O ₃ /B ₂ O ₃ /TeO ₂	CsPbBr ₃	-	[569]
Cs ₂ O/SrO/ZnO/PbI ₂ /NaI/B ₂ O ₃ /SiO ₂	CsPbI ₃	-	[570]

earth and rare earth ions has also been frequently reported in the literature. Most of the fluoride crystals were doped with other rare earth elements. Table 4 shows that LiGdF₄ [551] as well as NaGdF₄ [49,540], NaLuF₄ [553-556] doped with various rare earth cations, LiYF₄ [552], NaYF₄ [556,557], Na_{1.5}Y_{2.5}F₉ [558], Na₅Y₉F₃₂ [559], KLaF₄ [62], NaYbF₄, doped with Er³⁺, Ho³⁺ and Dy³⁺ [560], and NaLaF₄ [61] nano crystals were precipitated from alkaline rare earth aluminosilicate glasses. Concerning alkaline earth rare earth fluorides, BaGdF₅ [561,562] also doped with other rare earth elements were most frequently reported. BaLuF₅ and Ba₄Y₃F₁₇ both doped with Er³⁺ have also been crystallized [564,564]. Glass-ceramics containing rare earth doped nano crystalline fluorides can, e.g., be used as active laser materials, up-conversion materials and materials for quantum cutting; Table 5 illustrates that there is much literature in this field which has been reviewed as well [497,547,573-577].

The crystallization of other halogenides from glass melts was scarcely reported before 2016 when the crystallization of CsPbBr₃ from a phosphate glass of the composition Cs₂O/SrO/NaBr/PbBr₂/Al₂O₃/P₂O₅/SiO₂ was first described [565,566]. CsPbBr₃ was then crystallized from borosilicate glasses in the systems Cs₂O/ZnO/PbBr₂/NaBr/B₂O₃/SiO₂ [568] and Na₂O/Cs₂O/ZnO/PbBr₂/NaBr/B₂O₃/SiO₂ [567] as well as from tellurite glasses in the Na₂O/Cs₂O/ZnO/PbBr₂/KBr/Al₂O₃/B₂O₃/TeO₂ system [569]. The crystallization of CsPbI₃ from glasses in the system Cs₂O/SrO/ZnO/PbI₂/NaI/B₂O₃/SiO₂ was also described [570]. These materials were also doped with a large variety of rare earth elements and exhibit very interesting luminescence properties, the number of publications on this topic is currently increasing rapidly. It should be noted that Ag and Cu chlorides, bromides and iodides precipitated from glasses in tiny quantities have been known for a long time and are the basis of photochromic glasses [253-255] which show reversible

photodarkening.

Details concerning the physical properties of transparent nano crystalline transparent glass-ceramics based on halides and their optical properties were recently described in comprehensive reviews [497,573]. Other cases where the precipitation of nano crystals is accompanied by a viscosity increase are not as easy to understand as for the halogenide crystallization. One example is the crystallization of quartz solid solution in the $\text{MgO}/\text{Al}_2\text{O}_3/\text{SiO}_2/\text{TiO}_2$ system [427]. Here the T_g increase is even more pronounced and shifts from 812 °C to around 960 °C during thermal treatment at 960 °C, i.e., to the supplied temperature. Crystallization begins with the precipitation of a nucleation agent such as ZrO_2 [389,390] followed by the crystallization of a quartz solid solution incorporating equimolar concentrations of MgO and Al_2O_3 (around 10 mol% each). Then the quartz crystals expel MgO and Al_2O_3 which form spinel ($\text{Mg}_2\text{Al}_2\text{O}_4$) [389,390] and are hence depleted in these components. The spinel crystals grow, also depleting Mg^{2+} and Al^{3+} from the glass melt and causing an increase of the residual glass viscosity [427]. The residual quartz contains only minor MgO and Al_2O_3 concentrations (~ 1 mol% each) and transfers to α -quartz during cooling [89], as shown using dilatometry [89]. It was concluded that the attributed high temperature phase is β -quartz.

Further examples are found in the $\text{Na}_2\text{O}/\text{CaO}/\text{Fe}_2\text{O}_3/\text{B}_2\text{O}_3$ system where nano crystalline magnetite precipitates after adjusting the redox $\text{Fe}^{2+}/\text{Fe}^{3+}$ ratio during thermal treatment and the T_g increases from 520 to 585 °C [578].

A deductible general rule to achieve nano crystallization is to design glass compositions so that network forming components are enriched in the residual glass during crystallization. While this strategy is easy enough for fluorides, where the viscosity always increases during crystallization (at least in silicate glasses), it is more complicated for the crystallization of oxides or silicates because here judging how the viscosity will change is often much harder. It is particularly difficult if a glass contains B_2O_3 or Al_2O_3 because the coordination number of B and Al ions in the glass may change during crystallization; Boron may change from four to threefold while Al may change from four to five- and sixfold or vice versa. As a first approximation, it may help to design a crystallization path where the composition of the residual glass is calculated for different volume concentrations of the crystal phase. Then, the viscosity at appropriate temperatures (above T_g) should be calculated for the respective compositions of the residual glass using empirical correlations and/or appropriate software such as, e.g., Sciglass [579]. If the viscosity of the residual glass melt increases or is higher than that of the initial glass at some point of crystallization, the composition should be favourable to achieve nano crystallization. A relatively simple experiment to perform is crystallizing a glass and measuring whether the T_g increases. If so, nano crystallization probably occurred if the correct crystal phase is formed while the specimen remains transparent.

Fig. 24 presents direct evidence using combined TEM and EDXS for the example of a glass with the molar composition $70 \text{ SiO}_2 \bullet 7 \text{ Al}_2\text{O}_3 \bullet 8 \text{ Na}_2\text{O} \bullet 8 \text{ K}_2\text{O} \bullet 7 \text{ LaF}_3$ from which NaLaF_4 was crystallized. The normalized concentration of Si declines rapidly with an increasing distance from the crystal [61]. It should be noted that the shells around crystal cores simply function as diffusion barriers and may also play an important part if nucleating agents crystallize. This has also been shown for the diffusion profile around a ZrTiO_4 crystal [402]. Here, the Al/Si ratio declines rapidly with an increasing distance from the crystal. Another example is the precipitation of metallic Ag nano crystals [571] where Ag^+ is removed from the melt by a preceding redox reaction (e.g., $2\text{Ag}^+ + \text{Sb}^{3+} \rightarrow 2\text{Ag} + \text{Sb}^{5+}$) which leads to an increase in viscosity because Ag^+ acts as a network modifier [580] and is removed from the adjacent glass melt, thus forming a diffusion barrier which hinders further growth.

Fig. 25 illustrates the effects glass compounds not incorporated into crystals have on crystal growth. If a network modifier is crystallized, network forming compounds are enriched at the growth front, increasing the viscosity and decreasing the crystal growth velocity, sometimes by some orders of magnitude. In turn, the crystal growth velocity increases when network formers crystallize as network modifiers are enriched at the growth front and the viscosity decreases. The latter is quantitatively described above for the case of water.

3.6. The Formation of Internal Stresses and their Effects

Internal stresses have an important effect on the mechanical properties of glass-ceramics. As most contain significant amounts of at

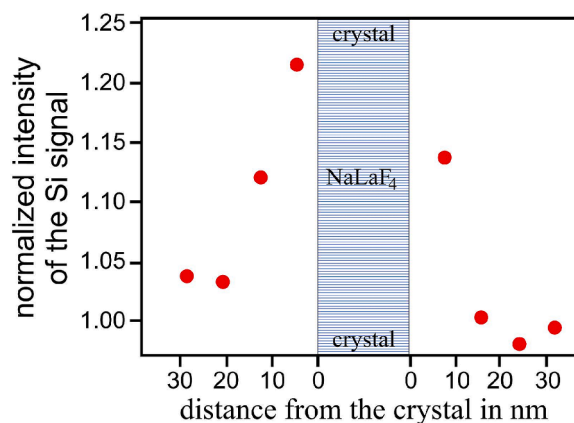


Fig. 24. Diffusion profile around a NaLaF_4 crystal in a $70 \text{ SiO}_2 \bullet 7 \text{ Al}_2\text{O}_3 \bullet 8 \text{ Na}_2\text{O} \bullet 8 \text{ K}_2\text{O} \bullet 7 \text{ LaF}_3$ melt. Based on Ref. [61].

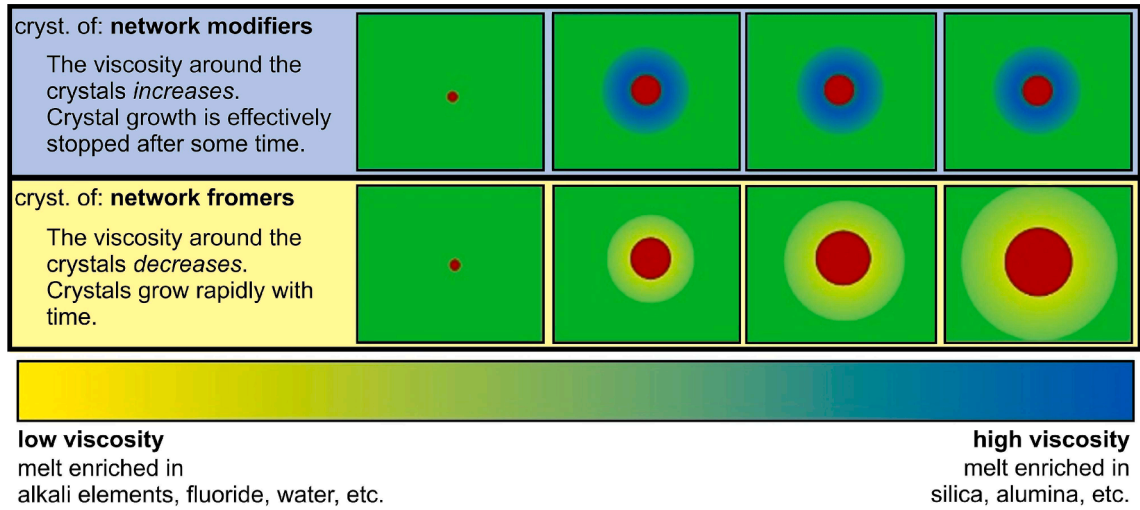


Fig. 25. The effect that compounds enriched at the growth front have on the crystal growth velocity.

least one crystalline and one glassy phase, stresses form during cooling because the respective CTEs almost never match. In a first approximation, the stresses form below the T_g but the cooling rate has a minor effect: smaller cooling rates allow mechanical relaxation which decreases T_g (see the Bartenew Equation in Ref. [581]) and hence the glass is frozen at a lower temperature. The calculation of stresses from the CTEs, the elastic moduli, Poisson ratios and the T_g is currently only possible for very simple geometries such as spherical or ellipsoidal inclusions in an infinitely large matrix, see, e.g., Selsing [582]. As real materials are mainly not composed by inclusions in an infinitely large matrix, Eq. (20) for spherical inclusions (index: i) in a matrix (index: m) is only a first approximation. Nevertheless, the formed stresses can be estimated. For a temperature of 25 °C this means:

$$P = \frac{\Delta CTE \times (T_g - 25^\circ C)}{\left(\frac{1+\mu_m}{2E_m} + \frac{1-2\mu_i}{E_i} \right)} \quad (20)$$

Where E_i and E_m are the Young's Moduli, and μ_i and μ_m are the respective Poisson's ratios of the inclusion and the matrix. ΔCTE is the difference in the linear CTEs of matrix and inclusion, T_g is in °C and P is the stress inside the spherical inclusion. Equation (20) is only valid if the CTE does not depend on the crystallographic direction, i.e., for isotropic spherical inclusions and matrices. The stresses formed at the matrix/inclusion interface do not depend on the size of the inclusion. If the inclusions are far enough from each other, the stress inside an inclusion is distributed homogeneously. In the matrix, the radial (σ_r) and tangential stress (σ_t) decline with R^3/d^3 (with R = radius of the inclusion and d = distance from the centre of the particle) as described by Eq. (21):

$$\sigma_r = -2\sigma_t = -P \frac{R^3}{d^3} \quad (21)$$

Hence, the stresses at a given distance from the inclusion increase with an increasing size of the inclusion. Please note that the signs for the radial and tangential stresses always oppose each other. Finite element calculations are possible for more complicated systems composed of a few crystals arbitrarily arranged to each other or inclusions with different CTEs in different crystallographic directions

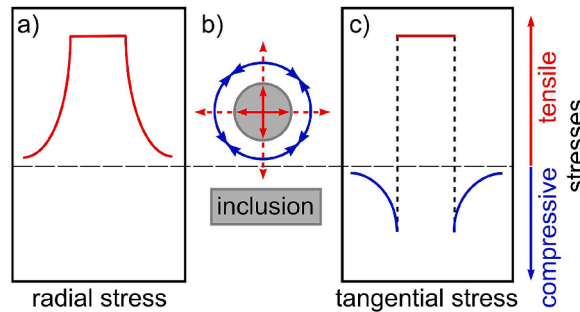


Fig. 26. Stresses around spherical inclusions a) in radial direction: tensile stresses in and around an inclusion with a higher CTE than the matrix. b) Direction of tensile stresses and compressive stresses in and outside the inclusion. c) Tangential directions: tensile stress in the inclusion and compressive stresses outside the inclusion according to Ref. [582], see Eq. (21).

and may provide an idea how real microstructures may behave.

Fig. 26 shows a scheme of the stresses formed in and around a spherical inclusion for the case that the CTE of the inclusion is larger than that of the bulk and does not depend on the crystallographic direction. As outlined in Fig. 26 a), isostatic tensile stresses occur inside the inclusion while the radial stresses outside are also tensile. By contrast, the tangential stresses are compressive and only 50 % of the radial stresses at a given distance from the particle as illustrated in Fig. 26 c). Of course, a prerequisite of such considerations is that the matrix/inclusion interface is strong enough not to fracture.

Ref. [583] describes stresses calculated in and around two spherical inclusions using the finite element method. The calculated stresses are in a fairly good agreement with those obtained by a simple superposition of (radial) stress profiles calculated for spheres in an infinitely large matrix according to Eq. (21). Fig. 27 visualizes the stresses amongst the matrix and two spherical inclusions of the same size at distances of a) $3 \cdot R$ (radius of the inclusion) and b) $1 \cdot R$. The stresses inside the inclusions show little asymmetry at larger distances a) but if the distance is R , they are no longer isostatic and increase at that side which faces the second sphere. The stresses in the matrix are notably higher between the spheres than at the opposite side.

An even greater impact on stress formation is caused by crystal phase transitions below the T_g of the residual glass as the accompanying volume effect can be much higher than that of the CTE mismatch. Equation (22) can be used for the case of a spherical inclusion undergoing a phase transition. The numerator of this equation stands for changes in the dimension.

$$P = \frac{\Delta V^*/3}{\left(\frac{1+\mu_m}{2E_m} + \frac{1-2\mu_l}{E_l}\right)} = \frac{\Delta CTE_2 \times (T_g - T_t) + \Delta V_t/3 + \Delta CTE_1(T_t - 25^\circ \text{C})}{\left(\frac{1+\mu_m}{2E_m} + \frac{1-2\mu_l}{E_l}\right)} \quad (22)$$

The phase transition takes place at the temperature T_t and usually runs parallel to a volume decrease (ΔV_t) during cooling. The total volume change between the two phases, ΔV^* depends on (i) ΔV_t and (ii) the change in length during cooling from T_g to T_t as well as on (iii) the change in length during cooling from T_t to 25°C . It is assumed that the matrix CTE remains constant over the entire temperature range and that the CTE of the low temperature phase is smaller, but also constant between 25°C and T_t (according ΔCTE_1). The CTE of the high temperature phase is also assumed to be constant between T_t and T_g (according ΔCTE_2). The elastic constants of the inclusion and the matrix phase are assumed to remain constant between 25°C and T_t . The contribution of the three terms of Eq. (22) is illustrated in Fig. 28.

3.6.0.1. Mismatch in the Coefficients of Thermal Expansion

The case of a surface crystallizing glass is considered as a first example. After surface nucleation with a high nucleation rate, the crystals grow into the bulk and ideally form a layer with an approximately constant thickness which can be adjusted by the time and temperature of thermal treatment. At temperatures above T_g , the viscoelastic properties of the glass melt allow stresses to relax during cooling, but below T_g the relaxation times become too large for effective relaxation. It is a good approximation to assume that T_g is the temperature below which mechanical stresses are frozen although it can actually vary depending on the cooling rate upon which the T_g depends according to the Bartenev Equation [581,584]. If the CTE of a surface crystallized layer is smaller than that of the glass,

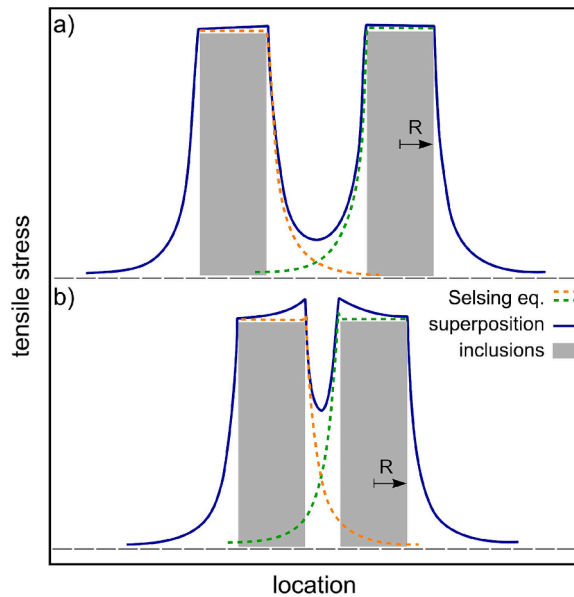


Fig. 27. Tensile stresses (dashed lines) between two spherical particles with different distances in a matrix with smaller CTE. a) Distance between the spheres = $3 \cdot R$ (radius of the spheres). b) Distance between the spheres = R . The solid line represents the sum of the stresses in the particle vicinity according to a superposition of the dashed lines (Eq. (21) and Ref. [582]).

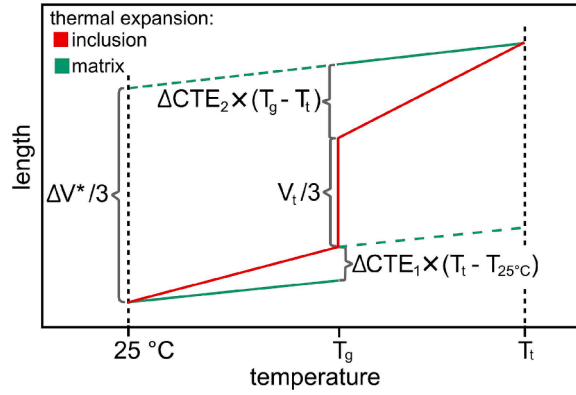


Fig. 28. The length changes of matrix and inclusion as a function of the temperature during cooling if there is a phase transition according to Eq. (22).

compressive stresses form near the surface during cooling. These stresses are high if T_g is high and the differences in the CTEs of the crystalline layer and the bulk glass are large. According to Ref. [585], the stresses at the bulk/layer boundary are given by Eq. (23):

$$\sigma = \frac{\Delta CTE \times E_1 \times E_2 \times (T_g - 25^\circ \text{C})}{E_1 + E_2} \quad (23)$$

where E_1 and E_2 are the respective Young's Moduli of the surface layer and the bulk. The stresses at the immediate surface decrease with an increasing thickness of the crystallized layer [586] and the CTE parallel to the surface is decisive for anisotropic crystalline phases because crystallized surface layers are often crystallographically textured. Hence the crystallization of a thin surface layer with the relevant CTE lower than that of the glass leads to compressive stresses at the surface which should result in an increase of the mechanical strength. This route to improve the mechanical properties of glass-ceramics has been scarcely reported in the scientific literature [586-589] but the patent literature is quite comprehensive, see the Refs. [590-593]. One of the few reports in the scientific literature is the crystallization of β -quartz (formal composition: LiAlSiO_4) from a glass with the composition $66 \text{ SiO}_2 \cdot 20.7 \text{ Al}_2\text{O}_3 \cdot 6.1 \text{ Li}_2\text{O} \cdot 2.9 \text{ K}_2\text{O} \cdot 1.2 \text{ Na}_2\text{O} \cdot 1.1 \text{ MgO} \cdot 1.1 \text{ CaO}$ which was already published in 1996 [589] where the obtained 4-point-bending strengths were up to 800 MPa for a 100 μm thick crystalline surface layer.

A more recent report performed using the same glass composition achieved a ball-on-three-ball strength of 680 MPa for these transparent glass-ceramics [594], the results are presented in Fig. 29. The strength increases from about 100 MPa for the glass up to 680 MPa for a glass-ceramic with a 9 μm thick layer of surface crystallization [594]. LiAlSiO_4 has a negative thermal expansion and, if the composition contains nucleating agents such as ZrO_2 and/or TiO_2 , a thermal treatment leads to bulk crystallization and enables to prepare zero thermal expansion glass-ceramics. By contrast, compositions without nucleating agents may solely show surface crystallization. It should be noted that this composition does not contain any nucleation agent and does not crystallize in the bulk. This procedure is hence not suitable to prepare zero thermal expansion glass-ceramics with a high strength. In analogy, glass with the composition Zn_2SiO_4 shows the sole surface crystallization of willemite [586] and has a CTE of $2.3 \cdot 10^{-6} \text{ K}^{-1}$ perpendicular to the crystallographic c-axis which is the dominant growth direction. This is notably lower than the CTE of $5.5 \cdot 10^{-6} \text{ K}^{-1}$ in the glass. The

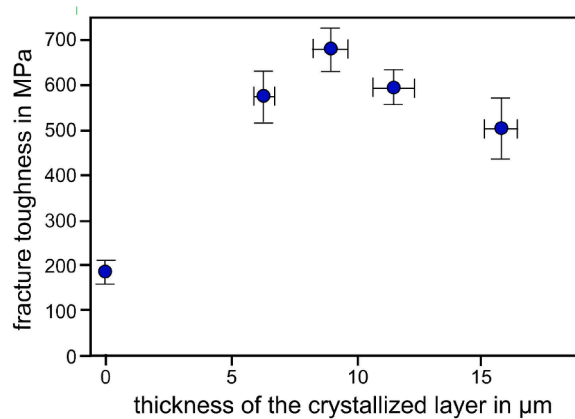


Fig. 29. Mechanical strength (ball on three ball test) of a glass-ceramic with the composition $66 \text{ SiO}_2 \cdot 20.7 \text{ Al}_2\text{O}_3 \cdot 6.1 \text{ Li}_2\text{O} \cdot 2.9 \text{ K}_2\text{O} \cdot 1.2 \text{ Na}_2\text{O} \cdot 1.1 \text{ MgO} \cdot 1.1 \text{ CaO}$ surface crystallized at 565°C for various periods of time. Based on Ref. [594].

strength increases rapidly with the crystallization time to reach a maximum after 10 h before decreasing again. The maximum value of 218 MPa is about three times the value of the uncrystallized glass and corresponds to a surface layer thickness of 33 μm which is comparable to the layer with compressive stresses of commercial glasses reinforced by ion exchange [595,596]. It should be noted that the latter have high bending strengths of up to 800 MPa for soda-aluminosilicate glasses ion exchanged with potassium salt melts [597-599].

The more important issue are systems showing bulk crystallization where the CTE of the crystallizing phase is larger than that of the residual glass. They were by far more frequently studied because this usually leads to an increase of the mechanical strength. To the best of our knowledge, the first report on the effect of crystalline inclusions in a glassy matrix on the mechanical strength was published by F. F. Lange in 1971 [600]. Here Al_2O_3 particles were homogeneously dispersed in a borosilicate glass powder and subsequently sintered under pressure causing an increase of the mechanical strength. The CTE of $\alpha\text{-Al}_2\text{O}_3$ parallel to the crystallographic c-axis is $8.3 \cdot 10^{-6} \text{ K}^{-1}$ while that perpendicular to the c-axis is $7.2 \cdot 10^{-6} \text{ K}^{-1}$ [601], meaning the average CTE should be $7.5 \cdot 10^{-6} \text{ K}^{-1}$. The CTE of the used borosilicate glass should be $7.9 \cdot 10^{-6} \text{ K}^{-1}$ according to SciGlass [579]. The mismatch in the CTEs is hence small and stresses generated during cooling should hence also be small. Nevertheless, compressive stresses should occur inside the inclusions.

It has been shown that the mechanical strength of phase separated glasses is often smaller than that of homogeneous glasses [602]. In the past, this has been related to the inhomogeneity of these glasses in which droplets or the interface between the droplet and the matrix may act as Griffith flaws [603]. This was mainly stated for glasses in the $\text{Na}_2\text{O}/\text{B}_2\text{O}_3/\text{SiO}_2$ system which showed phase separations into SiO_2 rich droplets and an $\text{Na}_2\text{O}/\text{B}_2\text{O}_3$ -rich matrix. It should be noted that the inclusions in these glasses have a smaller CTE than their matrix [480,602]. Recent studies have reported that glasses with the inverted separation into $\text{Na}_2\text{O}/\text{B}_2\text{O}_3$ enriched droplets and an SiO_2 -rich matrix in turn show higher mechanical strengths than the homogeneous glass [467], disproving that phase separation should automatically be considered to be a flaw.

This is supported by the fact that crystalline inclusions with a higher CTE than the matrix generally cause higher mechanical strengths [480,602]. Here radial compressive stresses occur around the inclusion according to the Eqs. (20) and (21) while the corresponding axial stresses are tensile. The stresses in phase separated glasses notably depend on the temperature/time schedule applied during the phase separation process because the chemical composition of both phases, and hence also their CTEs, depend on it [467].

Crystalline phases with a high CTE that can be precipitated from glasses are, e.g., ZrO_2 (CTE $\sim (10\text{--}11) \cdot 10^{-6} \text{ K}^{-1}$ [604], MgAl_2O_4 (CTE $\sim 9 \cdot 10^{-6} \text{ K}^{-1}$ [605]), $\text{Ba}_x\text{Si}_2\text{O}_{4+x}$ (with $1 \leq x \leq 2$, CTEs $\sim (10\text{--}13) \cdot 10^{-6} \text{ K}^{-1}$) [457] or phases within the solid solution systems $\text{Ba}(\text{Zn}, \text{M})_2\text{Si}_2\text{O}_7$ (M=Mg, Mn, Ni, Co, Cu) with CTEs ranging from 12 to $16 \cdot 10^{-6} \text{ K}^{-1}$ [84,606]. One example of such glass-ceramics is the system $\text{MgO}/\text{Y}_2\text{O}_3/\text{Al}_2\text{O}_3/\text{SiO}_2/\text{ZrO}_2$ with 2.4 mol% Y_2O_3 [379]. Here tetragonal ZrO_2 and spinel form during crystallization while α - or β -quartz phases are not formed and 4-point bending strengths up to 440 MPa were reported [379].

Rare earth or alkaline earth fluorides show even higher CTEs frequently above $20 \cdot 10^{-6} \text{ K}^{-1}$ [607]. Hence the precipitation of fluorides would seem to be particularly promising to achieve high mechanical strengths, but favourable mechanical properties have not been reported for such glass-ceramics so far. Perhaps this is caused by an incompatibility of the fluoride crystals with the silicate network, which does not lead to a strong adherence between such inclusions and their matrix. Otherwise, the crystallization of fluorides results in the formation of a shell highly enriched in SiO_2 around the fluoride crystals as discussed in chapter 3.5 which should have a lower CTE than the bulk glass and may play a decisive part in stress formation.

3.6.0.2. Phase Transitions during Cooling

The described above, the effect of inclusions with high CTEs can be enhanced by precipitating phases which show a phase transition in the temperature range from somewhat below T_g to room temperature (RT) during cooling and is accompanied by a volume decrease. Then the effect of the volume contraction is much larger than of phases which solely show a linear shrinkage with decreasing temperature. Phases crystallized from glasses showing a pronounced volume decrease in the respective temperature range are, e.g., cristobalite ($T_f=180\text{--}270^\circ\text{C}$, $\Delta V=2.8\%$ [608]), quartz ($T_f=573^\circ\text{C}$, $\Delta V=0.8\%$ [608]) or $\text{BaZn}_2\text{Si}_2\text{O}_7$ ($T_f=260\text{--}280^\circ\text{C}$, $\Delta V=3.5\%$ [84]). While the T_f is nearly constant for cristobalite, it is somewhat affected by the formation of a solid solution in quartz (typically: 1 mol% MgO and 1 mol% Al_2O_3). Quartz solid solutions with much higher MgO and Al_2O_3 concentrations do not show a transformation and hence the same phase occurs at high temperature and at RT [89]. Hence the formation of quartz solid solutions incorporating higher concentrations of MgO and Al_2O_3 should be avoided if high stresses are desired. The T_f of $\text{BaZn}_2\text{Si}_2\text{O}_7$ is widely affected by the formation of solid solutions and values from below RT up to 950°C have been reported [84,90,91]. The CTEs in this system, and their dependence on the crystallographic direction, are strongly affected by the formation of solid solutions [84,90,91].

The most frequently published system showing a phase transition during cooling is $\text{MgO}/\text{Al}_2\text{O}_3/\text{SiO}_2$ [41,47,89,352,378,379,389,390,418,427] which can be modified by the (partial) replacement of MgO against ZnO [46,421]. Nucleation agents such as TiO_2 , ZrO_2 or both are absolutely necessary to achieve volume nucleation as most compositions otherwise solely show surface crystallization [160,609-612]. As noted above, the nucleation agent is crystallized in a first step and hence, e.g., TiO_2 , ZrO_2 or ZrTiO_4 are formed. Then, a quartz solid solution is precipitated which typically contains 10 mol% of both Al_2O_3 and MgO (MgO may partially be replaced by ZnO). During further thermal treatment, the quartz solid solution expels MgO and Al_2O_3 to form spinel, MgAl_2O_4 or $(\text{Mg}, \text{Zn})\text{Al}_2\text{O}_4$ and a quartz solid solution with only minor MgO and Al_2O_3 concentrations, the latter transforms to an α -quartz solid solution during cooling. This decomposition is accelerated by increasing temperatures and an increasing concentration of nucleating agents. The α -quartz phase has a high CTE and typical MgO and Al_2O_3 concentrations of 1 mol% each. In the range of $100\text{--}300^\circ\text{C}$, the mean CTE is around $10\text{--}12 \cdot 10^{-6} \text{ K}^{-1}$ and decreases to $5\text{--}6 \cdot 10^{-6} \text{ K}^{-1}$ between 550 and 800°C [89]. The phase transition appears as a kink in the dilatometric curve rather than a step [89]. The CTE of the residual glass is about $4\text{--}5 \cdot 10^{-6} \text{ K}^{-1}$. Nevertheless, the CTE of the crystalline inclusion is much higher than that of the surrounding matrix and hence, the inclusion is under tensile stress while the radial stresses around the inclusion are also tensile stresses, but the tangential stresses are compressive. Hence

the stresses around the crystalline α -quartz inclusions are qualitatively comparable with those around the $\text{Na}_2\text{O}/\text{B}_2\text{O}_3$ droplets in phase separated glasses. The strengths achievable by utilizing this effect may exceed 1 GPa in the $\text{MgO}/\text{Al}_2\text{O}_3/\text{SiO}_2$ and $\text{MgO}/\text{ZnO}/\text{Al}_2\text{O}_3/\text{SiO}_2$ systems [46,47].

It should be noted that quartz solid solutions with high MgO and Al_2O_3 concentrations (i.e., that phase which is formed before spinel is expelled) have a comparatively small CTE of about $4.5\text{--}5.0 \cdot 10^{-6} \text{ K}^{-1}$ [89], hence approximately have the same CTE as the surrounding matrix and thus do not give rise to high strengths. Besides keatite, this β -quartz solid solution is the main crystalline phase in glass-ceramics based on lithium aluminosilicate, which frequently shows CTEs around zero [30]. Here, Al_2O_3 and mainly Li_2O are incorporated into the solid solution besides MgO and ZnO which leads to a stabilization of the β -quartz and a negative thermal expansion of the crystalline phase. As the strengthening mechanism does not work if the CTE of the inclusion is lower than that of its matrix, the mechanical strengths of low CTE glass-ceramics are much lower than for glass-ceramics in the $\text{MgO}/\text{Al}_2\text{O}_3/\text{SiO}_2$ system optimized with respect to high mechanical strengths. This is most evident for cases where the glass-ceramic microstructures containing inclusions of high and much lower CTEs are similar. For example, if a glass in the system $\text{MgO}/\text{Al}_2\text{O}_3/\text{SiO}_2$ is crystallized at 1050°C , the subsequent thermal expansion is low, approximately constant up to 1000°C , a quartz solid solution with 10 mol% MgO and Al_2O_3 each is formed and the indentation fracture toughness is $2.1 \text{ MPa}\cdot\text{m}^{1/2}$. If the same glass is crystallized at 1080°C , the subsequent thermal expansion is much higher up to a temperature of around 520°C , a quartz solid solution with only minor concentrations of MgO and Al_2O_3 occurs and the indentation fracture toughness is more than doubled to $4.3 \text{ MPa}\cdot\text{m}^{1/2}$ [89] while the microstructures are almost the same.

3.7. Solid Solutions with Variable Compositions and Properties

Many phases precipitated from glasses form solid solutions. Among these, the composition of mica can be varied in a large range. Spinel (MgAl_2O_4) is another example where MgO can be partially or completely substituted by divalent transition metal oxides such as FeO [613,614], ZnO [615], NiO [616,617], CoO [617,618], CuO [619] or MnO [620,621]. Al_2O_3 can be substituted by Fe_2O_3 [614], Cr_2O_3 [613,614], V_2O_5 [613,614], Co_2O_3 [620], Mn_2O_3 [620] or Ga_2O_3 [622]. Furthermore, Li^+ can be incorporated at Mg^{2+} sites [621] and Ti^{4+} at Al^{3+} sites [615]. Many other substitutions are also possible but a comprehensive description is beyond the scope of this review.

The chemical composition of perovskites can also be varied in a wide range. Starting from, e.g., BaTiO_3 , BaO can be replaced by CaO [623], SrO [624] or PbO [625,626], while TiO_2 can be substituted by ZrO_2 [625–629] or SnO_2 [629–632]. These substitutions affect the T_{Curie} of ferroelectric BaTiO_3 , its dielectric constant, the attributed temperature dependency as well as its piezoelectric constants. Furthermore, Ti^{4+} can also be substituted by Nb^{5+} , Ta^{5+} [632,633] or Sc^{3+} [634] and rare earth ions while Ba^{2+} can be replaced by rare earth cations [635–638], Bi^{3+} [638] or Li^+ , Na^+ and K^+ [632,633].

The melilite family [639–642] contains solid solutions which can be precipitated from glasses such as \AA kermanite ($\text{Ca}_2\text{MgSi}_2\text{O}_7$) and gehlenite ($\text{Ca}_2\text{Al}_2\text{SiO}_7$) solid solutions (AGSS). Starting from the gehlenite structure, two Al^{3+} cations of gehlenite are replaced by one Mg^{2+} and one Si^{4+} ion to obtain \AA kermanite [639,641,642]. Furthermore, Zn^{2+} as well as other divalent transition metal cations may replace Mg^{2+} in the crystal structure [455]. Gehlenite, \AA kermanite, melilite as well as the solid solutions derived thereof, are tetragonal with the space group $P\bar{4}2_1m$ [643–645]. In the temperature range from 25 to 925°C , \AA kermanite and gehlenite respectively have CTEs of 7.88 and $10 \cdot 10^{-6} \text{ K}^{-1}$. The composition of the formed solid solution and hence the CTE can be adjusted by the composition of the parent glass.

$\text{BaZn}_2\text{Si}_2\text{O}_7$ also forms solid solutions in a wide range. ZnO can be replaced by other divalent transition metal oxides such as CoO [84,91,461], NiO [91], CuO [91], MnO [91] or MgO [462,606]. BaO can be substituted by SrO [90] and SiO_2 by GeO_2 [646] which all drastically affect the T_{f} and the accompanying volume effect. For example, the T_{f} of $\text{BaZn}_2\text{Si}_2\text{O}_7$ is 280°C but a full replacement of ZnO by CoO results in $T_{\text{f}} = 850^\circ\text{C}$. Replacing BaO by SrO shifts T_{f} to lower temperatures, even below RT. The low temperature phase has a composition dependent CTE of $12\text{--}16 \cdot 10^{-6} \text{ K}^{-1}$ while the high temperature phase has a very low or even negative CTE [90]. Both the T_{f} and the CTE can be varied in an extremely wide range in this system [91,92].

The advantage of precipitating solid solutions from glasses is that physical properties can be continuously varied, i.e., tuned to an

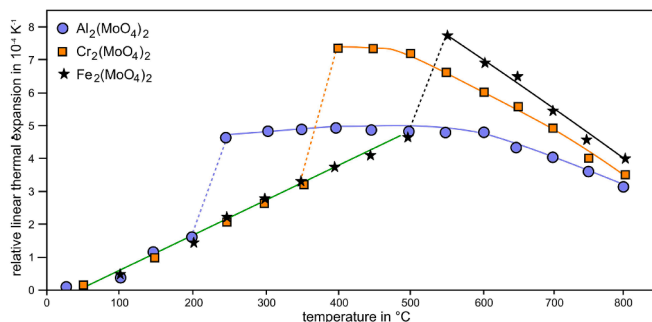


Fig. 30. Thermal expansions of $\text{Al}_2(\text{MoO}_4)_2$, $\text{Cr}_2(\text{MoO}_4)_2$ and $\text{Fe}_2(\text{MoO}_4)_2$. The sharp increase in length is attributed to a phase transition and depends on the chemical composition, based on Ref. [647].

application. Solid solutions with the compositions $\text{BaZn}_{2-x}\text{Mg}_x\text{SiO}_7$ show a T_t increase with an increasing MgO concentration [606]. The linear thermal expansion up to T_t first decreases from $x=0$ to $x=0.2$ and then continuously increases with increasing MgO concentrations. This enables an accurate adjustment of the CTE by tailoring the chemical composition. The systems $\text{M}_2(\text{MoO}_4)_2$ (with $\text{M}=\text{Al}$, Cr and Fe) show an analogous phase transition running parallel to a notable increase in volume as shown in Fig. 30. According to Chapter 3.6.2, such phase transitions enable to introduce well defined stresses during cooling. This effect can be further tailored by crystallizing solid solutions in the respective systems.

A wide formation of solid solutions is also observed in the perovskite system. For example the thermal expansion of the solid solution system $\text{LaCo}_{1-x}\text{Cr}_x\text{O}_3$ is shown in Fig. 31. Here the CTE decreases from 23 to $8 \cdot 10^{-6} \text{K}^{-1}$ with an increasing Cr concentration, enabling an wide range for tailoring the CTE via the precipitated perovskites.

By analogy, the CTE in the spinel system is also strongly affected by the formation of solid solutions. While Mn_2CoO_4 exhibits a CTE of $7.4 \cdot 10^{-6} \text{K}^{-1}$ [649], that of MgAl_2O_4 is $9 \cdot 10^{-6} \text{K}^{-1}$ [605]. Higher CTEs are observed in CuCo_2O_4 ($11.5 \cdot 10^{-6} \text{K}^{-1}$ [650]), $\text{MnCu}_{0.5}\text{Co}_{1.5}\text{O}_4$ ($12.3 \cdot 10^{-6} \text{K}^{-1}$ [651]) and MnCo_2O_4 ($13.4 \cdot 10^{-6} \text{K}^{-1}$ [649]). Fig. 32 shows the CTE of $\text{Mn}_x\text{Co}_{3-x}\text{O}_4$ as a function of the chemical composition [649]. The CTE is $13.3 \cdot 10^{-6} \text{K}^{-1}$ for Co_3O_4 ($x=1$) and linearly decreases with increasing Mn_3O_4 contents until reaching $7.2 \cdot 10^{-6} \text{K}^{-1}$ for Mn_2CoO_4 ($x=2$). This example shows that the CTE can be adjusted over a wide range by varying the Mn/Co ratio. The cubic spinel structures have the great advantage that stresses due to anisotropic thermal expansion do not occur.

Not only the CTE of spinel solid solutions can be tailored by its chemical composition over a wide range; their specific electric conductivity and magnetic properties can also be adjusted. While MgAl_2O_4 is an electric insulator and diamagnetic, magnetite (Fe_3O_4) shows a high electric conductivity and is ferrimagnetic. There are multiple further reports on the crystallization of spinel solid solutions from glasses and the resulting physical properties [399,419,652-656].

The T_{Curie} of ferroelectric perovskite solid solutions in the system $(\text{Ba}, \text{Sr})\text{TiO}_3$ and related systems can be shifted to higher values by increasing the BaO/SrO-ratio [657,658]. This helps with the tailoring of physical properties because the volume concentrations can be kept constant, while only the composition of the respective phase is changed by adapting the glass composition and the required temperature/time schedule for crystallization.

Crystallizing phases which incorporate various oxides can also be used to minimize concentration gradients around growing crystals and in turn minimize the volume concentration of the residual glass. Crystallizing phases which form solid solutions with impurities may also help to reduce raw material costs because enriching impurities such as Fe in a residual glass can notably affect its physical properties.

3.8. Comparison of tools to tailor the microstructure and resulting properties

Fig. 33 compares the effects of phase separation, nucleating agents and nucleation inhibitors. At room temperature, immediately after cooling, nuclei are not detectable in the cooled glass (or in phase separated glasses). During thermal treatments at typical temperatures of $T_g \leq T \leq T_g + 50^\circ \text{C}$, nuclei form in one of the phase separated glasses or throughout the bulk if nucleation agents are present. If nucleation inhibitors are present, they typically prevent nucleation at this stage. At temperatures of typically $T_g + 100^\circ \text{C}$ or above, but of course below T_i , the crystals grow until either the elements or space required for growth are depleted. In glasses containing nucleating agents, the target phase is formed on, or around, the heterogenous nuclei. Glasses containing nucleation inhibitors form nuclei in this temperature range which then start to grow.

Fig. 34 presents an overview of some exemplary microstructures, their resulting properties and possible applications. Nanocrystals with a shell, functioning as diffusion barrier and causing a narrow size distribution, do not scatter visible and near infrared light. For the most advantageous applications, the preferably fluoridic crystals should incorporate rare earth and/or transition metal ions with interesting luminescence properties. Possible applications are luminescence materials such as active laser glasses, up-conversion glasses or light converters. Glass-ceramics containing interlocked needles or rods show interesting mechanical properties such as high strengths and a high toughness. Applications are, e.g., dental ceramics based on Li-disilicate. Crystals with pronounced cleavage planes, such as mica, can lead to glass-ceramics with a good machinability which is highly advantageous for molded components. They can be applied in rapid prototyping and bone replacement in plastic surgery. Dendrites form comparably large, well-connected microstructures advantageous for the electric conductivity. They are hence of interest for thermoelectric materials intended for energy harvesting where large-scale and low-cost components are required. For example, magnetite can easily be crystallized from glass in dendritic morphology and has high Seebeck coefficients [659]. To increase the thermoelectric performance (figure of merit), the propagation of phonons has to be suppressed by nano structuration. In contrast to other nanostructured materials [660], the dendritic microstructure is formed by self organization down to the nm-scale. The next example are glass-ceramics containing a phase with a high CTE, or, even better, a phase transition with a high volume contraction during cooling at temperatures below T_g . The resulting high tensile stresses in the radial direction and compressive stresses in tangential direction led to a high strength and fracture toughness. A typical phase exhibiting the required properties is quartz with the α/β -quartz transition, i.e., not highly doped. Finally, solid solutions offer the possibility to minimize the amount of residual glass, i.e., to maximize the crystalline volume concentration. Advantageous crystal phases allowing the incorporation of various compounds and impurities are found in the melilite or perovskite families. Depending on the composition, the resulting properties can be minimum creep, an adjustable CTE, a high ϵ_r , and a tailored Curie temperature. They can, e.g., be applied as dielectric glass-ceramics or seals with a CTE tailored for the specific application.

4. Concluding Remarks and Outlook

Glasses, and in turn glass-ceramics, can incorporate most chemical elements, apart from noble gases, allowing a very high

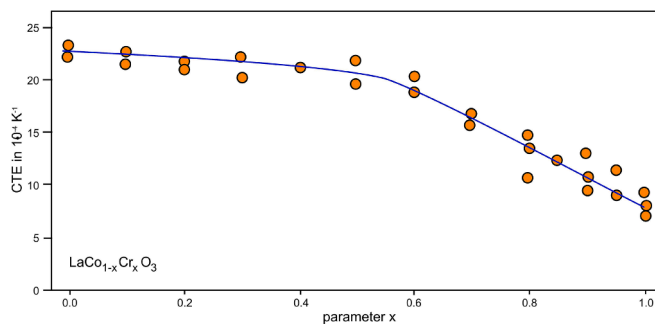


Fig. 31. Thermal expansion of solid solutions in the composition series $\text{LaCo}_{1-x}\text{Cr}_x\text{O}_3$, based on Ref. [648].

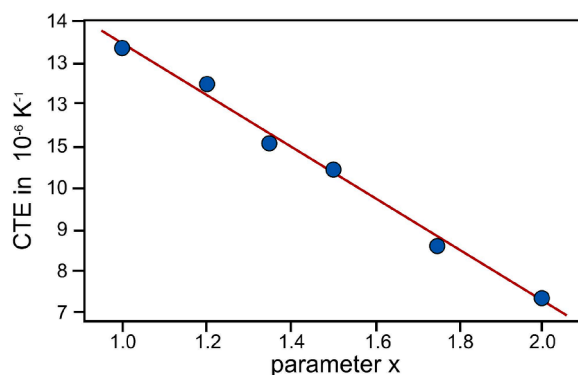


Fig. 32. CTE in the solid solutions series $\text{Mn}_x\text{Co}_{3-x}\text{O}_4$, based on Ref. [649].

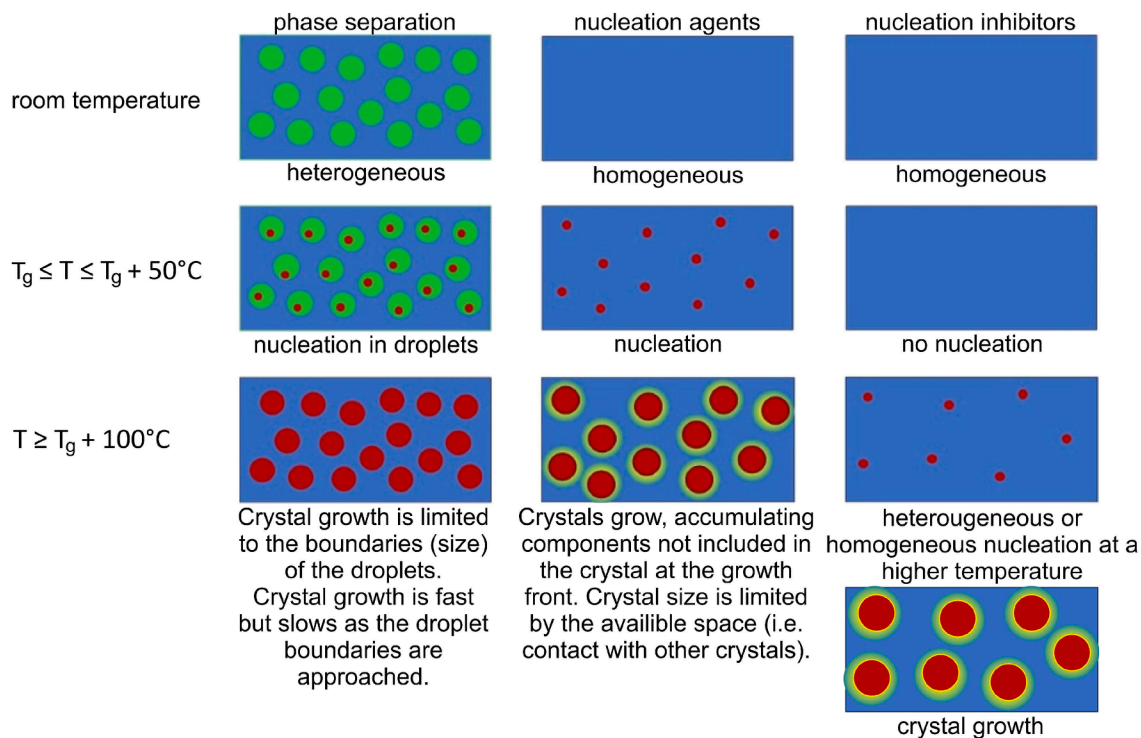


Fig. 33. Schematic illustration of the effects of phase separation, nucleating agents and nucleation inhibitors. Please note that the stated temperature ranges are typical, other ranges are advantageous in many glass compositions.

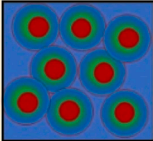

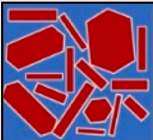
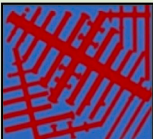

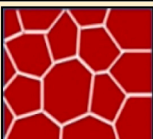
	microstructure	property	application	example phases
nano crystals with a shell		transparent, no light scattering in the visible range	photonic materials luminescence up-conversion materials	rare earth doped alkaline earth fluorides
interlocked needles or rods		high mechanical toughness and strength	dental materials mechanical components	Li-disilicate fluoroapatite mullite
plates with cleavage planes		high cleavability	machinable glass-ceramics	mica
dendrites		high electric and thermal conductivity	thermoelectric devices	magnetite
stresses induced by a high crystal CTE		high mechanical strength and toughness	mechanical components	low-quartz
solid solutions		minimum creep tailored CTE, ϵ_r and T_{Curie}	seals dielectrics	mellite perovskite

Fig. 34. Overview of microstructures and examples of the resulting properties and applications.

variability of chemical compositions. Additionally, stresses can be introduced or removed and the degree of crystallinity can be adapted. Consequentially, the physical and chemical properties of these materials are widely tuneable. Even restricting the field to non-toxic components leaves a high variability, and glass-ceramics containing hazardous compounds such as Tl, Cd or As are no longer industrially produced to the best of our knowledge. Only Pb-containing glass-ceramics are still being produced for special electronic or optoelectronic applications. The chemical durability of most applied glass-ceramics is very high, but they do degrade when exposed to soil or aqueous environments for a time scale of decades or centuries. Even the durability of lithium disilicate glass-ceramics is sufficient for dental applications [42,45,100]. Hence, in contrast to organic polymers, their environmental impact is limited. Furthermore, glasses and glass-ceramics can serve as raw material reservoirs in a circular economy; they can be fully recycled without a degradation of their physical properties.

There are many fields where a disruptive development can be expected. Currently, the most rapidly developing field are nano crystalline glass-ceramics, which include the above noted ruby and photochromic glass-ceramics but also PTR materials. Irradiating the parent glasses with interfering light followed by crystallization via a thermal treatment enables to produce alternating layers with different refractive indices [348,661] which act as Bragg Gratings and can be used to adjust the wavelength of lasers or laser diodes. Glass-ceramics containing crystals of AgBr [661], AgCl/NaCl solid solutions [662] or CaF_2 [350] grown on silver nano crystals are currently under development for applications such as holograms, but possibilities to increase the difference in the refractive indices are also of interest because this would enable to miniaturize devices such as Bragg gratings.

Other future applications of nano crystalline glass-ceramics include light converting materials to produce a warm white light from LEDs. In contrast to luminescent ceramics and phosphors embedded in polymers, the glass-ceramics minimize visible light scattering. In the near future, light converting materials are probably the largest potential application for luminescent glass-ceramics. They are suitable for high intensity applications where polymer matrix composites are not applicable. Further potential applications are active laser materials in a large wavelength range from the visible range to around $2.5 \mu\text{m}$ as optical losses can be minimal. In principle, fibre laser cores may also be produced using glass-ceramics, but here precipitating the required nano crystals with a narrow size distribution during fibre cooling requires a very delicate tailoring of the glass composition. Here re-heating the glass to nucleate and crystallize it

should be impossible as that would immediately cause a strong decrease of the mechanical strength. One promising example in this field is the precipitation of nano crystalline rare earth doped BaF_2 while drawing a $\text{BaF}_2/\text{ZnO}/\text{B}_2\text{O}_3$ glass fibre without the necessity of a subsequent crystallization step [663].

Up conversion glass-ceramics transferring two photons of infrared light to one photon of visible light would be a great advantage to widen the exploitable spectrum for solar energy harvesting and increase solar cell efficiency. By analogy, nano crystalline glass-ceramics showing the effect of quantum cutting may contribute to a more effective exploitation of UV light by semiconductors. Here a high energy photon is transferred to two photons of lower energy which are still above the semiconductor band gap energy, increasing the quantum efficiency.

Another rapidly developing field are glass-ceramics with special mechanical properties. Here, high Young's Moduli and high hardness are especially valuable for armour applications. In comparison to state-of-the-art materials such as α -alumina with very high Young's Moduli, glass-ceramics with comparatively high Young's Moduli show far smaller densities which is, e.g., advantageous in automotive engineering. The high strength and high fracture toughness of such materials are also favourable for dental applications such as 3-unit bridges as they are easier to machine than state of the art ZrO_2 based materials.

Glass-ceramics for medical applications such as bone replacement/repairing are currently being improved with respect to their mechanical properties and resorption rates. They can, e.g., be produced from phosphate or phosphosilicate glasses and can be biocompatible, bioactive or even bioresorbable. Resorbable osteosynthesis materials could replace the currently used metals which frequently require a surgical removal after the bones are healed.

Another growing field is that of crystallizing glass seals. They are especially advantageous, if materials with high CTEs (e.g., $\geq 10 \cdot 10^{-6} \text{ K}^{-1}$) are to be sealed and the application temperature is high, e.g., $> 800^\circ\text{C}$ (as in high temperature fuel cells). Here non-crystallizing glass seals are not feasible because their T_g is either far below the operating temperature or their CTE is much too small. One major problem in this field is the adhesion of the glass-ceramic seal to metals. Seals chemically reacting with the metal have the potential for a strong adherence and the strategies known from enamelling should be very useful in this field. Glasses containing CoO [83] or NiO [460] can, e.g., react with an Fe containing alloy yielding metallic Co and Fe-oxide which then dissolves in the glass. This is accompanied by interface roughening and a strong mechanical interlocking.

Rapidly crystallizing glass seals can also decrease the sealing time and save energy, e.g., via laser sealing. Although this procedure has recently been successfully applied for sealing $\alpha\text{-Al}_2\text{O}_3$ components within a few minutes [639], appropriate seals to join other materials have not been suggested so far.

Many glass compositions are advantageous ion conductors and can be used in Li-ion batteries. Crystallizing appropriate phases may substantially increase the Li^+ conductivity which has a positive impact on the battery efficiency [664,665]. Here, especially the improvement of ion conductivity as well as of the stability and aging behaviour are the focus of current research [666].

Currently, most commercial glass-ceramics are still classic glass-ceramics where the second production step (crystal growth) is time and energy consuming, requires special facilities and should be avoided if possible. This procedure was considered to be "controlled" crystallization and distinguished from the "wild" crystallization which occurred during cooling [16] and usually led to coarse, often dendritic microstructures without favourable properties and hence avoided.

If higher quantities of small crystals are to be grown during cooling, the composition of a glass melt should be tailored to achieve high nucleation rates at a temperature sufficient to allow notable crystal growth. As noted above, the nucleation rate primarily depends on the interfacial energy of the formed nucleus and the surrounding glass matrix. The interfacial energy for a nucleus in contact with a silicate melt is reported to always range from 0.2 to 0.4 N/m [29]. The interfacial energy for the formation of amorphous droplets in a glass matrix is much lower [110,667,668] and reported to range from 0.004 to 0.010 N/m [110,667]. Hence liquid/liquid phase separation has a much lower activation energy than crystallization. If liquid/liquid phase separation leads to droplets with a low network connectivity, it should also trigger crystallization in the droplets and enable to prepare materials with fine grained microstructures. This strategy has already been realized for the crystallization of fluorides from oxyfluoride silicate melts [669-672]. The crystallization of glass melts by simply cooling them to RT is sometimes denoted as "self-crystallization" [669-674] but such a natural effect, also observed in water or metallic melts, should not be discussed as a technological achievement as the key aspect is tuning the composition. It has recently been reported that an oxidic melt with the composition $33 \text{ CaO} \bullet 9 \text{ MgO} \bullet 13 \text{ AlO}_{1.5} \bullet 45 \text{ SiO}_2$ [673] shows a fine-grained microstructure after cooling. This composition has a network connectivity of 2.42, i.e., near the percolation threshold of 2.40 where no rigid network occurs [316].

The crystallization of $\text{Na}_2\text{MgSiO}_4$ from melts in the system $\text{SiO}_2/\text{Al}_2\text{O}_3/\text{P}_2\text{O}_5/\text{Na}_2\text{O}/\text{MgO}/\text{CaO}$ during cooling was observed in the Refs. [320-322]. Here phase separation and subsequent crystallization occurred during cooling and the obtained glass-ceramics were transparent to translucent depending on the respective chemical compositions. The crystallization of nanocrystalline fluorophlogopite ($\text{NaMg}_3\text{AlSi}_3\text{O}_{10}\text{F}_2$) from a $64.45 \text{ SiO}_2 \bullet 2.96 \text{ Al}_2\text{O}_3 \bullet 10.57 \text{ Na}_2\text{O} \bullet 17.76 \text{ MgO} \bullet 2.02 \text{ CaO} \bullet 2.23 \text{ Na}_2\text{SiF}_6$ melt during cooling was reported in Ref. [323].

So far, only a few papers report fine grained microstructures obtained by directly cooling a glass melt, especially containing oxidic crystals. Utilizing this technique to produce useful materials from nonmetallic inorganic melts is, however, expected to be a rapidly developing field in the future.

Author credit statement

C. Rüssel: Conceptualization, Writing – Original Draft, Supervision

W. Wisniewski: Visualization, Writing – Review & Editing,

CRediT authorship contribution statement

Christian Rüssel: Writing – review & editing, Writing – original draft, Funding acquisition, Conceptualization. **Wolfgang Wisniewski:** Writing – review & editing, Visualization.

Declaration of competing interest

The authors declare that they have no known competing financial interests or personal relationships that could have appeared to influence the work reported in this paper.

Data availability

No data was used for the research described in the article.

References

- [1] Deubener J, Allix M, Davis MJ, Duran A, Höche T, Honma T, et al. Updated definition of glass-ceramics. *J. Non-Cryst. Solids* 2018;501:3–10.
- [2] Allix M, Alahrahe S, Payon F, Suchomel M, Porcher F, Cardinal T, et al. Highly transparent BaAl₄O₇ polycrystalline ceramic obtained by full crystallization from glass. *Adv. Mater.* 2012;24:5570–5.
- [3] Alahrahe S, Al Saghir K, Chenu S, Véron E, Meneses DDS, Becerro AI, et al. Perfectly transparent Sr₃Al₂O₆ polycrystalline ceramic elaborated from glass crystallization. *Chem. Mat.* 2013;25:4017–24.
- [4] Véron E, Garaga MN, Pelloquin D, Cadars S, Suchomel M, Suard E, et al. Synthesis and structure determination of CaSi_{1/3}B_{2/3}O_{8/3}, a new calcium borosilicate. *Inorg. Chem.* 2013;52:4250–8.
- [5] Al Saghir K, Chenu S, Veron E, Payon F, Suchomel M, Genevois C, et al. Transparency through structural disorder: a new concept for innovative transparent ceramics. *Chem. Mater.* 2015;27:508–14.
- [6] Boyer M, Carrion AJF, Ory S, Becerro AI, Villette S, Eliseeva SV, et al. Transparent polycrystalline SrREGa₃O₇ melilite ceramics: potential phosphors for tuneable solid state lighting. *J. Mater. Chem. C* 2016;4:3238–47.
- [7] Boyer M, Alahrahe S, Genevois C, Licheron M, Lefevre FX, Castro C, et al. Enhanced transparency through second phase crystallization in BaAl₄O₇ scintillating ceramics. *Cryst. Growth Des.* 2016;16:386–95.
- [8] Bertrand A, Carreaud J, Chenu S, Allix M, Véron E, Duclère JR, et al. Scalable and formable tellurite-based transparent ceramics for near infrared applications. *Adv. Opt. Mater.* 2016;4:1482–6.
- [9] Fernández-Carrión AJ, Al-Saghir K, Veron E, Becerro AI, Porcher F, Wisniewski W, et al. Local disorder and tuneable luminescence in new Sr_{1-x/2}Al_{2-x}Si_xO₄ (x = 0.2, 0.4 and 0.5) transparent ceramics. *Inorg. Chem.* 2017;56:14446–58.
- [10] Ma X, Li X, Li J, Genevois C, Ma B, Etienne A, et al. Pressureless glass crystallization of transparent yttrium aluminum garnet-based nanoceramics. *Nat. Commun.* 2018;9:1175.
- [11] Boyer M, Yang X, Carrion AJF, Wang Q, Veron E, Genevois C, et al. First transparent oxide ion conducting ceramics synthesized by full crystallization from glass. *J. Mater. Chem. A* 2018;6:5276–89.
- [12] Wisniewski W, Carrión AJF, Schöppe P, Rüssel C, Allix M. Oriented nucleation and crystal growth in SrO-Al₂O₃-SiO₂ tectosilicate glasses. *CrystEngComm* 2018; 20:3455–66.
- [13] Xu J, Wang J, Rakhmatullin A, Ory S, Carrión AJF, Yi H, et al. Interstitial oxide ion migration mechanism in aluminate melilite La_{1+x}Ca_{1-x}Al₃O_{7+0.5x} ceramics synthesized by glass crystallization. *ACS Appl. Energy Mater.* 2019;2:2878–88.
- [14] Stookey SD. Catalyzed crystallization of glass in theory and practice. *Ind. Eng. Chem.* 1959;51:805–8.
- [15] McMillan PW. Glass-ceramics. 2. Ed. London/New York/San Francisco: Academic Press; 1979.
- [16] Vogel W. Glass chemistry. 2. Ed. Berlin/Heidelberg: Springer; 1992.
- [17] Rüssel C, Keding R. A new explanation for the induction period observed during nucleation of lithiumdisilicate glass. *J. Non-Cryst. Solids* 2003;328:174–82.
- [18] Shneidman VA, Weinberg MC. Crystallization of rapidly heated amorphous solids. *J. Non-Cryst. Solids* 1996;194:145–54.
- [19] Davis M. Effect of the growth treatment on two-stage nucleation experiments: The “flushing” effect. *Glastech. Ber. Glass Sci. Technol.* 2000;73(C1):170–7.
- [20] Shneidman VA, Uhlmann DR. The fast cooling/heating rate effects in devitrification of glasses. I. Number of nucleated particles. *J. Chem. Phys.* 1998;108: 1094–102.
- [21] Davis MJ. Effect of the Growth Treatment on Two-Stage Nucleation Experiments. *J. Am. Ceram. Soc.* 2001;84:492–546.
- [22] Wisniewski W, Švančárek P, Pmová A, Parchovianský M, Galusek D. Y₂O₃-Al₂O₃ microsphere crystallization analyzed by electron backscatter diffraction (EBSD). *Sci. Rep.* 2020;10:11122.
- [23] Pmová A, Plško A, Klement R, Valúchová J, Haladějová K, Švančárek P, et al. Crystallization kinetics of binary La₂O₃-Al₂O₃ glass. *J. Non-Cryst. Solids* 2018; 501:55–61.
- [24] Mei L, He G, Wang L-L, Liu G-H, Li J-T. Fabrication of transparent LaAlO₃/t-ZrO₂ nanoceramics through controlled amorphous crystallization. *J. Eur. Ceram. Soc.* 2011;31:1603–9.
- [25] Boccacini AR, Chen Q, Lefebvre L, Gremillard L, Chevalier J. Sintering, crystallisation and biodegradation behaviour of Bioglass®-derived glass-ceramics. *Faraday Discuss.* 2007;136:27–44.
- [26] Chen G-H, Liu X-Y. Sintering, crystallization and properties of MgO-Al₂O₃-SiO₂ system glass-ceramics containing ZnO. *J. Alloys Comp.* 2007;431:282–6.
- [27] Reddy AA, Goel A, Tulyaganov DU, Kapoor S, Pradeesh K, Pascual MJ, et al. Study of calcium-magnesium-aluminum-silicate (CMAS) glass and glass-ceramic sealant for solid oxide fuel cells. *J. Power Source* 2013;231:203–12.
- [28] Thieme C, Schlesier M, Bocker C, de Souza GB, Rüssel C. Thermal expansion of sintered glass-ceramics in the system BaO-SrO-ZnO-SiO₂ and its dependence on the particle size. *ACS Appl. Mater. Interf.* 2016;8:20212–9.
- [29] Fokin VM, Zannotto ED, Yuritsyn NS, Schmelzer JWP. Homogeneous crystal nucleation in silicate glasses: A 40 years perspective. *J. Non-Cryst. Solids* 2006;352: 2681–714.
- [30] Pannhorst W. Overview. In: Bach H, editor. Low thermal expansion glass-ceramics. Berlin, Heidelberg, New York: Springer; 1995. p. 1–12.
- [31] Dudek R, Krause C, Kristen K, Naß P, Schaupert K, Scheidler H, et al. Glass-ceramics for household appliances. In: Bach H, editor. Low thermal expansion glass-ceramics. Berlin: Springer; 1995. p. 75–80.
- [32] Kiefer W, Pannhorst W. Glass-ceramics for household appliances. Zerodur—A low thermal expansion glass ceramic for optical precision applications. In: Bach H, editor. Low thermal expansion glass-ceramics. Berlin: Springer; 1995. p. 107–30.
- [33] Borens M, Gabelmann T, Leroux M, Münch T. Glass-ceramics for household appliances. In: Bach H, editor. Low thermal expansion glass-ceramics. Berlin: Springer; 1995. p. 103–6.
- [34] Höland W, Vogel W, Mortier WJ, Duvigneaud PH, Nassens G, Plumet E. A new type of phlogopite crystal in machineable glass-ceramics. *Glass Technol.* 1983; 24:318–22.
- [35] Höland W, Zlateva K, Vogel W. Kinetik der Phasenbildung in Phlogopitglaskeramiken. *Z. Chem.* 1982;22:197–202.

- [36] Grossman DG. Machinable Glass-Ceramics based on tetrasilic mica. *J. Am. Ceram. Soc.* 1972;55:446–9.
- [37] Baik DS, No KS, Chun J-S-S, Yoon YJ. Mechanical properties of mica glass-ceramics. *J. Am. Ceram. Soc.* 1995;78:1217–22.
- [38] Neo M, Kotani S, Fujita Y, Nakamura T, Yamamuro T, Banda Y, et al. Differences in ceramic–bone interface between surface-active ceramics and resorbable ceramics: A study by scanning and transmission electron microscopy. *J. Biomed. Mater. Res.* 1992;26:255–67.
- [39] Hill R, Wood D. Apatite-mullite glass-ceramics. *J. Mater. Sci.: Mater. Medicine* 1995;6:311–8.
- [40] Vogel W, Höland W. Zur Entwicklung von Bioglasceramiken für die Medizin. *Angew. Chem.* 1987;99:541–58.
- [41] Dittmer M, Rüssel C. Colorless and high strength MgO/Al₂O₃/SiO₂ glass-ceramic dental materials using zirconia as nucleating agent. *J. Biomed. Mater. Res. B* 2012;100:463–70.
- [42] Apel E, van't Hoen C, Rheinberger V, Höland W. Influence of ZrO₂ on the crystallization and properties of lithium disilicate glass-ceramics derived from a multi-component system. *J. Eur. Ceram. Soc.* 2007;27:1571–7.
- [43] Zhang F, Reveron H, Spies BC, van Meerbeek B, Chevalier J. Trade-off between fracture resistance and translucency of zirconia and lithium-disilicate glass-ceramics for monolithic restorations. *Acta Biomaterialia* 2019;91:24–34.
- [44] Montazerian M, Bairo F, Fiume E, Migneco C, Alaghmandfard A, Sedighi O, et al. Glass-ceramics in dentistry: Fundamentals, technologies, experimental techniques, applications, and open issues. *Prog. Mater. Sci.* 2023;132:101023.
- [45] Höland W, Apel E, van't Hoen Ch, Rheinberger V. Studies of crystal phase formations in high-strength lithium disilicate glass–ceramics. *J. Non-Cryst. Solids* 2006;352:4041–50.
- [46] Seidel S, Dittmer M, Höland W, Rüssel C. High strength, translucent glass-ceramics in the system MgO-ZnO-Al₂O₃-SiO₂-ZrO₂. *J. Eur. Ceram. Soc.* 2017;37:2685–94.
- [47] Seidel S, Dittmer M, Wisniewski W, Höland W, Rüssel C. Effect of the ZrO₂ concentration on the crystallization behaviour and the mechanical properties of high strength MgO-Al₂O₃-SiO₂ glass-ceramics. *J. Mater. Sci.* 2017;52:1955–68.
- [48] Herrmann A, El-Shahat MAM, Bocker C, Rüssel C. The nano-crystallization and luminescence in the visible spectra of thulium doped Na₂O/K₂O/CaO/Al₂O₃/CaF₂/SiO₂ glasses. *J. Lumin.* 2018;194:321–6.
- [49] Herrmann A, Tylkowski M, Bocker C, Rüssel C. Cubic and hexagonal NaGdF₄ crystals precipitated from an aluminosilicate glass-preparation and luminescence properties. *Chem. Mater.* 2013;48:3461–8.
- [50] Fedorov PP, Luginina AA, Popov AI. Transparent oxyfluoride glass ceramics. *J. Fluorine Chem.* 2015;172:22–50.
- [51] Kemere M, Sperga J, Rogulis U, Kriek G, Grube J. Luminescence properties of Eu, RE³⁺ (RE= Dy, Sm, Tb) co-doped oxyfluoride glasses and glass–ceramics. *J. Lumin.* 2017;181:25–30.
- [52] Kemere M, Rogulis U, Sperga J. Luminescence and energy transfer in Dy³⁺/Eu³⁺ co-doped aluminosilicate oxyfluoride glasses and glass-ceramics. *J. Alloy. Compd.* 2018;735:1253–61.
- [53] Kawamoto Y, Kanno R, Qiu J. Upconversion luminescence of Er³⁺ in transparent SiO₂-PbF₂-ErF₃ glass-ceramics. *J. Mater. Sci.* 1998;33:63–7.
- [54] Chen D, Yu Y, Wang Y, Huang P, Weng F. Cooperative energy transfer up-conversion and quantum cutting down-conversion in Yb³⁺:TbF₃ nanocrystals embedded glass-ceramics. *J. Phys. Chem. C* 2009;113:6406–10.
- [55] Takahashi M, Izumi K, Kanno R, Kawamoto Y. Up-conversion characteristics of Er³⁺ in transparent oxyfluoride glass–ceramics. *J. Appl. Phys.* 1998;83:3920–2.
- [56] Lin C, Bocker C, Rüssel C. Nanocrystallization in oxyfluoride glasses, controlled by amorphous phase separation. *Nano Lett.* 2015;15:6764–9.
- [57] de Pablos-Martín A, Ristic D, Bhattacharyya S, Höche T, Mather GC, Ramírez MO, et al. Effects of Tm³⁺ additions on the crystallization of LaF₃ nanocrystals in oxyfluoride glasses: optical characterization and up-conversion. *J. Am. Ceram. Soc.* 2013;96:447–57.
- [58] Bhattacharyya S, Bocker C, Heil T, Jinschek JR, Höche T, Rüssel C, et al. Experimental evidence of self-limited growth of nanocrystals in glass. *Nano Lett.* 2009;9:2493–6.
- [59] Rüssel C. Nano-crystallization of CaF₂ from Na₂O/K₂O/CaO/CaF₂/Al₂O₃/SiO₂ glasses. *Chem. Mater.* 2005;17:5843–7.
- [60] de Pablos-Martín A, Hémono N, Mather GC, Bhattacharyya S, Höche T, Bornhöft H, et al. Crystallization kinetics of LaF₃ nanocrystals in an oxyfluoride glass. *J. Am. Ceram. Soc.* 2011;94:2420–8.
- [61] de Pablos-Martín A, Mather GC, Muñoz F, Bhattacharyya S, Höche T, Jinschek JR, et al. Design of oxy-fluoride glass-ceramics containing NaLaF₄ nano-crystals. *J. Non-Cryst. Solids* 2010;356:3071–9.
- [62] de Pablos-Martín A, Muñoz F, Mather GC, Patzig C, Bhattacharyya S, Jinschek JR, et al. KLaF₄ nanocrystallisation in oxyfluoride glass-ceramics. *CrystEngComm* 2013;15:10323–32.
- [63] Bocker C, Rüssel C. Self organized nano-crystallisation of BaF₂ from Na₂O/K₂O/BaF₂/Al₂O₃/SiO₂ glasses. *J. Eur. Ceram. Soc.* 2009;29:1221–5.
- [64] Lin C, Liu C, Zhao Z, Li L, Rüssel C. Broadband near-IR emission from cubic perovskite Ni:KZnF₃ nanocrystals embedded glass-ceramics. *Opt. Lett.* 2015;40:5263–6.
- [65] Ashbee KHG. Anisotropic glass-ceramics produced by extrusion through opposed dies. *J. Mater. Sci.* 1975;10:911–7.
- [66] Atkinson DIH, McMillan PW. Glass-ceramics with random and oriented microstructures. Pt. 3. Preparation and microstructure of an aligned glass-ceramic. *J. Mater. Sci.* 1977;12:443–50.
- [67] Rüssel C. Oriented crystallization of glass. a review. *J. Non-Cryst. Solids* 1997;219:212–8.
- [68] Wisniewski W, Rüssel C. Oriented surface nucleation in inorganic glasses – a review. *Prog. Mater. Sci.* 2021;118:100758.
- [69] Halliyal A, Safari A, Bhalla AS, Newnham RE. Grain-oriented glass-ceramics: new Materials for hydrophone applications. *Ferroelectrics* 1983;50:45–50.
- [70] Halliyal A, Safari A, Bhalla AS, Newnham RE, Cross LE. Grain-oriented glass-ceramics for piezoelectric devices. *J. Am. Ceram. Soc.* 1984;67:331–5.
- [71] Halliyal A, Bhalla AS, Newnham RE. Polar glass-ceramics – a new family of electroceramic materials: tailoring the piezoelectric and pyroelectric properties. *Mater. Res. Bull.* 1983;18:1007–19.
- [72] Patschger M, Wisniewski W, Rüssel C. Piezoelectric glass-ceramics produced via oriented growth of Sr₂TiSiO₈ fresnoite: thermal annealing of surface modified quenched glasses. *CrystEngComm* 2012;14:7368–73.
- [73] Lahav M, Leiserowitz L. A stereochemical approach that demonstrates the effect of solvent in the growth of polar crystals: a perspective. *Cryst. Growth Des.* 2006;6:620–4.
- [74] Rüssel C, Wisniewski W. How can surface crystallized glass-ceramics be piezoelectric? *Cryst. Growth Des.* 2021;21:2405–15.
- [75] Wisniewski W, Thieme K, Rüssel C. Fresnoite glass-ceramics – a review. *Prog. Mater. Sci.* 2018;98:68–107.
- [76] Nishida T, Kubuki S, Takashima Y, Mikami M, Yagi T. Laser- and gamma-ray induced crystallization of IR-transmitting calcium gallate glass. *Hyperfine Interactions* 1994;94:2125–30.
- [77] Satu R, Benino Y, Fujiwara T, Komatsu T. YAG laser-induced crystalline dot patterning in samarium tellurite glasses. *J. Non-Cryst. Solids* 2001;289:228–32.
- [78] Komatsu T, Honma T. Nucleation and crystal growth in laser-patterned lines in glasses. *Frontiers Mater.* 2016;3:32.
- [79] Komatsu T, Honma T. Laser patterning and growth mechanism of orientation designed crystals in oxide glasses: A review. *J. Solid State Chem.* 2019;275:210–22.
- [80] Savytskii D, Musterman E, Dierolf V, Jain H. Influence of the Laser Scanning Rate on the Structure of Rotating Lattice Single Crystal Lines. *Cryst. Growth Des.* 2019;19:6324–30.
- [81] McAnany SD, Veenhuizen KJ, Kiss AM, Thieme J, Nolan DA, Aitken BG, et al. Evolution of glass structure during femtosecond laser assisted crystallization of LaBGeO₅ in glass. *J. Non-Cryst. Solids* 2021;551:120396.
- [82] Stone A, Sakakura M, Shimotsuma Y, Stone G, Gupta P, Miura K, et al. Formation of ferroelectric single-crystal architectures in LaBGeO₅ glass by femtosecond vs. continuous-wave lasers. *J. Non-Cryst. Solids* 2010;356:3059–65.
- [83] Thieme C, Rüssel C. Cobalt containing glass seals for solid oxide fuel cells – a new strategy for strong adherence to metals and high thermal expansion. *J. Power Sources* 2014;258:182–8.
- [84] Kerstan M, Thieme C, Grosch M, Müller M, Rüssel C. BaZn₂Si₂O₇ and the solid solution series BaZn_{2-x}Co_xSi₂O₇ (0 < x ≤ 2) as high temperature seals for solid oxide fuel cells studied by high temperature X-ray diffraction and dilatometry. *J. Solid State Chem.* 2013;207:55–60.

- [85] Nguyen XV, Chang CT, Jung GB, Chan SH, Lee WT, Chang SW, et al. Study of sealants for SOFC. *Int. J. Hydrog. Energy* 2016;41:21812–9.
- [86] Zhang X, Liu B, Yang Y, Li J, Li J, Zhao Y, et al. Advances in component and operation optimization of solid oxide electrolysis cell. *Chin. Chem. Lett.* 2022;34:108035.
- [87] Mahapatra MK, Lu K. Glass-based seals for solid oxide fuel and electrolyzer cells – A review. *Mater. Sci. Eng. R* 2010;67:65–85.
- [88] Lessing PA. A review of sealing technologies applicable to solid oxide electrolysis cells. *J. Mater. Sci.* 2007;42:3465–76.
- [89] Wange P, Höche T, Rüssel C, Schnapp J-D. Microstructure – property relationship in high – strength MgO – Al₂O₃ – SiO₂ – TiO₂ glass-ceramics. *J. Non-Cryst. Solids* 2002;298:137–45.
- [90] Thieme C, Görls H, Rüssel C. Ba_{1-x}Sr_xZn₂Si₂O₇-A new family of materials with giant negative and very high thermal expansion. *Sci. Rep.* 2015;5:18040.
- [91] Thieme C, Rüssel C. Very high or close to zero thermal expansion by the variation of the Sr/Ba ratio in Ba_{1-x}Sr_xZn₂Si₂O₇ solid solutions. *Dalton Trans.* 2016;45:4888–95.
- [92] Thieme C, Waurischk T, Heitmann SL, Rüssel C. A new family of materials with negative coefficients of thermal expansion – The effect of MgO, CoO, MnO, NiO or CuO on the phase stability and thermal expansion of solid solution phases derived from BaZn₂Si₂O₇. *Inorg. Chem.* 2016;55:4476–84.
- [93] Harizanova R, Völksch G, Rüssel C. Crystallization and microstructure of glasses in the system Na₂O/MnO/SiO₂/Fe₂O₃. *Mater. Res. Bull.* 2011;46:81–6.
- [94] Wisniewski W, Patscher M, Rüssel C. Viscous fingering and dendritic growth of surfaces crystallized Sr₂TiSi₂O₈ fresnoite. *Sci. Rep.* 2013;3:3558.
- [95] Couder Y, Cardoso O, Dupuy D, Tavernier P, Thom W. Dendritic growth in the Saffman-Taylor experiment. *Europhys. Lett.* 1986;2:437–43.
- [96] Buka A, Kertész J, Vicsek T. Transitions of viscous fingering patterns in nematic liquid crystals. *Nature* 1986;323:424–5.
- [97] DiFrancesco MW, Rauseo SN, Maher JV. Viscous fingering as a first step toward understanding dendrites. *Superlatice. Microst.* 1987;3:617–23.
- [98] Ben-Jacob E, Godbey R, Goldenfeld ND, Koplik J, Levine H, Mueller T, et al. Experimental demonstration of the role of anisotropy in interfacial pattern formation. *Phys. Rev. Lett.* 1985;55:1315–8.
- [99] Höland W, Beall GH. Glass-ceramic technology. Hoboken, New Jersey: John Wiley & Sons; 2019.
- [100] von Clausbruch SC, Schweiger M, Höland W, Rheinberger V. The effect of P₂O₅ on the crystallization and microstructure of glass-ceramics in the SiO₂-Li₂O-K₂O-ZnO-P₂O₅ system. *J. Non-Cryst. Solids* 2000;263–264:388–94.
- [101] Fu L, Engqvist H, Xia W. Glass-ceramics in dentistry: A review. *Mater.* 2020;13:1049.
- [102] Hallmann L, Ulmer P, Kern M. Effect of microstructure on the mechanical properties of lithium disilicate glass-ceramics. *J. Mech. Behavior Biomed. Mater.* 2018;82:355–70.
- [103] W. Vogel, Glass Chemistry, Springer, Berlin/Heidelberg, 2. Ed., 1992, p. 209.
- [104] Heidenreich E, Doenitz F-D, Ehrh R, Vogel W. Zur gesteuerten Kristallisation im Glas I: Der Einfluß von Fluor auf Phasentrennung und Kristallisation in einem MgO-Al₂O₃-SiO₂-Grundglas. *Silikattechnik* 1974;25:225–6.
- [105] S. M. Ohlberg, H. R. Golob, D. W. Strickler, Crystal Nucleation by Glass in Glass Separation, in: “Symposium on Nucleation and Crystallization in Glasses and Melts”, The American Ceramic Society (1962) pp. 55-62.
- [106] Vogel W. Inter-relationships between microheterogeneity, nucleation, and crystallization in glasses. *Glass Technol.* 1966;7:15–21.
- [107] Vogel W. Structure and Crystallization of Glasses. Oxford, UK: Pergamon Press; 1971.
- [108] Harizanova R, Völksch G, Rüssel C. Microstructures formed during devitrification of Na₂O•Al₂O₃•B₂O₃•SiO₂•Fe₂O₃. *J. Mater. Sci.* 2010;45:1350–3.
- [109] Bocker C, Herrmann A, Loch P, Rüssel C. The nano-crystallization and fluorescence of terbium doped Na₂O/K₂O/CaO/CaF₂/Al₂O₃/SiO₂ glasses. *J. Mater. Chem. C* 2015;3:2274–81.
- [110] Zanutto ED. Effect of liquid phase separation on crystal nucleation in glass-formers. Case Closed. *Ceram. Int.* 2020;46:24779–91.
- [111] Moisesescu C, Jana C, Rüssel C. Crystallization of rod-shaped fluoroapatite from glass melts in the system SiO₂/Al₂O₃/CaO/P₂O₅/Na₂O/K₂O/F. *J. Non-Cryst. Solids* 1999;248:169–75.
- [112] I. Gutzow, J. Schmelzer, The vitreous state thermodynamics, structure, rheology, and crystallization, Springer: Berlin, Heidelberg, New York, 2013 (2nd ed.).
- [113] Montazerian M, Zanutto ED. Nucleation, growth, and crystallization in oxide glass-formers. A current perspective. *Rev. Mineral. Geochem.* 2022;87:405–29.
- [114] Kaur G, Kumar V, Bano F, Mauro JC, Pickrell G, Evans I, et al. Mechanical properties of bioactive glasses, ceramics, glass-ceramics and composites: State-of-the-art review and future challenges. *Mater. Sci. Eng. C* 2019;104:109895.
- [115] Fernandes HR, Gaddam A, Rebelo A, Brazete D, Stan GE, Ferreira JM. Bioactive glasses and glass-ceramics for healthcare applications in bone regeneration and tissue engineering. *Mater.* 2018;11:2530.
- [116] Kleebusch E, Rüssel C, Patzig C, Höche T. Evidence of epitaxial growth of high-quartz solid solution on ZrTiO₄ nuclei in a Li₂O-Al₂O₃-SiO₂ glass. *J. Alloy. Compd.* 2018;748:73–9.
- [117] Schwartz AJ, Kumar M, Adams BL, Field DP. Electron Backscatter Diffraction in Materials Science. 2nd Edition. New York: Springer; 2009.
- [118] Wisniewski W, Saager S, Böbenroth A, Rüssel C. Experimental evidence concerning the significant information depth of electron backscatter diffraction (EBSD). *Ultramicroscopy* 2017;173:1–9.
- [119] Keshavarzi A, Wisniewski W, Rüssel C. EBSD and EDX analyses of a glass-ceramic multi phase obtained by crystallizing an yttrium aluminosilicate glass. *ACS Appl. Mater. Interfaces* 2013;5:8531–6.
- [120] Gibbs JW. The Collected Works, Thermodynamics, Vol. 1. New York: Longmans & Green; 1928.
- [121] Volmer M, Weber A. Keimbildung in übersättigten Gebilden. *Phys. Chem.* 1926;119:277–301.
- [122] Volmer M. Kinetik der Phasenbildung. Dresden: Steinkopf; 1939.
- [123] Becker R, Döring W. Kinetische Behandlung der Keimbildung in übersättigten Dämpfen. *Ann. Phys.* 1935;24:719–52.
- [124] Kaischew R, Stranski IN. Zur kinetischen Ableitung der Keimbildungsgeschwindigkeit. *Z. Phys. Chem. B* 1934;26:317–26.
- [125] Turnbull D, Fisher JC. Rate of nucleation in condensed systems. *J. Chem. Phys.* 1949;17:71–3.
- [126] Tammann G. Über die Abhängigkeit der Zahl der Kerne, welche sich in verschiedenen unterkühlten Flüssigkeiten bilden, von der Temperatur. *Z. Phys. Chem.* 1898;25:441–79.
- [127] Tammann G. Der Glaszustand. Leipzig, Germany: Leopold Voss; 1933.
- [128] Babushkin VL, Matveyev GM, Mchedlov-Petrosyan OP. Thermodynamics of Silicates. Berlin, Germany: Springer; 1985.
- [129] Kelton KE. Crystal Nucleation in Liquids and Glasses. *Solid State Phys.* 1991;45:75–177.
- [130] Abyzov AS, Fokin VM, Yuritsyn NS, Nascimento ML, Schmelzer JW, Zanutto ED. Crystal nucleation in a glass during relaxation well below T_g. *J. Chem. Phys.* 2023;158:064501.
- [131] Fokin VA, Abyzov AS, Yuritsyn NS, Schmelzer JW, Zanutto ED. Effect of structural relaxation on crystal nucleation in glasses. *Acta Mater.* 2021;203:116472.
- [132] Abyzov AS, Fokin VM, Rodrigues AM, Zanutto ED, Schmelzer JW. The effect of elastic stresses on the thermodynamic barrier for crystal nucleation. *J. Non-Cryst. Solids* 2016;432:325–33.
- [133] Fokin VM, Yuritsyn NS, Zanutto ED, Schmelzer JWP, Cabral AA. Nucleation time-lag from nucleation and growth experiments in deeply undercooled glass-forming liquids. *J. Non-Cryst. Solids* 2008;354:3785–92.
- [134] Yuritsyn NS. Crystal nucleation in soda-lime-silica glass at temperatures below the glass transition temperature. *Glass Phys. Chem.* 2020;46:120–6.
- [135] Kalinina AM, Filipovich VN, Fokin VM. Stationary and Non-Stationary Crystal Nucleation Rates in the Na₂O•2CaO•3SiO₂ Glass of Stoichiometric Composition. *J. Non-Cryst Solids* 1980;38–39:723–8.
- [136] V. M. Fokin, N. S. Yuritsyn, E. D. Zanutto, Nucleation and crystallization kinetics in silicate glasses: theory and experiment, in J. W. P. Schmelzer (Ed.): “Nucleation theory and applications”, Wiley-VCH, (2005) 74-125.
- [137] Schmelzer JWP, Fokin VM, Abyzov AS. Crystallization of glass: What we know, what we need to know. *Intern. J. Appl. Glass Sci.* 2016;7:253–61.
- [138] Fan Z, Men H. An Overview on Atomistic Mechanisms of Heterogeneous Nucleation. *Metals* 2022;12:1547.
- [139] Montazerian M, Zanutto ED. Nucleation, Growth, and Crystallization in Oxide Glass-formers. A Current Perspective. *Rev. Mineral. Geochem.* 2022;87:405–29.
- [140] Turnbull D. Kinetics of Heterogeneous Nucleation. *J. Chem. Phys.* 1950;18:198–203.
- [141] Burgner LL, Weinberg MC. Crystal growth mechanisms in inorganic glasses. *Phys. Chem. Glasses* 2001;42:184–90.

- [142] Nascimento MLF, Fokin VM, Zanutto ED, Abyzov AS. Dynamic processes in a silicate liquid from above melting to below the glass transition. *J. Chem. Phys.* 2011;135:194703.
- [143] Barker MF, Wang T-H, James PF. Nucleation and growth kinetics of lithium disilicate and lithium metasilicate in lithia-silica glasses. *Phys. Chem. Glasses* 1988; 29:240–8.
- [144] Gonzalez-Oliver CJR, Johnson PS, James PF. Influence of water content on the rates of crystal nucleation and growth in lithia-silica and soda-lime-silica glasses. *J. Mater. Sci.* 1979;14:1159–69.
- [145] Burgner LL, Weinberg MC. An assessment of crystal growth behavior in lithium disilicate glass. *J. Non-Cryst. Solids* 2001;279:28–43.
- [146] Fokin VM, Zanutto ED, Schmelzer JWP, Potapov OV. New insights on the thermodynamic barrier for nucleation in glasses: The case of lithium disilicate. *J. Non-Cryst. Solids* 2005;351:1491–9.
- [147] Müller R, Zanutto ED, Fokin VM. Surface crystallization of silicate glasses: nucleation sites and kinetics. *J. Non-Cryst. Solids* 2000;274:208–31.
- [148] Zanutto ED, Craievich AF. The role of amorphous phase separation in crystal nucleation in splat cooled $\text{Li}_2\text{O-SiO}_2$ glasses. *J. Mater. Sci.* 1981;16:973–82.
- [149] Matsusita K, Sakka S, Maki T, Tashiro M. Study on crystallization of glass by differential thermal analysis. Effect of added oxide on crystallization of $\text{Li}_2\text{O-SiO}_2$ glasses. *J. Mater. Sci.* 1975;10:94–100.
- [150] Deubener J, Brückner R, Sternitzke M. Induction time analysis of nucleation and crystal growth in di- and metasilicate glasses. *J. Non-Cryst. Solids* 1993;163: 1–12.
- [151] Matusita K, Tashiro M. Rate of Crystal Growth in $\text{Li}_2\text{O} \cdot 2\text{SiO}_2$ Glass. *Yogyo-Kyokai-Shi* 1973;81:500–6.
- [152] Sharifianjazi F, Parvin N, Tahr M. Formation of apatite nano-needles on novel gel derived $\text{SiO}_2\text{-P}_2\text{O}_5\text{-CaO-SrO-Ag}_2\text{O}$ bioactive glasses. *Ceram. Inter.* 2017;43: 15214–20.
- [153] Duminis T, Shahid S, Hill RG. Apatite glass-ceramics: a review. *Front. Mater.* 2017;3:59.
- [154] Wisniewski W, Pitcher MJ, Veron E, Fan J, Sarou-Kanian V, Fayon F, et al. Allix Macroscopic orientation domains grown via aerodynamic levitation: a path toward single crystals. *Cryst. Growth Des.* 2021;21:3554–61.
- [155] Rindone GE. Influence of platinum nucleation on crystallization of a lithium silicate glass. *J. Am. Ceram. Soc.* 1958;41:41–2.
- [156] Kracker M, Thieme C, Thieme K, Patzig C, Berthold L, Höche T, et al. Gold nanoparticles and crystallization of a glass in the system BaO/SrO/ZnO/SiO_2 . *RSC Adv.* 2018;8:6267–77.
- [157] Höche T, Moisesescu C, Avramov J, Rüssel C, Heerdegen WD. Microstructure of $\text{SiO}_2 - \text{Al}_2\text{O}_3 - \text{CaO} - \text{P}_2\text{O}_5 - \text{K}_2\text{O} - \text{F}$ Glass-ceramics 1. needle like versus isometric morphology of apatite crystals. *Chem. Mater.* 2001;13:1312–9.
- [158] Wisniewski W, Rüssel C. An Experimental Viewpoint on the Information Depth of EBSD. *Scanning* 2016;38:164–71.
- [159] Wisniewski W, Carl R, Völksch G, Rüssel C. Mullite needles grown from a $\text{MgO/Al}_2\text{O}_3\text{/TiO}_2\text{/SiO}_2\text{/B}_2\text{O}_3\text{/CaO}$ glass melt: orientation and diffusion barriers. *Cryst Growth Des.* 2011;11:784–90.
- [160] Wisniewski W, Baptista C, Völksch G, Rüssel C. Surface crystallization of cordierite from glass studied by high temperature X-ray diffraction and electron backscatter diffraction. *Cryst. Growth Des.* 2011;11:4660–6.
- [161] Wisniewski W, Harizanova R, Völksch G, Rüssel C. Crystallisation of iron containing glass-ceramics and the transformation of hematite to magnetite. *CrystEngComm* 2011;13:4025–31.
- [162] Gönnä Gvd, Keding R, Rüssel C. Oriented crystallization of mullite using electrochemical nucleation. *J. Non-Cryst. Solids* 1999;243:109–15.
- [163] Hartmann P, Perdok GW. On the relations between structure and morphology of Crystals I. *Acta Cryst.* 1955;8:49–52.
- [164] Hartmann P, Perdok GW. On the relations between structure and morphology of Crystals II. *Acta Cryst.* 1955;8:521–4.
- [165] Hartmann P, Perdok GW. On the relations between structure and morphology of Crystals III. *Acta Cryst.* 1955;8:525–9.
- [166] Docherty R, Clydesdale G, Roberts KJ, Bennema P. Application of Bravais-Friedel-Donnay-Harker, attachment energy and Ising models to predicting and understanding the morphology of molecular crystals. *J. Phys. D: Appl. Phys.* 1991;24:89–99.
- [167] Schneider H, Fischer RX, Schreuer J. Mullite: crystal structure and related Properties. *J. Am. Ceram. Soc.* 2015;98:2948–67.
- [168] Carl R, Rüssel C. Growth of mullite crystals in $\text{MgO/Al}_2\text{O}_3\text{/TiO}_2\text{/SiO}_2\text{/B}_2\text{O}_3\text{/CaO}$ glasses by electrochemical induced nucleation. *Eur. J. Glass Sci. Technol. B, Phys. Chem. Glasses* 2007;48:271–5.
- [169] Tran R, Xu Z, Radhakrishnan B, Winston D, Sun W, Persson KA, et al. Data descriptor: surface energies of elemental crystals. *Scientific Data* 2016;3:160080.
- [170] Li S, Xu Y, Zhang X, Lu P. Formation and crystal growth of needle-like rutile in glass-ceramics. *J. Eur. Ceram. Soc.* 2022;42:3313–20.
- [171] Garkava R, Völksch G, Rüssel C. Precipitation of SnO_2 nano-crystallites from $\text{Na}_2\text{O/B}_2\text{O}_3\text{/SnO}_2\text{/(Al}_2\text{O}_3)$ glasses. *J. Non-Cryst. Solids* 2005;351:2287–93.
- [172] Toledo-Antonio JA, Gutiérrez-Baez R, Sebastián PJ, Vázquez A. Thermal stability and structural deformation of rutile SnO_2 nanoparticles. *J. Solid State Chem.* 2003;174:241–8.
- [173] Höland W. Biocompatible and bioactive glass-ceramics—state of the art and new directions. *J. Non-Cryst. Solids* 1997;219:192–7.
- [174] Höland W, Rheinberger V, Schweiger M. Control of nucleation in glass ceramics. *Phil. Trans. Soc. Lond. A* 2003;61:575–89.
- [175] Höland W, Ritzberger C, Apel E, Rheinberger V, Nesper R, Krumeich F, et al. Formation and crystal growth of needle-like fluoroapatite in functional glass-ceramics. *J. Mater. Chem.* 2008;18:1318–32.
- [176] Fleet ME, Pan Y. Site preference of Nd in fluorapatite $[\text{Ca}_{10}(\text{PO}_4)_6\text{F}_2]$. *J. Solid State Chem.* 1994;112:78–81.
- [177] Poulon-Quintin A, Ogden E, Large A, Vaudecal M, Labrugère C, Bartal M, et al. Chemical surface modification of lithium disilicate needles of a silica-based ceramic after HF-etching and ultrasonic bath cleaning: Impact on the chemical bonding with silane. *Dent. Mater.* 2021;37:832–9.
- [178] Höland W, Schweiger M, Frank M, Rheinberger V. A comparison of the microstructure and properties of the IPS Empress®2 and the IPS Empress® glass-ceramics. *Dental Biomater.* 2000;53:297–303.
- [179] Taurines T, Boizot B. Microstructure of powellite-rich glass-ceramics: a model system for high level waste immobilization. *J. Am. Ceram. Soc.* 2012;95: 1105–11.
- [180] Höche T, Deckwerth M, Rüssel C. Partial stabilization of tetragonal zirconia in oxynitride glass-ceramics. *J. Am. Ceram. Soc.* 1998;81:2029–36.
- [181] Takeda H. Distribution of mica polytypes among space groups. *Am. Mineral.* 1971;56:1042–56.
- [182] Höche T, Habelitz S, Avramov I. Crystal morphology engineering in $\text{SiO}_2\text{-Al}_2\text{O}_3\text{-MgO-K}_2\text{O-Na}_2\text{O-F}$ mica glass-ceramics. *Acta Mater.* 1999;47:735–44.
- [183] Wisniewski W, Rüssel C. EBSD-measurements of phlogopite glass-ceramics. *Crystengcomm* 2015;17:8671–6.
- [184] Avramov I, Höche T, Rüssel C. Is there a crystallization pendulum? *J. Chem. Phys.* 1999;110:8676–8.
- [185] D. G. Grossman, Glass-ceramic articles with oriented mica crystals. US pat. no. 3905824. Sept. 16, 1975.
- [186] G.H. Beall, Mica glass-ceramics. U.S. Patent No. 3,689,293. 5 Sep. 1972.
- [187] G.H. Beall, Strontium fluor mica glass ceramics. U.S. Patent No. 3,756,838. 4 Sep. 1973.
- [188] Beall GH. Design and properties of glass-ceramics. *Ann. Rev. Mater. Sci.* 1992;22:91–119.
- [189] Tauch D, Rüssel C. Glass-ceramics with zero thermal expansion in the system $\text{BaO/Al}_2\text{O}_3\text{/B}_2\text{O}_3$. *J. Non-Cryst. Solids* 2005;351:2294–8.
- [190] Ye N, Zeng WR, Wu BC, Huang XY, Chen CT. Crystal structure of barium aluminium borate, $\text{BaAl}_2\text{B}_2\text{O}_7$. *Z. Kristallogr. NCS* 1998;213:452.
- [191] Wisniewski W, Zschechel T, Völksch G, Rüssel C. Electron backscatter diffraction of $\text{BaAl}_2\text{B}_2\text{O}_7$ Crystals Grown from the Surface of a $\text{BaO-Al}_2\text{O}_3\text{-B}_2\text{O}_3$ Glass. *CrystEngComm* 2010;12:3105–11.
- [192] Shtukenberg AG, Punin YO, Gunn E, Kahr B. Spherulites. *Chem. Rev.* 2012;112:1805–38.
- [193] Shi Y, Han XX, Li BW, Chen YX, Zhang MX. Modification of glass network and crystallization of $\text{CaO-Al}_2\text{O}_3\text{-MgO-SiO}_2$ based glass-ceramics with addition of iron oxide. *Ceram. Int.* 2020;46:9207–17.
- [194] Truong LN, Dussauze M, Fargin E, Santos L, Vigouroux H, Fargues A, et al. Isotropic octupolar second harmonic generation response in LaBGeO_5 glass ceramic with spherulitic precipitation. *Appl. Phys. Lett.* 2015;106:16190.
- [195] Wisniewski W, Seyring M, Patzig C, Höche T, Keshavarzi A, Rüssel C. Fivefold pseudo symmetry due to monoclinic growth in a matrix containing growth barriers. *Sci. Rep.* 2016;6:19645.

- [196] Wisniewski W, Thieme C, Rüssel C. The detailed microstructure of an alumina-zirconia-silica (AZS) fused cast refractory material from the cast skin into the bulk analyzed using EBSD. *J. Eur. Ceram. Soc.* 2019;39:2186–98.
- [197] He X, Wang Y, Jia K, Zhang Y. Room-temperature homogeneous precipitation of highly uniform BaCO₃ dumbbells in a mixed solvent of ethylene glycol and water. *Mater. Lett.* 2016;181:244–7.
- [198] Liu H, Liu H. Preparing micro/nano dumbbell-shaped CeO₂ for high performance electrode materials. *J. Alloy. Compd.* 2016;681:342–9.
- [199] Gránásky L, Pusztai T, Tegze G, Warren JA, Douglas JF. Growth and form of spherulites. *Phys. Rev. E* 2005;72:011605.
- [200] Carr SM, Subramanian KN. Spherulitic crystal growth in P₂O₅ nucleated lead silicate glass. *J. Cryst. Growth* 1982;60:307–12.
- [201] Zaitsev AI, Zamkov AV, Koroleva NS, Molokheev MS, Cherepakhin AV. Phase Formation upon Crystallization of SrO-2B₂O₃ Glasses. *Cryst. Rep.* 2011;56:44–51.
- [202] Moriceau J, Houzot P, To T, Mougari A, Orain H, Celarié F, et al. Nucleation and crystallization of Ba₂Si₃O₈ spherulites in a barium aluminum silicate glass, and mechanical properties of the obtained glass-ceramics. *J. Eur. Ceram. Soc.* 2021;41:838–48.
- [203] Lewis MH, Smith G. Spherulitic growth and recrystallization in barium silicate glasses. *J. Mater. Sci.* 1976;11:2015–26.
- [204] Knowles KM, Butt H, Batal A, Sabouri A, Anthony CJ. Light scattering and optical diffusion from willemite spherulites. *Opt. Mater.* 2016;52:163–72.
- [205] Butt H, Knowles KM, Montelongo Y, Amaratunga GAJ, Wilkinson TD. Devitrite-based optical diffusers. *ACS Nano* 2014;8:2929–35.
- [206] Vigouroux H, Fargin E, Gomez S, Le Garrec B, Mountrichas G, Kamitsos E, et al. Synthesis and multiscale evaluation of LiNbO₃ – containing silicate glass-ceramics with efficient isotropic SHG response. *Adv. Funct. Mater.* 2012;22:3985–93.
- [207] Wisniewski W, Nagel M, Völksch G, Rüssel C. Irregular fourfold hierarchy in fresnoite dendrites due to secondary crystallization. *Cryst. Growth Des.* 2010;10:4526–30.
- [208] Wisniewski W, Patschger M, Rüssel C. Sr₂TiSi₂O₈ surface crystallization of a 2 SrO-TiO₂-2.75 SiO₂ glass studied by EBSD. *CrystEngComm* 2012;14:5425–33.
- [209] Wange P, Vogel J, Horn L, Höland W, Vogel W. The morphology of phase formations in phosphate glass-ceramics. *Silic. Ind.* 1990;7–8:231–6.
- [210] Gránásky L, Pusztai T, Warren JA, Douglas JF, Börzsönyi T, Ferreira V. Growth of ‘dizzy dendrites’ in a random field of foreign particles. *Nature Mater.* 2003;2:92–6.
- [211] Gránásky L, Pusztai T, Börzsönyi T, Warren JA, Douglas JF. A general mechanism of polycrystalline growth. *Nature Mater.* 2004;3:645–50.
- [212] Keshavarzi A, Wisniewski W, Rüssel C. Dendritic growth of yttrium aluminium garnet from an oxide melt in the system SiO₂/Al₂O₃/Y₂O₃/CaO. *CrystEngComm* 2012;14:6904–9.
- [213] Wisniewski W, Nagel M, Rüssel C. Macroscopic glass permeated single crystals in the system Ba₂TiSi₂O₈/SiO₂. *CrystEngComm* 2015;17:5019–25.
- [214] Wang X, Huang J, Feng H, Li J, Pu Z, Yin X. Facile preparation of the dendritic Fe₃O₄ with a core-shell microstructure in SiO₂-B₂O₃-Al₂O₃-CaO-Fe₂O₃ glass-ceramic system for enhanced microwave absorbing performance. *J. Alloys Comp.* 2021;877:160147.
- [215] Wang X, Huang J, Feng H, Li J, Xu Z, Xiong K, et al. Constructing dendrite-flower-shaped Fe₃O₄ crystals in glass-ceramic materials as novel broadband high-efficient electromagnetic wave absorbers. *J. Alloys Comp.* 2022;901:163541.
- [216] Feng H, Huang J, Wang X, Li J, Yin X, Xu Z, et al. Microstructure and enhanced electromagnetic wave absorbing performance of Zn_{0.6}Ni_{0.3}Cu_{0.1}Fe₂O₄ ferrite glass-ceramic. *Ceram. Inter.* 2022;48:9090–8.
- [217] Wence X, Weili C, Xiaolin J, Xuefeng Z. Effect of magnetic-field heat treatment on directional growth of magnetite in glass ceramics. *Mater. Res. Express* 2019;6:075204.
- [218] Romero M, Rincon JM. Surface and bulk crystallization of glass-ceramic in the Na₂O–CaO–ZnO–PbO–Fe₂O₃–Al₂O₃–SiO₂ system derived from a goethite waste. *J. Am. Ceram. Soc.* 1999;82:1313–7.
- [219] Nandi P, Goswami M, Arya A, Krishnan M. Study of crystallization kinetics, microstructure and optical properties of Ce: YAG glass-ceramics for white LED applications. *J. Thermal Anal. Calorimetry* 2022;147:3007–13.
- [220] Han DF, Zhang QM, Luo J, Tang Q, Dun J. Optimization of energy storage density in ANb₂O₆–NaNbO₃–SiO₂ (A=[(1-x)Pb, xSr]) nanostructured glass–ceramic dielectrics. *Ceram. Inter.* 2012;38:6903–6.
- [221] Wu K, Wang F, Liao Q, Zhu H, Liu D, Zhu Y. Synthesis of pyrochlore-borosilicate glass-ceramics for immobilization of high-level nuclear waste. *Ceram. Inter.* 2020;46:6085–94.
- [222] McCoy M, Lee WE, Heuer AH. Crystallization of MgO–Al₂O₃–SiO₂–ZrO₂ glasses. *J. Am. Ceram. Soc.* 1986;69:292–6.
- [223] Gerace KS, Randall C, Mauro JC. Crystallization of LiNbO₃ and NaNbO₃ in niobosilicate glass–ceramics. *J. Am. Ceram. Soc.* 2023;106:2716–31.
- [224] Lu AX, Ke ZB, Xiao ZH, Zhang XF, Li XY. Effect of heat-treatment condition on crystallization behavior and thermal expansion coefficient of Li₂O–ZnO–Al₂O₃–SiO₂–P₂O₅ glass–ceramics. *J. Non-Cryst. Solids* 2007;353:2692–7.
- [225] Fernandes HR, Tulyaganov DU, Goel IK, Ferreira JMF. Crystallization process and some properties of Li₂O–SiO₂ glass–ceramics doped with Al₂O₃ and K₂O. *J. Am. Ceram. Soc.* 2008;91:3698–703.
- [226] Zou C, Cao J, Zhao M, Wang Z, Lu J. Combined sodium and fluorine promote diopside continuous growth to achieve one-step crystallization in CaO–Al₂O₃–SiO₂–Fe₂O₃ glass–ceramics. *J. Eur. Ceram. Soc.* 2019;39:4979–87.
- [227] Senanon W, Yongsiri P, Eitssayeam C, Tunkasiri T, Pengpat K. Comparison between incorporation and conventional fabrication techniques of diopside-based glass-ceramics. *Mater. Lett.* 2019;249:160–4.
- [228] Fernández-Rodríguez L, Gorni G, Mather GC, Savvin S, Cuello GJ, Durán A, et al. X-ray absorption spectroscopy and neutron-diffraction study of persistent luminescent Sr₂MgSi₂O₇ glass-ceramics. *Acta Mater.* 2021;215:117080.
- [229] Mitchell AL, Smith CM. Influence of composition and microstructure on transparency and diffusivity in ion-exchangeable spinel glass-ceramics. *J. Am. Ceram. Soc.* 2020;103:4925–38.
- [230] Davis C, Nino JC. Microwave processing for improved ionic conductivity in Li₂O–Al₂O₃–TiO₂–P₂O₅ glass-ceramics. *J. Am. Ceram. Soc.* 2015;98:2422–7.
- [231] Stanton KT, O’Flynn KP, Kiernan S, Menuge J, Hill R. Spherulitic crystallization of apatite–mullite glass-ceramics: mechanisms of formation and implications for fracture properties. *J. Non-Cryst. Solids* 2010;356:1802–13.
- [232] Harizanova R, Wisniewski W, Avdeev G, Rüssel C. Crystallization and growth morphology of barium titanate and fresnoite from a glass with the composition 20.1Na₂O-23.1BaO-23TiO₂-9.8B₂O₃-21SiO₃-3Al₂O₃. *CrystEngComm* 2017;19:6208–14.
- [233] Nan Y, Lee WE, James PF. Crystallization behavior of CaO–P₂O₅ glass with TiO₂, SiO₂, and Al₂O₃ additions. *J. Am. Ceram. Soc.* 1992;75:1641–7.
- [234] Lacerda SR, Oliveira JM, Correia RN, Fernandes MHV. TiO₂ induced phase separation and crystallization in 2SiO₂-3CaO-P₂O₅-MgO glass. *J. Non-Cryst. Solids* 1997;221:255–60.
- [235] Vogel J, Jana C, Hartmann P. Structural investigations of SiO₂-containing phosphate glasses. *Glastech. Ber. Glass Sci. Technol.* 1998;71:97–101.
- [236] Oliveira JM, Correia RN, Fernandes MHV. Formation of convoluted silica precipitates during amorphous phase separation in the Ca₃(PO₄)₂-SiO₂-MgO system. *J. Am. Ceram. Soc.* 2000;83:1296–8.
- [237] Nittmann J, Stanley HE. Tip splitting without interfacial tension and dendritic growth patterns arising from molecular anisotropy. *Nature* 1986;321:663–8.
- [238] Harizanova R, Keding R, Rüssel C. Electric conductivity of glasses in the system Na₂O/CaO/SiO₂/Fe₂O₃. *J. Non-Cryst. Solids* 2008;254:65–71.
- [239] Rettenmayr M. Melting and remelting phenomena. *Int. Mater. Rev.* 2009;54:1–17.
- [240] Langer JS. Instabilities and pattern formation in crystal growth. *Rev. Mod. Phys.* 1980;52:1–30.
- [241] Levi AC, Kotrla M. Theory and simulation of crystal growth. *J. Physics: Cond. Matter* 1997;9:299–344.
- [242] Trivedi R, Kurz W. Dendritic growth. *Inter. Mater. Rev.* 1994;39:49–74.
- [243] Langer JS. Dendrites, viscous fingers, and the theory of pattern formation. *Science* 1989;243:1150–6.
- [244] Wagner FE, Haslbeck S, Stievano L, Calogero S, Pankhurst QA, Martinek K-P. Before striking gold in gold-ruby glass. *Nature* 2000;407:691–2.
- [245] Ruivoa A, Gomes C, Lima A, Botelho ML, Melo R, Belchior A, et al. Gold nanoparticles in ancient and contemporary ruby glass. *J. Cultural Heritage* 2008;9 (Supplement):e134–7.
- [246] Stookey SD. Coloration of glass by gold, silver and copper. *J. Am. Ceram. Soc.* 1949;32:246–9.
- [247] Paje SE, Llopis J, Villegas MA, García MA, Navarro JMF. Thermal effects on optical properties of silver ruby glass. *Appl. Phys. A* 1998;67:429–33.
- [248] Brun N, Mazerolles L, Pernot M. Microstructure of opaque red glass containing copper. *J. Mater. Sci. Lett.* 1991;10:1418–20.

- [249] Sonawane RS, Naik SD, Apte SK, Kulkarni MV, Kale BB. CdS/CdSe quantum dots in glass matrix. *Bull. Mater. Sci.* 2008;31:495–9.
- [250] Apte SK, Kale BB, Sonawane RS, Naik SD, Bodhale SS, Das BK. Homogeneous growth of CdS/CdSe nanoparticles in glass matrix. *Mater. Lett.* 2006;60:499–503.
- [251] Esch V, Fluegel B, Khitrova G, Gibbs HM, Jiajin X, Kang K, et al. State filling, Coulomb, and trapping effects in the optical nonlinearity of CdTe quantum dots in glass. *Phys. Rev. B* 1990;42:7450–3.
- [252] Liu L-C, Kim MJ, Risbudand SH, Carpenter RW. High-resolution electron microscopy and microanalysis of CdS and CdTe quantum dots in glass matrices. *Phil. Mag. B* 1991;63:769–76.
- [253] Tschomsky VA, Dotsenko AV, Glebov LB. Physics and chemistry of photochromic Glasses. (1st ed.). Boca Raton: CRC Press; 1998. 10.1201/9781003067986.
- [254] Pascova R, Gutzow I, Schmelzer J. A model investigation of the process of phase formation in photochromic glasses. *J. Mater. Sci.* 1990;25:921–31.
- [255] Morse DL. Copper halide-containing photochromic glasses. *Inorg. Chem.* 1981;20:777–80.
- [256] Armistead WH, Stookey SD. Photochromic silicate glasses sensitized by silver halides. *Science* 1964;144:150–4.
- [257] Smith G. Photochromic glasses: properties and applications. *J. Mater. Sci.* 1967;2:139–52.
- [258] Smith GP. Photochromic silver halide glasses. *J. Photographic Sci.* 1970;18:41–9.
- [259] Ruppini R. Optical absorption of copper colloids in photochromic glasses. *J. Appl. Phys.* 1986;59:1355–9.
- [260] Kriltz A, Müller M. On-line spectroscopic studies of glasses at high temperatures. *Glastech. Ber. Glass Sci. Technol.* 1994;67C:305–8.
- [261] Kriltz A, Müller M. Spectroscopic investigations of glasses with semiconductor microcrystals at higher temperatures. *Glastech. Ber. Glass Sci. Technol.* 1994;67:343–7.
- [262] Meiwes-Broer KH, Lutz HO. Cluster—zwischen Atom und Festkörper. *Phys. Bl.* 1991;47:283–8.
- [263] Lifshitz IM, Slyozov VV. The kinetics of precipitation from supersaturated solid solutions. *J. Phys. Chem. Solids* 1961;19:35–50.
- [264] Brailford AD, Wynblatt P. The dependence of Ostwald ripening kinetics on particle volume fraction. *Acta Metall.* 1979;27:489–97.
- [265] Hoell A, Varga Z, Raghuwanshi VS, Krumrey M, Bocker C, Rüssel C. ASAXS Study of CaF₂ nanoparticles embedded in a silicate glass matrix. *J. Appl. Cryst.* 2014;47:60–6.
- [266] Raghuwanshi VS, Rüssel C, Hoell A. Crystallization of ZrTiO₄ Nanocrystals in Lithium-alumino-silicate Glass Ceramics: ASAXS Investigation. *Cryst. Growth Des.* 2014;14:2838–45.
- [267] Tang H, Cheng Y, Yuan X, Zhang K, Kurnosov A, Chen Z, et al. Toughening oxide glasses through paracrystallization. *Nat. Mater.* 2023;22:1189–95.
- [268] Zandonà A, Véron E, Helsch G, Canizarès A, Deubener J, Allix M, et al. Crystallization Mechanism of Gel-Derived SiO₂–TiO₂ Amorphous Nanobeads Elucidated by High-Temperature In Situ Experiment. *Cryst. Growth Des.* 2023;23:4545–55.
- [269] Leadbetter AJ, Wright AF. The α – β transition in the cristobalite phases of SiO₂ and AlPO₄ I. X-ray studies. *Phil. Mag.* 1976;33:105–12.
- [270] Schmahll WW, Swaisson IP, Dove MT, Graeme-Barber AZ. Landau free energy and order parameter behaviour of the α/β phase transition in cristobalite. *Z. Kristallogr.* 1992;201:125–45.
- [271] Herrmann A, Simon A, Rüssel C. Preparation and luminescence properties of Eu²⁺-doped BaSi₂O₅ glass-ceramics. *J. Lumin.* 2012;132:215–9.
- [272] Moulton BJ, Silva LD, Sabino SR, Evaristo LL, Sampaio DV, Buchner S, et al. Unusual crystallization pathways revealed in six barium disilicate (BaSi₂O₅) glasses. *Ceram. Int.* 2023;49:10852–63.
- [273] Wisniewski W, Keshavarzi A, Zschechel T, Rüssel C. EBSD-based phase identification in glass-ceramics of the Y-Al-Si-O system containing α - and β -Y₂Si₂O₇. *J. Alloys Compd.* 2017;699:832–40.
- [274] Keshavarzi A, Wisniewski W, de Kloe R, Rüssel C. Surface crystallization of yttrium aluminium garnet from a silicate glass. *CrystEngComm* 2013;15:5425–33.
- [275] Ueno S, Suzuki Y, Furukawa Y, Tada T, Kanno N, Jang BK. Crystallization of glass with Y₂Si₂O₇-mullite eutectic composition. *J. Ceram. Soc. Japan* 2016;124:796–9.
- [276] Ueno S, Tada T, Suzuki Y, Nozawa J, Jang BK, Sekino T. Crystallization and microstructure formation of glass with Y₂Si₂O₇-mullite eutectic composition. *Ceram. Int.* 2016;42:13601–4.
- [277] Wisniewski W, Seidel S, Patzig C, Rüssel C. Surface crystallization of a MgO/Y₂O₃/SiO₂/Al₂O₃/ZrO₂ glass: growth of an oriented β -Y₂Si₂O₇ layer and epitaxial ZrO₂. *Sci. Rep.* 2017;7:44144.
- [278] Courcot E, Rebillat F, Teyssandier F, Louchet-Pouillier C. Thermochemical stability of the Y₂O₃-SiO₂ system. *J. Eur. Ceram. Soc.* 2010;30:905–10.
- [279] Hudon P, Jung I-H, Baker DR. Experimental investigation and optimization of thermodynamic properties and phase diagrams in the systems CaO-SiO₂, MgO-SiO₂, CaMgSi₂O₆-SiO₂ and CaMgSi₂O₆-Mg₂SiO₄ to 1.0 GPa. *J. Petrology* 2005;46:1859–80.
- [280] Zhang R, Mao H, Taskinen P. Thermodynamic descriptions of the BaO-CaO, BaO-SrO, BaO-SiO₂ and SrO-SiO₂ systems. *Calphad* 2016;54:107–16.
- [281] Xinyu Y, Yang L, Songbin L, Di W, Dejian H, Fengli Y. Experimental study and thermodynamic calculation of Lu₂O₃-SiO₂ binary system. *J. Rare Earths* 2017;35:927–33.
- [282] Parker CG, Opila EJ. Stability of the Y₂O₃-SiO₂ system in high-temperature, high-velocity water vapor. *J. Am. Ceram. Soc.* 2020;103:2715–26.
- [283] Christian JW. The Theory of Transformations in Metals and Alloys. Oxford, England: Pergamon Press; 1965. p. 544.
- [284] Uhlmann DR. A Kinetic Treatment of Glass Formation. *J. Non-Cryst. Solids* 1972;7:337–48.
- [285] Weinberg MC. Time-temperature-transformation diagrams with more than one nose. *J. Am. Ceram. Soc.* 1992;75:56–61.
- [286] D. R. Uhlmann, P. I. K. Onorato, G. W. Scherer, A simplified model for glass formation, Lunar and Planetary Science Conference, 10th, Houston, Tex., March 19–23, 1979, Proceedings. Vol. 1, New York, Pergamon Press, Inc., 1979, p. 375–381.
- [287] J. E. Shelby "Introduction to glass science and technology" 2nd Edition, Royal Society of Chemistry, 2005.
- [288] Elliott SR. Medium-range structural order in covalent amorphous solids. *Nature* 1991;354:445–52.
- [289] Buckermann W-A, Müller-Warmuth W, Frischat GH. A further ²⁹Si MAS NMR study on binary alkali silicate glasses. *Glastech. Ber.* 1992;65:18–21.
- [290] Stebbins JF. Effects of temperature and composition on silicate glass structure and dynamics: Si-29 NMR results. *J. Non-Cryst. Solids* 1988;106:359–69.
- [291] Emerson JF, Stallworth PE, Bray PJ. High-field ²⁹Si NMR studies of alkali silicate glasses. *J. Non-Cryst. Solids* 1989;113:253–9.
- [292] Avramov I, Rüssel C, Keding R. Effect of chemical composition on viscosity of oxide glasses. *J. Non-Cryst. Solids* 2003;324:29–35.
- [293] Brady GW. Structure of sodium metaphosphate glass. *J. Chem. Phys.* 1958;28:48–50.
- [294] Velli LL, Varsamis CPE, Kamitsos EI, Möncke D, Ehrh D. Structural investigation of metaphosphate glasses. *Phys. Chem. Glasses* 2005;46:178–81.
- [295] Wasche R, Brückner R. The structure of mixed alkali phosphate melts as indicated by their non-Newtonian flow behavior and optical birefringence. *Phys. Chem. Glasses* 1986;27:87–94.
- [296] Brückner R. Anisotropic glasses and glass melts - A survey. *Glastech. Ber. Glass Sci Technol.* 1996;69:396–411.
- [297] Myers MB, Feltz EJ. Structural characterizations of vitreous inorganic polymers by thermal studies. *Mater. Res. Bull.* 1967;2:535–46.
- [298] Georgiev DG, Boolchand P, Micoulau M. Rigidity transitions and molecular structure of As_xSe_{1-x} glasses. *Phys. Rev. B* 2000;62:9228–31.
- [299] Mauro JC, Varshneya AK. Modeling of rigidity percolation and incipient plasticity in germanium-selenium glasses. *J. Am. Ceram. Soc.* 2007;90:192–8.
- [300] Seddon AB. Chalcogenides: glass-forming systems and progress in application of percolation theory. *J. Non-Cryst. Solids* 213 & 2 1997;214:22–9.
- [301] Varshneya AK. Some comments on physical properties of chalcogenide glasses. *J. Non-Cryst. Solids* 2000;273:1–7.
- [302] Blétry J. Description of the glass transition by a percolation blocking of local chemical order. *Z. Naturforsch.* 1996;51a:87–94.
- [303] Ojovan MI. Ordering and structural changes at the glass-liquid transition. *J. Non-Cryst. Solids* 2013;382:79–86.
- [304] Ojovan MI. The modified random network (MRN) model within the configuron percolation theory (CPT) of glass transition. *Ceramics* 2021;4:121–34.
- [305] Hunt A. Transport in ionic conducting glasses. *J. Phys.: Condens. Matter* 1991;3:7831–42.
- [306] Hunt AG. Fragility of liquids using percolation-based transport theories Correlation between limiting slope of the viscosity and non-exponentiality of relaxation. *J. Non-Cryst. Solids* 2000;274:93–101.
- [307] Ingram MD. A new mechanism for ionic conduction in glass. *Mater. Chem. Phys.* 1989;23:51–61.
- [308] Ingram MD. Ionic conductivity and glass structure. *Phil. Mag. B* 1989;60:729–40.
- [309] Hill R. An alternative view of the degradation of bioglass. *J. Mater. Sci. Lett.* 1996;15:1122–5.
- [310] Hill RG, Brauer DS. Predicting the bioactivity of glasses using the network connectivity or split network models. *J. Non-Cryst. Solids* 2011;357:3884–7.

- [311] Thorpe MF. Continuous deformations in random networks. *J. Non-Cryst. Solids* 1983;57:355–70.
- [312] Phillips JC, Thorpe MF. Constraint theory, vector percolation and glass formation. *Solid State Commun.* 1985;53:699–702.
- [313] Angell CS. Liquid fragility and the glass transition in water and aqueous solutions. *Chem. Rev.* 2002;102:2627–50.
- [314] Vilgis TA. Strong and fragile glasses: A powerful classification and its consequences. *Phys. Rev. B* 1993;47:2882–5.
- [315] Sidebottom DL. Fragility of network-forming glasses: A universal dependence on the topological connectivity. *Phys. Rev. E* 2015;92:062804.
- [316] Avramov I, Keding R, Rüssel C. Crystallization kinetics and rigidity percolation in glass forming melts. *J. Non-Cryst. Solids* 2000;272:147–53.
- [317] de Almeida RPF, Bocker C, Rüssel C. Size of CaF_2 crystals precipitated from glasses in the $\text{Na}_2\text{O}/\text{K}_2\text{O}/\text{CaO}/\text{CaF}_2/\text{Al}_2\text{O}_3/\text{SiO}_2$ -system and percolation theory. *Chem. Mater.* 2008;20:5916–21.
- [318] Lin C, Rüssel C, Dai S. Chalcogenide glass-ceramics: functional design and crystallization mechanism. *Prog. Mater. Sci.* 2018;93:1–44.
- [319] Liu SJ, Fu GZ, Shan ZT, Ren XR, Zhang YF, Zhu CF, et al. Nanocrystal formation and photoluminescence in the $\text{Yb}^{3+}/\text{Er}^{3+}$ codoped phosphosilicate glasses. *J. Non-Cryst. Solids* 2014;383:141–5.
- [320] Liu SJ, Shan ZT, Fu GZ, Yue YZ. Influence of rare earth oxides on the non-isothermal crystallization of phosphosilicate melts during cooling. *J. Non-Cryst. Solids* 2014;385:75–80.
- [321] Liu S, Zhang Y, Yue Y. Effect of Mg–Ca substitution on the spontaneous crystallization behaviour of phospho silicate glasses. *Phys. Chem. Glasses: Eur. J. Glass Sci. Technol. B* 2011;52:85–90.
- [322] Liu SJ, Zhang YF, He W, Yue YZ. Transparent phosphosilicate glasses containing crystals formed during cooling of melts. *J. Non-Cryst. Solids* 2011;357:3897–900.
- [323] Liu S, Kong Y, Tao H, Sang Y. Crystallization of a highly viscous multicomponent silicate glass: Rigidity percolation and evidence of structural heterogeneity. *J. Eur. Ceram. Soc.* 2017;37:715–20.
- [324] Imaoka M, Yamazaki T. Glass formation ranges in ternary systems (Part 1) Silicates of a-group elements. *Report of the Institute of Industrial Science of Tokyo University* 1968;18:241–73.
- [325] Imaoka M. Glass formation of borate systems between a-group elements. *Report of the Institute of Industrial Science of Tokyo University* 1957;6:128–83.
- [326] Imaoka M, Yamazaki T. Studies of the Glass-formation Range of Tellurite Systems. *J. Ceram. Soc. Jpn.* 1968;76:160–72.
- [327] Chen HS, Miller CE. A rapid quenching technique for the preparation of thin uniform films of amorphous solids. *Rev. Sci. Instruments* 1970;41:1237–8.
- [328] Lenarciak A, Wójcik NA, Kupracz P, Strychalska-Nowak J, Sobczak Z, Przeźniak-Welenc M, et al. Thermal, electrical, and magnetic properties of Fe_2O_3 - PbO - SiO_2 glass prepared by traditional melt-quenching and twin roller fast-cooling methods. *J. Phys. Chem. Solids* 2019;135:109010.
- [329] Rindome GE. Further studies of the crystallization of a lithium silicate glass. *J. Am. Ceram. Soc.* 1962;45:7–12.
- [330] Huang WH, Ray CS, Day DE. Dependence of the critical cooling rate for lithium-silicate glass on nucleating agent. *J. Non-Cryst. Solids* 1986;86:204–12.
- [331] Ray CS, Huang W, D. e. Day Crystallization Kinetics of Lithia-Silica Glasses: Effect of Composition and Nucleating Agent. *J. Am. Ceram. Soc.* 1987;70:599–603.
- [332] Narayan KL, Kelton KF, Ray CS. Effect of Pt doping on nucleation and crystallization in Li_2O - 2SiO_2 glass: experimental measurements and computer modeling. *J. Non-Cryst. Solids* 1996;195:148–57.
- [333] Alton J, Plaisted TJ, Hrma P. Kinetics of growth of spinel crystals in a borosilicate glass. *Chem. Eng. Sci.* 2002;57:2503–9.
- [334] Vladislavova L, Kracker M, Zschechel T, Thieme C, Rüssel C. The effect of different platinum concentrations as nucleation agent in the $\text{BaO}/\text{SrO}/\text{ZnO}/\text{SiO}_2$ glass System. *J. Mater. Sci.* 2018;53:11204–15.
- [335] Mishima N, Wakasugi T, Ota R. Nucleation Behavior of Li_2O - Na_2O - SiO_2 Glass Doped with Platinum. *J. Ceram. Soc. Japan* 2004;112:350–3.
- [336] Cronin D, Pye LD. Platinum catalyzed crystallization of Li_2O - 2SiO_2 glass. *J. Non-Cryst. Solids* 1986;84:196–205.
- [337] Negro A, Murat M, Sassi F. Thermal crystallization of cordierite glass powder with platinum as a nucleating agent. *Ceramurgia Int.* 1976;2:131–4.
- [338] Ray CS, Day DE. An Analysis of Nucleation-Rate Type of Curves in Glass as Determined by Differential Thermal Analysis. *J. Am. Ceram. Soc.* 1997;80:3100–8.
- [339] Dobrev A, Gutzow I. Activity of substrates in the catalyzed nucleation of glass-forming melts. II. Experimental evidence. *J. Non-Cryst. Solids* 1993;162:13–25.
- [340] Thieme C, Kracker M, Thieme K, Patzig C, Höche T, Rüssel C. Core-shell structures with metallic silver as nucleation agent of low expansion phases in $\text{BaO}/\text{SrO}/\text{ZnO}/\text{SiO}_2$ glasses. *CrystEngComm* 2019;21:4373–86.
- [341] Szabó I, Frischat GH. Influence of Ag on nucleation and crystallization of fluorozirconate glasses. *J. Non-Cryst. Solids* 1993;161:66–9.
- [342] Bahadur D, Sudhakar N, Sharma SV, Gupta KP, Majumdar AK. Ag_2O as nucleating agent in the crystallization of superconducting phase in $\text{Bi}_2\text{Sr}_2\text{Ca}_4\text{Cu}_5\text{O}_7$ glass composition. *Physica C: Superconductivity* 1992;190:527–36.
- [343] Garai M, Sasmal N, Molla AR, Tarafder A, Karmakar B. Effects of in-situ generated coinage nanometals on crystallization and microstructure of fluorophlogopite mica containing glass-ceramics. *J. Mater. Sci. Technol.* 2015;31:110–9.
- [344] Rüssel C, Freude E. Voltammetric studies of the redox behaviour of various multivalent ions in soda-lime-silica glass melts. *Phys. Chem. Glasses* 1989;30:62–8.
- [345] Williams JA, Rindome GE, McKinsty HA. Small-angle X-ray scattering analysis of nucleation in glass: III, gold ruby glasses. *J. Am. Ceram. Soc.* 1981;64:709–13.
- [346] Simo A, Polte J, Pfänder N, Vainio U, Emmerling F, Rademann K. Formation Mechanism of Silver Nanoparticles Stabilized in Glassy Matrices. *J. Am. Chem. Soc.* 2012;134:18824–33.
- [347] Glebov LB. Kinetics modeling in photosensitive glass. *Opt. Mater.* 2004;25:413–8.
- [348] Glebov LB. Photosensitive holographic glass - new approach to creation of high power lasers. *Phys. Chem. Glasses B* 2007;48:123–8.
- [349] Lumeau J, Glebova L, Glebov LB. Influence of UV-exposure on the crystallization and optical properties of photo-thermo-refractive glass. *J. Non-Cryst. Solids* 2008;354:425–30.
- [350] Stoica M, de Macedo GNB, Rüssel C. Photo induced crystallization of CaF_2 from a $\text{Na}_2\text{O}/\text{K}_2\text{O}/\text{CaO}/\text{CaF}_2/\text{Al}_2\text{O}_3/\text{SiO}_2$ glass. *Opt. Mater. Exp.* 2014;4:1574–85.
- [351] Kleebusch E, Patzig C, Krause M, Hu Y, Höche T, Rüssel C. The effect of TiO_2 on nucleation and crystallization of a Li_2O - Al_2O_3 - SiO_2 glass investigated by XANES and STEM. *Sci. Rep.* 2018;8:2929.
- [352] Hunger A, Carl G, Gebhardt A, Rüssel C. Young's moduli and microhardness of glass-ceramics in the system $\text{MgO}/\text{Al}_2\text{O}_3/\text{TiO}_2/\text{SiO}_2$ containing quartz nano crystals. *Mater. Chem. Phys.* 2010;122:502–6.
- [353] Rezvanian M, Eftekhari-Yekta B, Solati-Hashjin M, Marghussian VK. Effect of Cr_2O_3 , Fe_2O_3 and TiO_2 nucleants on the crystallization behaviour of SiO_2 - Al_2O_3 - CaO - MgO (R_2O) glass-ceramics. *Ceram. Inter.* 2005;31:75–80.
- [354] Khater GA. Influence of Cr_2O_3 , LiF , CaF_2 and TiO_2 nucleants on the crystallization behavior and microstructure of glass-ceramics based on blast-furnace slag. *Ceram. Inter.* 2011;37:2193–9.
- [355] Rezvani M. The effect of Y_2O_3 , CeO_2 , P_2O_5 , ZrO_2 and TiO_2 in single, double and triple form on crystallization mechanism of Li_2O - Al_2O_3 - SiO_2 (LAS). *Iranian J. Mater. Sci. & Engin.* 2011;8:41–9.
- [356] Morimoto S, Kuriyam N. Effect of TiO_2 , ZrO_2 and P_2O_5 on the Crystallization of SiO_2 - Al_2O_3 - MgO - CaO - Na_2O Glass System. *J. Ceram. Soc. Japan* 1996;104:466–8.
- [357] Reben M, Kosmal M, Ziabka M, Pichniarczyk P, Grelowska I. The influence of TiO_2 and ZrO_2 on microstructure and crystallization behavior of CRT glass. *J. Non-Cryst. Solids* 2015;425:118–23.
- [358] Rao AS, Ashok J, Suresh B, Raju GN, Venkatramaiah N, Kumar VR, et al. Physical characteristics of PbO - ZrO_2 - SiO_2 - TiO_2 glass-ceramics embedded with $\text{Pb}_2\text{Ti}_2\text{O}_6$ cubic pyrochlore crystal phase: Part-I electrical properties. *J. Alloys Comp.* 2017;712:672–86.
- [359] Mirhadi B, Mehdikhani B. The Effect of compositional changes on the crystallization behaviour and mechanical properties of Li_2O - CaO - SiO_2 - Al_2O_3 . *Adv. Mater. Sci.* 2011;11:11–21.
- [360] Zdaniewski W. DTA and X-ray analysis study of nucleation and crystallization of MgO - Al_2O_3 - SiO_2 glasses containing ZrO_2 , TiO_2 , and CeO_2 . *J. Am. Ceram. Soc.* 1975;58:163–9.
- [361] Lembke U, Brückner R, Kranold R, Höche Th. Phase formation kinetics in a glass ceramic studied by small-angle scattering of X-rays and neutrons and by visible-light scattering. *J. Appl. Cryst.* 1997;30:1056–64.
- [362] Guignard M, Cormier L, Montouillout V, Menguy N, Massiot D, Hannon AC. Environment of titanium and aluminum in a magnesium aluminosilicate glass. *J. Phys.: Condens. Matter* 2009;21:375107.

- [363] Guignard M, Cormier L, Montouillout V, Menguy N, Massiot D, Hannon AC, et al. Rearrangement of the structure during nucleation of a cordierite glass doped with TiO_2 . *J. Phys.: Condens. Matter* 2010;22:185401.
- [364] Dutkiewicz J, Stoch L, Morgiel J, Kistorz G, Stoch P. Analytical and HREM study of the early stages of $\text{SiO}_2\text{-Al}_2\text{O}_3\text{-(Mg, Zn)O}$ glass crystallisation. *Mater. Chem. Phys.* 2003;81:411–3.
- [365] Golubkov VV, Dymshits OS, Zhilin AA, Chuvaeva TI, Shashkin AV. On the phase separation and crystallization of glasses in the $\text{MgO-Al}_2\text{O}_3\text{-SiO}_2\text{-TiO}_2$ system. *Glass Phys. Chem.* 2003;29:254–66.
- [366] Guignard M, Cormier L, Montouillout V, Menguy N, Massiot D. Structural fluctuations and role of Ti as nucleating agent in an aluminosilicate glass. *J. Non-Cryst. Solids* 2010;356:1368–73.
- [367] Li H, Liu L, Tang X, Wang Q, Xiong D. Preparation and luminescent properties of Tb^{3+} -doped $\text{SrO-Al}_2\text{O}_3\text{-SiO}_2$ glass-ceramics for white light-emitting diode. *Glass Phys. Chem.* 2005;12:507–10.
- [368] Loiko PA, Dymshits OS, Zhilin AA, Alekseeva IP, Yumashev KV. Influence of NiO on phase transformations and optical properties of $\text{ZnO-Al}_2\text{O}_3\text{-SiO}_2$ glass-ceramics nucleated by TiO_2 and ZrO_2 . Part II. Optical absorption and luminescence. *J. Non-Cryst. Solids* 2013;376:99–105.
- [369] Back G-S, Yoon M-J, Jung W-G. Effect of the Cr_2O_3 and TiO_2 as nucleating agents in $\text{SiO}_2\text{-Al}_2\text{O}_3\text{-CaO-MgO}$ glass-ceramic system. *Met. Mater. Int.* 2017;23:798–804.
- [370] de Borja CDG, Morais DS, Riella HG. Crystallization of the nepheline phase in $\text{Na}_2\text{O-K}_2\text{O-Al}_2\text{O}_3\text{-SiO}_2$ glasses by addition of nucleating agents. *Key Engin. Mater.* 2002;230–232:72–5.
- [371] Lahl N, Singh K, Singheiser L, Hilpert K. Crystallisation kinetics in $\text{AO-Al}_2\text{O}_3\text{-SiO}_2\text{-B}_2\text{O}_3$ glasses ($A = \text{Ba, Ca, Mg}$). *J. Mater. Sci.* 2000;35:3089–96.
- [372] Li-Ping Y, Han-Ning X, Peng-Fei H. Effect of nucleating agents on microstructure and mechanical properties of $\text{SiO}_2\text{-Al}_2\text{O}_3\text{-ZrO}_2$ glass-ceramics. *J. Cent. South Univ. Technol.* 2005;12:507–10.
- [373] Tauch D, Rüssel C. Glass-ceramics in the system $\text{BaO/TiO}_2(\text{ZrO}_2)/\text{Al}_2\text{O}_3/\text{B}_2\text{O}_3$ and their thermal expansion. *J. Non-Cryst. Solids* 2007;353:2109–14.
- [374] Cheng K, Wan J, Liang K. Differential thermal analysis on the crystallization kinetics of $\text{K}_2\text{O-B}_2\text{O}_3\text{-MgO-Al}_2\text{O}_3\text{-SiO}_2\text{-TiO}_2\text{-F}$ Glass. *J. Am. Ceram. Soc.* 1999;82:1212–6.
- [375] M. Garai, TiO_2 and ZrO_2 controlled crystallization and microstructure in $\text{SiO}_2\text{-MgO-Al}_2\text{O}_3\text{-B}_2\text{O}_3\text{-K}_2\text{O-F}$ glass. Materials Science and Technology 2017 (MS&T17), October 8 – 12, 2017, David L. Lawrence Convention Center, Pittsburgh, Pennsylvania USA, DOI 10.7449/2017/MST.2017.960.967.
- [376] Öztürk A. Microstructure and indentation fracture toughness of mica glass-ceramics. *Int. J. Microstruct. Mater. Properties* 2008;3:780–90.
- [377] Mollazadeh S, Yekta BE, Javadpour J, Yusefi A, Jafarzadeh TS. The role of TiO_2 , ZrO_2 , BaO and SiO_2 on the mechanical properties and crystallization behavior of fluorapatite-mullite glass-ceramics. *J. Non-Cryst. Solids* 2013;361:70–7.
- [378] Dittmer M, Yamamoto CF, Bocker C, Rüssel C. The effect of yttria on the crystallization and mechanical properties of $\text{MgO/Al}_2\text{O}_3/\text{SiO}_2/\text{ZrO}_2$ glass-ceramics. *Solid State Sci.* 2011;13:2146–53.
- [379] Gawronski A, Rüssel C. High strength glass-ceramics in the system $\text{MgO/Y}_2\text{O}_3/\text{Al}_2\text{O}_3/\text{SiO}_2/\text{ZrO}_2$. *J. Mater. Sci.* 2013;38:3461–8.
- [380] Hsiang H-I, Yung S-W, Wang C-C. Crystallization, densification and dielectric properties of $\text{CaO-MgO-Al}_2\text{O}_3\text{-SiO}_2$ glass with ZrO_2 as nucleating agent. *Mater. Res. Bull.* 2014;60:730–7.
- [381] Baldi G, Generali E, Leonelli C, Manfredini T, Pellacani GC, Siligardi C. Effects of nucleating agents on diopside crystallization in new glass-ceramics for tile-glaze application. *J. Mater. Sci.* 1995;30:3251–5.
- [382] Kleebusch E, Patzig C, Höche T, Rüssel C. Phase formation during crystallization of a $\text{Li}_2\text{O-Al}_2\text{O}_3\text{-SiO}_2$ glass with ZrO_2 as nucleating agent-an X-ray diffraction and (S)TEM study. *Ceram. Int.* 2017;43:9769–77.
- [383] Fernandes HR, Tulyaganov DU, Ferreira JMF. The role of P_2O_5 , TiO_2 and ZrO_2 as nucleating agents on microstructure and crystallization behaviour of lithium disilicate-based glass. *J. Mater. Sci.* 2013;48:765–73.
- [384] Krüger S, Deubener J, Ritzberger C, Höland W. Nucleation kinetics of lithium metasilicate in ZrO_2 -bearing lithium disilicate glasses for dental application. *Int. J. Appl. Glass Sci.* 2013;4:9–19.
- [385] Lin C-C, Shen P, Chang HM, Yang YJ. Composition dependent structure and elasticity of lithium silicate glasses: Effect of ZrO_2 additive and the combination of alkali silicate glasses. *J. Eur. Ceram. Soc.* 2006;26:3613–20.
- [386] Meechoowas E, Suriyoporn S, Pantulap U, Tapasa K. The effect of zirconium oxide on properties and crystallization of soda-lime silicate glass. *Key Engin. Mater.* 2017;751:374–8.
- [387] Chen B, Han N, Cao X, Guo Y, Liu C. Microstructure and crystallization properties of $\text{Na}_2\text{O-CaO-SiO}_2$ glass system with different ZrO_2 content. *J. Non-Cryst. Solids* 2021;573:121137.
- [388] Kamonlert A, Niyompan A, Tipakontitkul R. Effect of ZrO_2 addition on crystallization and properties of the glass-ceramics contained NaNbO_3 crystals. *Curr. Appl. Phys.* 2011;11:1100–5.
- [389] Patzig C, Höche T, Dittmer M, Rüssel C. Temporal evolution of crystallization in $\text{MgO/Al}_2\text{O}_3/\text{SiO}_2/\text{ZrO}_2$ glass-ceramics. *Cryst. Growth Des.* 2012;12:2059–67.
- [390] Seidel S, Patzig C, Höche T, Krause M, Ebert M, Hu Y, et al. The crystallization of $\text{MgO-Al}_2\text{O}_3\text{-SiO}_2\text{-ZrO}_2$ Glass-ceramics with and without addition of Y_2O_3 – a combined STEM/XANES study. *RSC Adv.* 2016;6:62934–43.
- [391] Vomacka P, Babushkin O, Warren R. Zirconia as a nucleating agent in a yttria-alumina-silica glass. *J. Eur. Ceram. Soc.* 1995;15:1111–7.
- [392] Vladislavova L, Thieme C, Rüssel C. The Effect of ZrO_2 on the crystallization of a glass in the system BaO/SrO/ZnO/SiO_2 - surface via bulk crystallization. *J. Mater. Sci.* 2017;52:4052–60.
- [393] Liu X, Pu Y, Li P, Wu T, Gao P. Influence of different nucleating agent additives on phase structure and ferroelectric properties of $\text{SrO-BaO-Nb}_2\text{O}_5\text{-CaO-SiO}_2\text{-B}_2\text{O}_3$ glass-ceramics. *J. Mater. Sci.: Mater. Electron.* 2014;25:3044–51.
- [394] Dargaud O, Cormier L, Menguy N, Galois L, Calas G, Papin S, et al. Structural role of Zr^{4+} as a nucleating agent in a $\text{MgO-Al}_2\text{O}_3\text{-SiO}_2$ glass-ceramics: A combined XAS and HRTEM approach. *J. Non-Cryst. Solids* 2010;356:2928–34.
- [395] Thieme C, Thieme K, Kracker M, Höche T, Rüssel C. Role of tin oxide as a nucleating agent with low solubility in BaO-SrO-ZnO-SiO_2 glasses studied by electron- and X-ray microscopy. *Cryst. Growth Des.* 2019;19:1815–24.
- [396] Dressler M, Rüdinger B, Deubener J. Crystallization kinetics in a lithium aluminosilicate glass using SnO_2 and ZrO_2 additives. *J. Non-Cryst. Solids* 2014;389:60–5.
- [397] Rincón-Mora B, Jordan MM, Ma J, Rincón, Chromium oxide additions in lithium disilicate glass crystallization. *Mater. Lett.* 2016;179:138–41.
- [398] Mirhadi B, Mehdikhani B. Crystallization behavior and microstructure of $(\text{CaO-ZrO}_2\text{-SiO}_2)\text{-Cr}_2\text{O}_3$ based glasses. *J. Non-Cryst. Solids* 2011;357:3711–6.
- [399] Kumara GR, Rao MC. Structural and photoluminescence investigations of Cr^{3+} mixed $\text{Li}_2\text{O-Bi}_2\text{O}_3\text{-ZrO}_2\text{-SiO}_2$ glass-ceramics for optoelectronic device application. *Optik – Inter. J. Light Electron. Optics* 2019;181:721–31.
- [400] Shi Y, Li B-W, Zhao M, Zhang M-X. Growth of diopside crystals in CMAS glass-ceramics using Cr_2O_3 as a nucleating agent. *J. Am. Ceram. Soc.* 2018;101:3968–78.
- [401] Kleebusch E, Patzig C, Höche T, Rüssel C. Effect of the concentration of nucleating agents ZrO_2 and TiO_2 on the crystallization of $\text{Li}_2\text{O-Al}_2\text{O}_3\text{-SiO}_2$ glass- an X-ray diffraction and TEM investigation. *J. Mater. Sci.* 2016;51:10127–38.
- [402] Bhattachaya S, Höche T, Linschek I, Avramov I, Wurth R, Müller M, et al. Direct evidence of Al-rich layers around nanosized ZrTiO_4 in glass: putting the role of nucleation agents in perspective. *Cryst. Growth Design* 2010;10:379–85.
- [403] Pércio MF, de Campos SD, Schneider R, de Campos EA. Effect of the addition of TiO_2 , ZrO_2 , V_2O_5 and Nb_2O_5 on the stability parameters of the $\text{Li}_2\text{O-BaO-SiO}_2$ glass. *J. Non-Cryst. Solids* 2015;411:125–31.
- [404] Wang P, Yu L, Xiao H, Cheng Y, Lian S. Influence of nucleation agents on crystallization and machinability of mica glass-ceramics. *Ceram. Int.* 2009;35:2633–8.
- [405] Benitez T, Veber A, Furlan KP, Rebouças LB, de Ligny D, Hotza D, et al. Development of magnesium-aluminum-silicate glass-ceramics nucleated with Nb_2O_5 . *Int. J. Appl. Glass Sci.* 2020;11:155–69.
- [406] Li Y, Liang K, Xu B, Cao JW. Crystallization mechanism and microstructure evolution of $\text{Li}_2\text{O-Al}_2\text{O}_3\text{-SiO}_2$ glass-ceramics with Ta_2O_5 as nucleating agent. *J. Therm. Anal. Calorim.* 2010;101:941–8.

- [407] Luo Z, Zhou J, Li J, Zhang C, Lu A. Effects of MO (M = Mg, Ca, Ba) on crystallization and flexural strength of semi-transparent lithium disilicate glass-ceramics. *Bull. Mater. Sci.* 2011;34:1511–6.
- [408] Hing P, McMillan PW. A transmission electron microscope, study of glass-ceramics. *J. Mater. Sci.* 1973;8:340–8.
- [409] Montazerian M, Zanotto ED. Tough, strong, hard, and chemically durable enstatite-zirconia glass-ceramic. *J. Am. Ceram. Soc.* 2020;103:5036–49.
- [410] Chakrabarti A, Molla AR. BaBi₂Ta₂O₉ based glass-ceramics: Influence of ZrO₂ on crystallization kinetics, microstructure and dielectric properties. *J. Alloys Comp.* 2019;805:247–57.
- [411] He D, Zhong H, Gao C. Characteristics and dielectric properties of ZrO₂-doped calcium borosilicate glass-ceramics. *Mater. Res. Bull.* 2020;123:110703.
- [412] Mirkazemi SM, Beitollah A, Marghussian VK. Microstructural and magnetic properties of BaO-Fe₂O₃-B₂O₃-SiO₂ glass ceramic with ZrO₂ as nucleating agent. *Phys. Stat. Sol. (C)* 2004;12:3216–26.
- [413] Mirkazemi M, Marghussian VK, Beitollahi A, Dou SX, Wexler D, Konstantinov K. Effect of ZrO₂ nucleant on crystallisation behaviour, microstructure and magnetic properties of BaO-Fe₂O₃-B₂O₃-SiO₂ glass-ceramics. *Ceram. Inter.* 2007;33:463–9.
- [414] Kleebusch E, Patzig C, Krause M, Hu Y, Höche T, Rüssel C. The Formation of Nanocrystalline ZrO₂ Nuclei in a Li₂O-Al₂O₃-SiO₂ Glass- a Combined XANES and TEM Study. *Sci. Rep.* 2017;7:10869.
- [415] Kleebusch E, Patzig C, Höche T, Rüssel C. The Evidence of Phase Separation Droplets in the Crystallization Process of a Li₂O-Al₂O₃-SiO₂ Glass with TiO₂ as Nucleation Agent – An X-ray Diffraction and (S)TEM Study Supported by EDX Analysis. *Ceram. Int.* 2018;44:2919–26.
- [416] Höche T, Mäder M, Bhattacharyya S, Henderson GS, Gemming T, Wurth R, et al. ZrTiO₄ crystallization in nanosized liquid-liquid phase – separation droplets in glass – a quantitative XANES study. *CrystEngComm* 2011;13:2550–6.
- [417] Dugué A, Dymshits O, Cormier L, Cochain B, Lelong G, Zhilin A, et al. In situ evolution of Ni environment in magnesium aluminosilicate glasses and glass-ceramics–Influence of ZrO₂ and TiO₂ nucleating agents. *J. Phys. Chem. Solids* 2015;78:137–46.
- [418] Hunger A, Carl G, Gebhardt A, Rüssel C. Ultra-high thermal expansion glass-ceramics in the system MgO/Al₂O₃/TiO₂/ZrO₂/SiO₂. *J. Non-Cryst. Solids* 2008;354:5402–7.
- [419] Huang J, Zhang J, Yu Y, Bai H, Zhang Z, Huang Y. Transparent MgO-Al₂O₃-SiO₂ glass-ceramics prepared with ZrO₂ and SnO₂ as nucleating agents. *J. Non-Cryst. Solids* 2022;588:121585.
- [420] Shyua J-J, Mai H-C. ZrO₂-nucleated calcium aluminate glass-ceramics with mid-infrared transparency. *J. Mater. Res.* 2006;21:465–72.
- [421] Hunger A, Carl G, Rüssel C. Crystallization of ZnO/MgO/Al₂O₃/TiO₂/ZrO₂/SiO₂-glasses. *Solid State Sci.* 2010;12:1570–4.
- [422] Vladislavova L, Kracker M, Zschechel T, Thieme C, Rüssel C. Crystallization of Ba_{1-x}Sr_xZn₂Si₂O₇ from BaO/SrO/ZnO/SiO₂ glass with different ZrO₂ and TiO₂ concentrations. *Solid State Sci.* 2018;78:107–15.
- [423] Callejas P, Barba MF, Rincon JM. The effect of TiO₂, ZrO₂ and MgO additions on the crystallization of glasses obtained from muscovite and amblygonite. *J. Mater. Sci. Lett.* 1985;4:1171–3.
- [424] Zheng X, Wen G, Song L, Huang XX. Effects of P₂O₅ and heat treatment on crystallization and microstructure in lithium disilicate glass ceramics. *Acta Mater.* 2008;56:549–58.
- [425] Gaddam A, Fernandes HR, Tulyaganov DU, Ribeiro MJ, Ferreira JM. The roles of P₂O₅ and SiO₂/Li₂O ratio on the network structure and crystallization kinetics of non-stoichiometric lithium disilicate based glasses. *J. Non-Cryst. Solids* 2018;481:512–21.
- [426] Hallmann L, Ulmer P, Gerngross M-D, Jetter J, Mintrone M, Lehmann F, et al. Properties of hot-pressed lithium silicate glass-ceramics. *Dental Mater.* 2019;35:713–29.
- [427] Dittmer M, Müller M, Rüssel C. Self organized nano crystallinity in MgO-Al₂O₃-SiO₂ glasses with ZrO₂ as nucleating agent. *Mater. Chem. Phys.* 2010;124:1083–8.
- [428] Deubener J, Zandonà A, Helsch G. Nomenclature of functional crystals in glass-ceramics: A recommendation based on aluminosilicate solid solutions. *J. Non-Cryst. Solids* 2024;633:122954.
- [429] Xu H, Lü X, Heaney PJ, Ren Y. Structural behavior of a stuffed derivative of α -quartz, Mg_{0.5}AlSiO₄. *Phys. Chem. Mineral.* 2019;46:717–25.
- [430] Xu H, Heaney PJ, Yu P, H. Xu, Synthesis and structure of a stuffed derivative of α -quartz, Mg_{0.5}AlSiO₄. *Am. Mineral.* 2015;100:2191–8.
- [431] Zandonà A, Patzig C, Rüdinger B, Hochrein O, Deubener J. TiO₂(B) nanocrystals in Ti-doped lithium aluminosilicate glasses. *J. Non-Cryst. Solids* 2019;2:100025.
- [432] Siebert H, Schleier P, Beinemann J, Fried W, Zenk W, Schumann D. Evaluation of individual ceramic implants made of Bioverit with CAD/CAM technology to reconstruct multidimensional craniofacial defects of the human skull. *Mund-, Kiefer- und Gesichtschirurgie* 2006;10:185–91.
- [433] Vogel W, Höland W. Development, structure, properties and application of glass-ceramics for medicine. *J. Non-Cryst. Solids* 1990;123:349–53.
- [434] Vogel W, Höland W. The development of bioglass ceramics for medical applications. *Angew. Chemie Int. Edition* 1987;26:527–44.
- [435] Stefančić G, Musić S, Ivanda M. Thermal behavior of the amorphous precursors of the ZrO₂-SnO₂ system. *Mater. Res. Bull.* 2008;43:2855–71.
- [436] Kido L, Müller M, Rüssel C. Redox Reactions Occurring During Temperature Change in Soda-Lime-Silicate Melts Doped with Copper, Tin and Antimony or Copper and Tin. *Phys. Chem. Glasses* 2004;45:21–6.
- [437] Höche T. Crystallization in glass: elucidating a realm of diversity by transmission electron microscopy. *J. Mater. Sci.* 2010;45:3683–96.
- [438] Bischoff JL. Kinetics of calcite nucleation: Magnesium ion inhibition and ionic strength catalysis. *J. Geophys. Res.* 1968;73:3315–22.
- [439] Yang J, Tohidi B. Characterization of inhibition mechanisms of kinetic hydrate inhibitors using ultrasonic test technique. *Chem. Engin. Sci.* 2011;66:278–83.
- [440] Jean JH, Gupta TK. Devitrification inhibitors in borosilicate glass and binary borosilicate glass composite. *J. Mater. Res.* 1995;10:1312–20.
- [441] Jean JH, Gupta TK. Alumina as a devitrification inhibitor during sintering of borosilicate glass powders. *J. Am. Ceram. Soc.* 1993;76:2010–6.
- [442] Thieme K, Rüssel C. Nucleation inhibitors- the effect of small concentrations of Al₂O₃, La₂O₃ or TiO₂ on nucleation and crystallization of lithium disilicate. *J. Eur. Ceram. Soc.* 2014;34:3969–79.
- [443] Thieme K, Rüssel C. Nucleation and growth kinetics and phase analysis in zirconia containing lithium disilicate glass. *J. Mater. Sci.* 2015;50:1488–94.
- [444] Thieme K, Rüssel C. The effect of niobium and tantalum oxide on nucleation and growth kinetics in lithium disilicate glasses. *Mater. Chem. Phys.* 2015;162:354–63.
- [445] Thieme K, Avramov J, Rüssel C. The mechanism of deceleration of nucleation and crystal growth by a small addition of transition metals- illustrated for Nb₂O₅ and Ta₂O₅ doped lithium silicate glasses. *Sci. Rep.* 2016;6:25451.
- [446] Thieme K, Rüssel C. CeO₂ and Y₂O₃ as nucleation inhibitors in lithium disilicate glasses. *J. Mater. Sci.* 2016;51:989–99.
- [447] Morey GW. The effect of alumina on the devitrification of a soda-lime-silica glass. *J. Am. Ceram. Soc.* 1930;13:718–23.
- [448] Smiljanić S, Hribar U, Spreitzer M, König J. Influence of additives on the crystallization and thermal conductivity of container glass cullet for foamed glass preparation. *Ceram. Int.* 2021;47:32867–73.
- [449] Wang M, Fang L, Li M, Liu Z, Hu Y, Zhang X, et al. Phase separation and crystallization of La₂O₃ doped ZnO-B₂O₃-SiO₂ glass. *J. Rare Earths* 2019;37:767–72.
- [450] Wang M-T, Fang L, Li M, Liu Z-G, Hu Y-H, Zhang X-W. Effect of rare earth dopant on thermal stability and structure of ZnO-B₂O₃-SiO₂ glass. *J. Inorg. Mater.* 2017;32:643–8.
- [451] Zhao H, Zhang J, Chen H, Liang T, Wei M. The effects of La₂O₃ doping on the photosensitivity, crystallization behavior and dielectric properties of Li₂O-Al₂O₃-SiO₂ photostructural glass. *Ceram. Inter.* 2018;44:20821–6.
- [452] Braun M, Yue Y, Rüssel C, Jäger C. 2D-NMR evidence for local structural order in extruded phosphate glasses. *J. Non-Cryst. Solids* 1998;241:204–7.
- [453] Islam MT, Sharmin N, Rance GA, Titman JJ, Parsons AJ, Hossain KMZ, et al. The effect of MgO/TiO₂ on structural and crystallization behavior of near invert phosphate-based glasses. *J. Biomed. Mater. Res. B: Appl. Biomater.* 2020;108:674–86.
- [454] Liao M, Sun H, Wen L, Fang Y, Hu L. Effect of alkali and alkaline earth fluoride introduction on thermal stability and structure of fluorophosphate glasses. *Mater. Chem. Phys.* 2006;98:154–8.
- [455] Kimata M. Crystallo-chemical evolution of a crystal structure due to cationic substitution after the example of melilite. *Naturwissenschaften* 1985;72:372–3.
- [456] Fokin VM, Reis RM, Abyzov AS, Chinaglia CR, Zanotto ED. Nonstoichiometric crystallization of lithium metasilicate–calcium metasilicate glasses. Part 1—Crystal nucleation and growth rates. *J. Non-Cryst. Solids* 2013;362:56–64.

- [457] Kerstan M, Rüssel C. Barium silicates as high thermal expansion seals for solid oxide fuel Cells Studied by High Temperature X-Ray Diffraction (HT-XRD). *J. Power Sources* 2011;196:7578–84.
- [458] Zhenguo Y, Meinhardt KD, Stevenson JW. Chemical compatibility of barium-calcium-aluminosilicate-based sealing glasses with the ferritic stainless steel interconnect in SOFCs. *J. Electrochem. Soc.* 2003;150:A1095.
- [459] Pascual MJ, Guillet A, Durán A. Optimization of glass–ceramic sealant compositions in the system MgO–BaO–SiO₂ for solid oxide fuel cells (SOFC). *J. Power Sources* 2007;169:40–6.
- [460] Thieme C, Rüssel C. Interfacial reactions between a crystallizing sealing glass from the system BaO–ZnO–NiO–SiO₂ and Crofer 22 APU. *J. Mater. Sci.* 2016;51:756–65.
- [461] Thieme C, Rüssel C. High thermal expansion in the solid solution series BaM_{2-x}Ni_xSi₂O₇ (M=Zn, Mg, Co)–the effect of Ni-concentration on phase transition and expansion. *J. Mater. Sci.* 2015;50:3416–24.
- [462] Thieme C, Rüssel C. Thermal expansion behaviour in the solid solution series BaMg_{2-x}Co_xSi₂O₇ (0 ≤ x ≤ 2), studied by dilatometry and in situ high temperature X-ray diffraction. *Thermochim. Acta* 2015;612:49–54.
- [463] Mazurin OV, Porai-Koshits EA, Andreev NS. Phase Separation in Glass. North-Holland, Amsterdam, New York; North Holland; 1984.
- [464] Janowski F, Heyer W. Poröse Gläser: Herstellung. Leipzig: Eigenschaften und Anwendung; VEB Deutscher Verlag für Grundstoffindustrie; 1982.
- [465] Zhu D, Ray CS, Luo F, Zhou W, Day DE. Melting and phase-separation of lead borate glasses in low gravity drop shaft. *Ceram. Inter.* 2008;34:417–20.
- [466] Reiß H. Effect of different gravity conditions on microstructure of glass melts in a stable miscibility gap. *Glastech. Ber. Glass Sci. Technol.* 1998;71:300–6.
- [467] Häbßer J, Rüssel C. Effect of microstructure of a phase separated sodium-borosilicate glass on mechanical properties. *Ceram. Int.* 2017;43:11403–9.
- [468] Flügel A, Rüssel C. Kinetics of phase separation in a 6.5 Na₂O–33.5 B₂O₃–60 SiO₂ glass. *Glastech. Ber. Glass Sci. Technol.* 2000;73:73–8.
- [469] Skatulla W, Vogel W, Wessel H. Phase Separation and Boron Anomaly in Simple Sodium Borate and Technical Alkali-Borosilicate Glasses. *Silikattechnik* 1958;9:51–62.
- [470] Kühne K. Eigenschaften und Struktur ultra-mikroporöser Gläser. *Z. Phys. Chem.* 1955;204:20–42.
- [471] Porai-Koshits EA, Averbach VI. Primary and secondary phase separation of sodium silicate glasses. *J. Non-Cryst. Solids* 1968;1:29–38.
- [472] Vogel W, Schmidt W, Horn L. Die mehrphasige Struktur von Bariumborosilicatgläsern als Folge einer stufenförmig ablaufenden Phasentrennung. *Z. Chem.* 1969;9:401–10.
- [473] Bocker C, Rüssel C. Percolation, phase separation and crystallization. *Phys. Chem. Glasses Glass Sci. Technol. B* 2017;58:133–41.
- [474] Haller W, Blackburn DH, Wagstaff FE, Charles RJ. Metastable Immiscibility Surface in the System Na₂O–B₂O₃–SiO₂. *J. Am. Ceram. Soc.* 1970;53:34–9.
- [475] Häbßer J, Rüssel C. Self organized growth of sodium-borate-rich droplets in a phase separated sodium-borosilicate glass. *Int. J. Appl. Glass Sci.* 2017;8:124–31.
- [476] Avramov J, Bocker C, Rüssel C. Topology and numerical simulation of phase separation in sodium silicate glass. *J. Phys. Chem. Solids*. 2015;78:8–11.
- [477] Kima SS, Sanders jr TH. Calculation of subliquidus miscibility gaps in the Li₂O–B₂O₃–SiO₂ system. *Ceram. Int.* 2000;26:769–78.
- [478] Du W-F, Kuraoka K, Akai T, Yazawa T. Study of Al₂O₃ effect on structural change and phase separation in Na₂O–B₂O₃–SiO₂ glass by NMR. *J. Mater. Sci.* 2000;35:4865–71.
- [479] Nordberg ME. Properties of some Vycor brand glasses. *J. Am. Ceram. Soc.* 1944;27:299–305.
- [480] James PF. Liquid-phase separation in glass-forming systems. *J. Mater. Sci.* 1975;10:1802–25.
- [481] Taylor P, Owen DG. Liquid immiscibility in the system K₂O–B₂O₃–SiO₂. *J. Am. Ceram. Soc.* 1981;64:C-158-C-159.
- [482] Nuzhnyy D, Vanek P, Petzelt J, Bovtun V, Kempa M, Gregora I, et al. Properties of BaTiO₃ confined in nanoporous Vycor and artificial opal silica. *Proc. Appl. Ceram.* 2010;4:215–23.
- [483] Prapitpongwanich P, Pengpat K, Rüssel C. Phase Separation and Crystallization in LiNbO₃/SiO₂ Glasses. *Mater. Chem. Phys.* 2009;113:913–8.
- [484] Tomozawa M. Liquid phase separation and crystal nucleation in Li₂O–SiO₂ glasses. *Phys. Chem. Glasses* 1972;14:161–6.
- [485] Tomozawa M. Liquid-phase separation and crystal growth in Li₂O–SiO₂ glass. *Phys. Chem. Glasses* 1973;14:112–3.
- [486] Cahn JW. The metastable liquidus and its effect on the crystallization of glass. *J. Am. Ceram. Soc.* 1969;52:118–21.
- [487] Sycheva GA. Nucleation and crystal growth in phase separated glasses in the lithium silicate system. In: Borisenko E, editor. Crystallization and materials science of modern artificial and natural crystals. Rijeka, Croatia: InTech; 2012. p. 23–48.
- [488] Craievich AF, Zanotto ED, James PF. Kinetics of sub-liquidus phase separation in silicate and borate glasses. A review. *Bull. Soc. Fr. Minéral. Cristallogr.* 1983;106:169–84.
- [489] Kalinina AM, Filipovich VN, Kolesova NA. Crystallisation products of lithium silicate glasses, The structure of glass 3. Boston, MA: Springer; 1964. p. 53–65.
- [490] Sycheva GA. Crystal growth and nucleation in glasses in the lithium silicate system. *J. Cryst. Process Technol.* 2016;6:29–55.
- [491] Jana C, Höland W. Formation and properties of a new apatite-containing glass ceramic. *Silic. Ind.* 1991;56:215–8.
- [492] Oliveira JM, Correia RN, Fernandes MH. Effect of SiO₂ on amorphous phase separation of CaO–P₂O₅–SiO₂–MgO glasses. *J. Non-Cryst. Solids* 2000;273:59–63.
- [493] Hill R, Calver A, Stamboulis A, Bub N. Real-Time Nucleation and Crystallization Studies of a Fluorapatite Glass–Ceramics Using Small-Angle Neutron Scattering and Neutron Diffraction. *J. Am. Ceram. Soc.* 2007;90:763–8.
- [494] Chen D, Wan Z, Zhou Y, Chen Y, Yu H, Lu H, et al. Lanthanide-activated Na₅GdF₃ nanocrystals precipitated from a borosilicate glass: phase-separation-controlled crystallization and optical property. *J. Alloys Comp.* 2015;625:149–57.
- [495] Chen D, Wan Z, Zhou Y, Huang P, Zhong J, Ding M, et al. Bulk glass ceramics containing Yb³⁺/Er³⁺: β-NaGdF₄ nanocrystals: Phase-separation-controlled crystallization, optical spectroscopy and unconverted temperature sensing behaviour. *J. Alloys Comp.* 2015;638:21–8.
- [496] Bocker C, Wiemert J, Rüssel C. The Formation of strontium fluoride nano crystals from a phase separated silicate glass. *J. Eur. Ceram. Soc.* 2013;33:1737–45.
- [497] de Pablos-Martín A, Durán A, Pascual MJ. Nanocrystallisation in oxyfluoride systems: mechanisms of crystallisation and photonic properties. *Int. Mater. Rev.* 2012;57:165–86.
- [498] Potapov OV, Fokin VM, Filipovich VN. Nucleation and crystal growth in water containing-soda lime-silica glasses. *J. Non-Cryst. Solids* 1999;247:74–8.
- [499] Wang T, Lu W, Xu X, Qiu J, Yu SF. Study of Crystallization and Coalescence of Nanocrystals in Amorphous Glass at High Temperature. *Inorg. Chem.* 2019;58:9500–4.
- [500] Sandu V, Cimpoiasu E, Greculeasa S, Kuncser A, Nicolescu MS, Kuncser V. Magnetite-based glass-ceramics prepared by controlled crystallization of borosilicate glasses: effect of nucleating agents on magnetic properties and relaxation. *Ceram. Inter.* 2017;43:3405–13.
- [501] Sandu V, Cimpoiasu E, Kuncser A, Nicolescu MS. Magnetic properties of glass-ceramics obtained by crystallization of iron-rich borosilicate glasses. *J. Adv. Ceram.* 2017;6:251–61.
- [502] Worsch C, Schaaf P, Harizanova R, Rüssel C. Magnetisation effects of multicore magnetic nanoparticles crystallised from a silicate glass. *J. Mater. Sci.* 2012;47:5886–90.
- [503] Büttner M, Schmidl F, Seidel P, Worsch C, Rüssel C. Multicore magnetic nanoparticles prepared by glass recrystallisation and magnetic properties. *J. Mater. Sci.* 2013;48:2299–307.
- [504] Chinnam RK, Francis AA, Will J, Bernardo E, Boccaccini AR. Functional glasses and glass-ceramics derived from iron rich waste and combination of industrial residues. *J. Non-Cryst. Solids* 2013;365:63–74.
- [505] Brown ASC, Hargreaves JSJ, Rijniers B. A study of the structural and catalytic effects of sulfation on iron oxide catalysts prepared from goethite and ferrihydrite precursors for methane oxidation. *Catal. Lett.* 1998;53:7–13.
- [506] Velasco MV, Souza MT, Crovace MC, de Oliveira AJA, Zanotto ED. Bioactive magnetic glass-ceramics for cancer treatment. *Biomed. Glasses* 2019;5:148–77.
- [507] Amirahmadi Z, Marghussian VK, Beitollahi A, Mirkazemi SM, Sarpoolaky H. Magnetite nanoparticles prepared by the crystallization of Na₂O–Fe₂O₃–B₂O₃–SiO₂ glasses. *J. Non-Cryst Solids* 2011;357:3195–9.
- [508] Miola M, Pakzad Y, Banijamali S, Kargozar S, Vitale-Brovvarone C, Yazdanpanah A, et al. Glass-ceramics for cancer treatment: so close, or yet so far? *Acta Biomater.* 2019;83:55–70.
- [509] Zheng W, Li Z, Zhang H, Wang W, Wang Y, Wang C. Electrospinning route for α-Fe₂O₃ ceramic nanofibers and their gas sensing properties. *Mater. Res. Bull.* 2009;44:1432–6.

- [510] Zboril R, Mashlan M, Petridis D. Iron(III) Oxides from thermal processes synthesis, structural and magnetic properties, Mössbauer spectroscopy characterization and applications. *Chem. Mater.* 2002;14:969–82.
- [511] de Pablos-Martin A, Patzig C, Höche T, Duran A, Pascual MJ. Distribution of thulium in Tm^{3+} -doped oxyfluoride glasses and glass-ceramics. *CrystEngComm* 2013;15:6979–85.
- [512] Barros JR, Bocker C, Rüssel C. The effect of Er^{3+} and Sm^{3+} on phase separation and crystallization in $\text{Na}_2\text{O}/\text{K}_2\text{O}/\text{BaF}_2/\text{BaO}/\text{Al}_2\text{O}_3/\text{SiO}_2$ glasses. *Solid State Sci.* 2010;12:2086–90.
- [513] Hoell A, Raghuwanshi VS, Bocker C, Herrmann A, Rüssel C, Höche T. Crystallization of BaF_2 from droplets of a phase separated glass-evidence of core-shell structure by SAXS. *CrystEngComm* 2020;22:5031–9.
- [514] Kokou L, Du J. Rare earth ion clustering behavior in europium doped silicate glasses: Simulation size and glass structure effect. *J. Non Cryst. Solids* 2012;358:3408–17.
- [515] Johnson JA, Benmore CJ, Holland D, Du J, Beuneu B, Mekki A. Influence of rare-earth ions on SiO_2 - Na_2O - RE_2O_3 glass structure. *J. Phys.: Condens. Matter* 2011;23:065404.
- [516] McGahay V, Tomozawa M. Phase-separation in rare-earth-doped SiO_2 glasses. *J. Non-Cryst. Solids* 1993;159:246–52.
- [517] Kuhn S, Herrmann A, Rüssel C. Quenching Behaviour of Sm^{3+} -Doped Lanthanum-Aluminium Silicate Glasses. *J. Lumin.* 2015;158:333–9.
- [518] Selvaraju K, Marimuthu K. Structural and spectroscopic studies on concentration dependent Sm^{3+} doped boro-tellurite glasses. *J. Alloys Comp.* 2013;553:273–81.
- [519] Kumar A, Rai DK, Rai SB. Optical properties of Sm^{3+} ions doped in tellurite glass. *Spectrochim. Acta A: Mol. Biomol. Spectrosc.* 2003;59:917–25.
- [520] Fernández-Rodríguez L, Balda R, Fernández J, Durán A, Pascual MJ. Structure and luminescent properties of Sm/Dy -doped $\text{Sr}_2\text{MgSi}_2\text{O}_7$ glass-ceramics. *Int. J. Appl. Glass Sci.* 2022;14:140–54.
- [521] Bocker C, Wiemert J, Rüssel C. The effect of viscosity on nano-crystallization of strontium fluoride from a silicate glass. *Solid State Sci.* 2014;38:55–60.
- [522] Fokin VM, Zanotto ED. Continuous compositional changes of crystal and liquid during crystallization of a sodium calcium silicate glass. *J. Non-Cryst. Solids* 2007;353:2459–68.
- [523] Potapov OV, Fokin VM, Ugoikov VL, Suslova LY, Filipovich VN. Influence of Na_2O content on the nucleation kinetics in glasses of compositions close to the $\text{Na}_2\text{O} \cdot 2\text{CaO} \cdot 3\text{SiO}_2$ stoichiometry. *Glass Phys. Chem.* 2000;26:27–32.
- [524] Fielitz P, Cassar DR, Yuritsyn NS, Abyzov AS, Fokin VM, Borchardt G, et al. Decelerated crystal growth in a soda-lime-silica glass. *J. Non-Cryst. Solids* 2022;596:121879.
- [525] Fokin VM, Potapov OV, Zanotto ED, Spiadorello FM, Ugolkov VL, Pevzner BZ. Mutant crystals in $\text{Na}_2\text{O} \cdot 2\text{CaO} \cdot 3\text{SiO}_2$ glasses. *J. Non-Cryst. Solids* 2003;331:240–53.
- [526] Kuhn S, Tiegel M, Herrmann A, Körner J, Seifert R, Yue F, et al. The effect of hydroxyl concentration on Yb^{3+} luminescence properties in a peraluminous lithium-alumino-silicate glass. *Opt. Mater. Exp.* 2015;5:430–40.
- [527] Peitl O, Zanotto ED, Heide K. Crystallization-triggered bubbles in glass-ceramics. *Ceram. Inter.* 2020;46:22513–20.
- [528] Davis MJ, Ihinger PD. Heterogeneous crystal nucleation on bubbles in silicate melt. *Am. Mineral.* 1998;83:1008–15.
- [529] Herrmann A, Rüssel C. A new route to an ordered array of bubbles formed during crystallization of glass. *Ceram. Int.* 2019;45:16666–9.
- [530] Braedt M, Frischat GH. Sodium self diffusion coefficients in alkali silicate melts as obtained by a microgravity experiment. *J. Am. Ceram. Soc.* 1984;67:C54–6.
- [531] Potapov OV, Fokin VM, Filipovich VN, Kalinina AM. Influence of water on the crystal nucleation and growth in the $\text{Na}_2\text{O} \cdot 2\text{CaO} \cdot 3\text{SiO}_2$ glass. *Glass Phys. Chem.* 1998;24:337–41.
- [532] Mackert Jr JR, Williams AL, Ergle JW, Russell CM. Water-enhanced crystallization of leucite in dental porcelain. *Dental Mater.* 2000;16:426–31.
- [533] Schairer JF, Bowen NL. The system $\text{K}_2\text{O}-\text{Al}_2\text{O}_3-\text{SiO}_2$. *Am. J. Sci.* 1955;253:681–746.
- [534] Davis MJ, Ihinger PD, Lasaga AC. Influence of water on nucleation kinetics in silicate melt. *J. Non-Cryst. Solids* 1997;219:62–9.
- [535] Dejneka MJ. The luminescence and structure of novel transparent oxyfluoride glass-ceramics. *J. Non-Cryst. Solids* 1998;239:149–55.
- [536] Wang Y, Ohwaki J. New transparent vitroceraamics codoped with Er^{3+} and Yb^{3+} for efficient frequency upconversion. *Appl. Phys. Lett.* 1993;63:3268–70.
- [537] Shinozaki K, Honma T, Oh-ishi K, Komatsu T. Morphology of CaF_2 nanocrystals and elastic properties in transparent oxyfluoride crystallized glasses. *Opt. Mater.* 2011;33:1350–6.
- [538] Lin C, Li L, Dai S, Liu C, Zhao Z, Bocker C, et al. Oxyfluoride glass-ceramics for transition metal ions based photonics: broadband near-IR luminescence of nickel ions dopant and nanocrystallization mechanism. *J. Phys. Chem. C* 2016;120:4556–63.
- [539] Gugov I, Müller M, Rüssel C. Transparent oxyfluoride glass-ceramics co-doped with Er^{3+} and Yb^{3+} -crystallization and up-conversion properties. *J. Solid State Chem.* 2011;184:1001–7.
- [540] Herrmann A, Tylkowski M, Bocker C, Rüssel C. Preparation and luminescence properties of glass-ceramics containing Sm^{3+} -doped hexagonal NaGdF_4 crystals. *J. Mater. Sci.* 2013;48:6262–8.
- [541] Bocker C, Bhattacharya S, Höche T, Rüssel C. Size distribution of nano crystallites in transparent glass-ceramics. *Acta. Mater.* 2009;57:5956–63.
- [542] Raghuwanshi VS, Hoell A, Bocker C, Rüssel C. Experimental evidence of a diffusion barrier around BaF_2 nano crystals in a silicate Glass by SAXS. *CrystEngComm* 2012;14:5215–23.
- [543] Lumeau J, Zanotto ED. A review of the photo-thermal mechanism and crystallization of photo-thermo-refractive (PTR) glass. *Intern. Mater. Rev.* 2017;62:348–66.
- [544] Lin C, Li L, Bocker C, Rüssel C. Preparation and structure of new oxyfluoride glass-ceramics containing BaLiF_3 nanocrystals. *J. Am. Ceram. Soc.* 2016;99:2878–81.
- [545] Chen D, Wang Y, Yu Y, Huang P. Intense ultraviolet upconversion luminescence from $\text{Tm}^{3+}/\text{Yb}^{3+}:\beta\text{-YF}_3$ nanocrystals embedded glass ceramic. *Appl. Phys. Lett.* 2007;91:51920.
- [546] Chen D, Wang Z, Zhou Y, Huang P, Ji Z. $\text{Tb}^{3+}/\text{Eu}^{3+}:\text{YF}_3$ nanophase embedded glass-ceramics: Structural characterization, tunable luminescence and temperature sensing behavior. *J. Alloys Comp.* 2015;646:339–44.
- [547] Meyneng T, Thomas J, Ledemi Y, Allix M, Veron E, Genevois C, et al. The role of fluorine in high quantum yield oxyfluoride glasses and glass-ceramics. *J. Alloys Comp.* 2022;900:163512.
- [548] Liu S, Chen D, Wan Z, Zhou Y, Huang P, Jia Z. Phase structure control and optical spectroscopy of rare-earth activated GdF_3 nanocrystal embedded glass-ceramics via alkaline-earth/alkali-metal doping. *RSC Adv.* 2016;6:71176.
- [549] Wurth R, Rüssel C. The crystallization of (Pb, Yb, Er) F_x nano particles from glasses with the composition $20\text{SiO}_2 \cdot 13.5\text{B}_2\text{O}_3 \cdot 6\text{Al}_2\text{O}_3 \cdot 10\text{PbO} \cdot 6.6\text{CaO} \cdot 20\text{PbF}_2 \cdot 13.3\text{CdF}_2 \cdot 10\text{YbF}_3 \cdot 0.5\text{ErF}_3$. *Solids State Sci* 2011;13:1132–6.
- [550] Haas S, Hoell A, Wurth R, Rüssel C, Boesecke P, Vainio U. Analysis of nano structure and nanochemistry by SAXS: a new approach to access phase compositions of oxyfluoride glass-ceramics doped with $\text{Er}^{3+}/\text{Yb}^{3+}$. *Phys. Rev. B.* 2010;81:184207.
- [551] Lakshminarayana G, Qiu J. Photoluminescence of Pr^{3+} , Sm^{3+} and Dy^{3+} : $\text{SiO}_2-\text{Al}_2\text{O}_3-\text{LiF}-\text{GdF}_3$ glass-ceramics and Sm^{3+} , Dy^{3+} : $\text{GeO}_2-\text{B}_2\text{O}_3-\text{ZnO}-\text{LaF}_3$ glasses. *Physica B* 2009;404:1169–80.
- [552] Truong NMP, Sedano M, Durán A, Balda R, Pascual MJ, Klement R. Er/Yb co-doped LiYF_4 transparent oxyfluoride glass-ceramics with up-conversion optical properties. *Ceram. Inter.* 2023;49:41202–9.
- [553] Velázquez JJ, Balda R, Fernández J, Gorni G, Sedano M, Durán A, et al. Structural and optical properties in $\text{Tm}^{3+}/\text{Tm}^{3+}-\text{Yb}^{3+}$ doped NaLuF_4 glass-ceramics. *Int. J. Appl. Glass Sci.* 2021;12:485–96.
- [554] Chen D, Zhou Y, Wan Z, Huang P, Yu H, Lu H, et al. Enhanced upconversion luminescence in phase-separation-controlled crystallization glass-ceramics containing Yb/Er(Tm): NaLuF_4 nanocrystals. *J. Eur. Ceram. Soc.* 2015;35:2129–37.
- [555] Wei Y, Liu X, Chi X, Wei R, Guo H. Intense upconversion in novel transparent $\text{NaLuF}_4:\text{Tb}^{3+}$, Yb^{3+} glass-ceramics. *J. Alloys Compd.* 2013;578:385–8.
- [556] de Pablos-Martin A, Méndez-Ramos J, del-Castillo J, Durán A, Rodríguez VD, Pascual MJ. Crystallization and up-conversion luminescence properties of $\text{Er}^{3+}/\text{Yb}^{3+}$ -doped NaYF_4 -based nano-glass-ceramics. *J. Eur. Ceram. Soc.* 2015;35:1831–40.

- [557] Gao Y, Chen J, Yang Y, Zhou D, Qiu J. Effect of glass-ceramics network intermediate Al_2O_3 content on up-conversion luminescence in $\text{Er}^{3+}/\text{Yb}^{3+}$ co-doped NaYF_4 oxy-fluoride glass-ceramics. *J. Eur. Ceram. Soc.* 2023;43:3591–9.
- [558] Niu Z, Yu B, Xu F, Jiang Y, Cai X, Hu J, et al. Color-tunable luminescence and temperature sensing in $\text{Ce}^{3+}/\text{Tb}^{3+}$ co-doped transparent oxyfluoride glass-ceramics containing $\text{Na}_{1.5}\text{Y}_{2.5}\text{F}_9$ nanocrystals. *J. Lumin.* 2022;246:118834.
- [559] Jiang Y, Chen C, Yu B, Li Q, Niu Z, Cai X, et al. Color tunable emission and temperature sensing performance in oxyfluoride glass ceramics containing $\text{Ce}^{3+}/\text{Dy}^{3+}$: $\text{Na}_5\text{Y}_9\text{F}_{32}$ nanocrystals. *J. Lumin.* 2023;256:119627.
- [560] Fu Y, Kang S, Guan S, Zhou G, Li S, Tan L, et al. Intense and broadband mid-infrared emission by nano-crystallization of rare-earth doped oxyfluoride glass-ceramic. *J. Alloys Comp.* 2022;900:163413.
- [561] Huang S, Gu M. Enhanced luminescent properties of Tb^{3+} ions in transparent glass-ceramics containing BaGdF_5 nanocrystals. *J. Non-Cryst. Solids* 2012;358:77–80.
- [562] Wu T, Zhao S, Lei R, Huang L, Xu S. Optical thermometry based on green upconversion emission in $\text{Er}^{3+}/\text{Yb}^{3+}$ codoped BaGdF_5 glass-ceramics. *Mater. Res. Express* 2018;5:025201.
- [563] Liu XY, Wei YL, Wei RF, Yang JW, Guo H. Elaboration, structure, and luminescence of Eu^{3+} -doped BaLuF_5 -based transparent glass-ceramics. *J. Am. Ceram. Soc.* 2013;96:798–800.
- [564] Li Y, Wang W, Pan Y, Chen H, Cao Q, Wei X. Upconversion luminescence and optical thermometry properties of transparent oxyfluoride glass ceramics embedded with $\text{Ba}_4\text{Y}_3\text{F}_{17}$: Yb^{3+} , Er^{3+} nanocrystals. *CrystEngComm* 2020;22:6302–9.
- [565] Ai B, Liu C, Wang J, Xie J, Han J, Zhao X. Precipitation and optical properties of CsPbBr_3 quantum dots in phosphate glasses. *J. Am. Ceram. Soc.* 2016;99:2875–7.
- [566] Ai B, Liu C, Deng Z, Wang J, Hana J, Zhao X. Low temperature photoluminescence properties of CsPbBr_3 quantum dots embedded in glasses. *Phys.Chem.Chem. Phys.* 2017;19:17349.
- [567] Wei K, Li P, Duan Y, Zhang S, Chen L, Xu S, et al. Temperature-dependent color-tunable luminescence in CsPbBr_3 : Dy^{3+} glass ceramic. *J. Non-Cryst. Solids* 2021;570:121022.
- [568] Cheng Y, Shen C, Shen L, Xiang W, Liang X. Tb^{3+} , Eu^{3+} co-doped CsPbBr_3 QDs glass with highly stable and luminous adjustable for white LEDs. *ACS Appl. Mater. Interfaces* 2018;10:21434–44.
- [569] Yuan S, Chen D, Li X, Zhong J, Xu X. In Situ crystallization synthesis of CsPbBr_3 perovskite quantum dot-embedded glasses with improved stability for solid-state lighting and random upconverted lasing. *ACS Appl. Mater. Interfaces* 2018;10:18918–26.
- [570] Liu S, Luo Y, He M, Liang X, Xiang W. Novel CsPbI_3 QDs glass with chemical stability and optical properties. *J. Eur. Ceram. Soc.* 2018;38:1998–2004.
- [571] Stoica M, Brehl M, Bocker C, Herrmann A, Rüssel C. Microstructure and luminescence of erbium doped $\text{Na}_2\text{O}/\text{K}_2\text{O}/\text{CaF}_2/\text{Al}_2\text{O}_3/\text{SiO}_2$ nano glass-ceramics. *Mater. Chem. Phys.* 2018;207:36–43.
- [572] Lee H, Lee J, Chung WJ, Im WB. Modifying the composition of oxyfluoride glass-ceramics containing Eu^{2+} -doped nepheline and LaF_3 crystals for white LED. *Optical Mater.* 2023;137:113550.
- [573] Liu X, Zhou J, Zhou S, Yue Y, Qiu J. Transparent glass-ceramics functionalized by dispersed crystals. *Prog. Mater. Sci.* 2018;97:38–96.
- [574] Xue J, Wang X, Jeong JH, Yan X. Fabrication, photoluminescence and applications of quantum dots embedded glass ceramics. *Chem. Eng. J.* 2020;383:123082.
- [575] He M, Jia J, Zhao J, Qiao X, Du J, Fan X. Glass-ceramic phosphors for solid state lighting: a review. *Ceram. Int.* 2021;47:2963–80.
- [576] Galante R, Figueiredo-Pina GC, Serro AP. Additive manufacturing of ceramics for dental applications: A review. *Dental Mater.* 2019;35:825–46.
- [577] Cruz ME, Sedano M, Castro Y, Pascual MJ, Fernández J, Balda R, et al. Rare-earth doped transparent oxyfluoride glass-ceramics: processing is the key. *Opt. Mater. Express* 2022;12:3493–516.
- [578] Woltz S, Rüssel C. Self organized nano crystallinity of magnetite precipitated from a 4.9 Na_2O 33.2 CaO 17.1 Fe_2O_3 44.7 B_2O_3 glass. *J. Non-Cryst. Solids* 2004;337:226–31.
- [579] <https://github.com/epam/SciGlass>, 17.11.2022.
- [580] Rüssel C. Self diffusion of polyvalent ions in a soda-lime-silica glass melt. *J. Non-Cryst. Solids* 1991;134:169–75.
- [581] Bartenev GM, Sanditow DS, Rasumowskaja IV, Lukyanow IA. Molecular kinetic processes in inorganic glass melts in the transformation range. *Silikattechnik* 1972;23:155–9.
- [582] Selsing J. Internal stresses in ceramics. *J. Am. Ceram. Soc.* 1961;44:419.
- [583] J. M. Aroni, G. H. Klöb, C. Rüssel, Stresses around spherical particles, calculated by FEM and measured using polarization microscopy. *Glass Sci. Technol.* 75 C2 (2002) 426–429.
- [584] Moynihan CT, Lee S-K, Tatsumisago M, Minami T. Estimation of activation energies for structural relaxation and viscous flow from DTA and DSC experiments. *Thermochim. Acta* 1996;280(281):153–62.
- [585] Li S, Zhou Y, Duan H, Qiu J, Zhang Y. Joining of SiC ceramic to Ni-based superalloy with functionally gradient material fillers and a tungsten intermediate layer. *J. Mater. Sci.* 2003;38:4065–70.
- [586] Bocker C, Funke C, Rüssel C. Strengthening of a zinc silicate glass by surface crystallization. *Mater. Lett.* 2017;207:41–3.
- [587] Stookey SD, Olcott JS, Garfinkel HM, Rothermel DL. in: *Advances in glass technology*. New York: Plenum; 1962. p. 397–411.
- [588] Partridge G, McMillan PV. Strengthening of glass by surface crystallization. *Glass Technol.* 1974;15:127–33.
- [589] Priller S, Frischat GH, Pye LD. Strengthening of glass through surface crystallization of β -spodumene ss. *J. Non-Cryst. Solids* 1996;196:144–9.
- [590] Petticrew RW, Schott CE, Smith WE. Art of producing high-strength, surface crystallized, glassbodies. *US* 1965;3,490,984.
- [591] Pressau JP. Method for producing surface compression in certain glasses by promoting random surface crystallization. *US* 1964;3,464,807.
- [592] Rinehart DW, Heights N. Surface crystallized glass and method of producing. *US* 1963;3,464,880.
- [593] Kiefer W, Sack W, Krause D. Making surface crystallized glass bodies and resulting product. *US* 1973;3,907,577.
- [594] Fabris DCN, Miguel EH, Vargas R, Canto RB, Villas-Boas MDOC, Peitl O, et al. Microstructure, residual stresses, and mechanical performance of surface crystallized translucent glass-ceramics. *J. Eur. Ceram. Soc.* 2022;42:4631–42.
- [595] Guldiren D, Erdem I, Aydin S. Influence of silver and potassium ion exchange on physical and mechanical properties of soda lime glass. *J. Non-Cryst. Solids* 2016;441:1–9.
- [596] Shaisha EE, Cooper AR. Ion exchange of soda-lime glass with univalent cations. *J. Am. Ceram. Soc.* 1981;64:278–83.
- [597] Kistler SS. Stresses in glass produced by nonuniform exchange of monovalent ions. *J. Am. Ceram. Soc.* 1962;45:59–68.
- [598] Gomez S, Dejneka MJ, Ellison AJ, Rossington KR. Look at the chemical strengthening process: alkali aluminosilicate vs. soda-lime glass 2011;Vol. 32:61–6.
- [599] Choi YS, Yun JU, Park SE. Flat panel display glass: current status and future. *J. Non Cryst. Solids* 2016;431:2–7.
- [600] Lange FF. Fracture energy and strength behavior of a sodium borosilicate glass- Al_2O_3 composite system. *J. Am. Ceram. Soc.* 1971;54:614–20.
- [601] Aitken JE, Ladbroke PH, Potok N. Microwave measurement of the temperature coefficient of permittivity for sapphire and alumina (short papers). *IEEE Trans. Microw. Theory and Tech.* 1975;23:526–9.
- [602] Sproull JF, Rindone GE. Correlation between strength of glass and glassy microphases. *J. Am. Ceram. Soc.* 1973;56:102–3.
- [603] Watanabe M, Moriya T. Consideration of relation between mechanical behavior of glasses and their internal structure. *Rev. Elec. Commun. Lab.* 1961;9:50–71.
- [604] Qu L, Chosakabey KL, Wheatley R. Enhanced doping effects of multielement on anisotropic thermal expansion in ZrO_2 with new compositions. *J. Am. Ceram. Soc.* 2020;103:5881–90.
- [605] Zhou Y, Yu Z, Zhao N, Shi C, Liu E, Du X, et al. Microstructure and properties of in situ generated MgAl_2O_4 spinel whisker reinforced aluminum matrix composites. *Mater. Design* 2013;46:724–30.
- [606] Kerstan M, Müller M, Rüssel C. Thermal expansion of $\text{Ba}_2\text{ZnSiO}_7$, BaZnSiO_4 and the solid solution series $\text{BaZn}_{2-x}\text{Mg}_x\text{SiO}_2$ ($0 \leq x \leq 2$) studied by high temperature X-ray diffraction and dilatometry. *J. Solid State Chem.* 2012;188:84–91.
- [607] Roberts RB, White GK. Thermal expansion of fluorites at high temperatures. *J. Phys. C: Solid State Phys.* 1986;19:7167–72.
- [608] Hinz W. Silikate. Berlin: VEB Verlag für Bauwesen; 1970.

- [609] Szabo I. Crystallization of magnesium aluminosilicate glasses. *J. Non-Cryst. Solids* 1997;219:128–35.
- [610] Avramov I, Völksch G. Near-surface crystallization of cordierite glass. *J. Non-Cryst. Solids* 2002;304:25–30.
- [611] Reinsch S, Nascimento MLE, Müller R, Zanotto ED. Crystal growth kinetics in cordierite and diopside glasses in wide temperature ranges. *J. Non-Cryst. Solids* 2008;354:5386–94.
- [612] Völksch G, Heide K. Dissolved gases and minor component effects on glass crystallization. *J. Non-Cryst. Solids* 1997;219:119–27.
- [613] Katsura T, Wakihara M, Hara S-I, Sugihara T. Some thermodynamic properties in spinel solid solutions with the Fe_3O_4 component. *J. Solid State Chem.* 1975;13:107–13.
- [614] Petric A, Jacob KT. Thermodynamic Properties of $\text{Fe}_3\text{O}_4\text{-FeV}_2\text{O}_4$ and $\text{Fe}_3\text{O}_4\text{-FeCr}_2\text{O}_4$ Spinel Solid Solutions. *J. Am. Ceram. Soc.* 1982;65:117–23.
- [615] Petrova M, Mikirticheva G, Novikova A, Popova V. Spinel solid solutions in the systems $\text{MgAl}_2\text{O}_4\text{-ZnAl}_2\text{O}_4$ and $\text{MgAl}_2\text{O}_4\text{-Mg}_2\text{TiO}_4$. *J. Mater. Res.* 1997;12:2584–8.
- [616] Jacob KT, Alcock CB. Activities and their relation to cation distribution in $\text{NiAl}_2\text{O}_4\text{-MgAl}_2\text{O}_4$ spinel solid solutions. *J. Solid State Chem.* 1977;20:79–88.
- [617] Kemei MC, Moffitt SL, Darago LE, Seshadri R, Suchomel MR, Shoemaker DP, et al. Structural ground states of $(\text{A},\text{A}')\text{Cr}_2\text{O}_4$ ($\text{A}=\text{Mg},\text{Zn}$; $\text{A}'=\text{Co},\text{Cu}$) spinel solid solutions: Spin-Jahn-Teller and Jahn-Teller effects. *Phys. Rev. B* 2014;89:174410.
- [618] Jacob KT, Fitzner K. Ion-exchange equilibria between $(\text{Mn}, \text{Co})\text{O}$ solid solution and $(\text{Mn}, \text{Co})\text{Cr}_2\text{O}_4$ and $(\text{Mn}, \text{Co})\text{Al}_2\text{O}_4$ spinel solid solutions at 1100° C. *J. Mater. Sci.* 1977;12:481–8.
- [619] Hirakawa T, Shimokawa Y, Tokuzumi W, Sato T, Tsushida M, Yoshida H, et al. Multicomponent spinel oxide solid solutions: a possible alternative to platinum group metal three-way catalysts. *ACS Catal.* 2019;9:11763–73.
- [620] Navrotsky A. Thermodynamics of $\text{A}_3\text{O}_4\text{-B}_3\text{O}_4$ spinel solid solutions. *J. Inorg. Nucl. Chem.* 1969;31:59–72.
- [621] Alcántara R, Jaraba M, Lavela P, Tirado JL. New $\text{LiNi}_y\text{Co}_{1-2y}\text{Mn}_{1+y}\text{O}_4$ spinel oxide solid solutions as 5 V electrode material for Li - Ion batteries. *J. Electrochem. Soc.* 2003;151:A53.
- [622] Sakoda K, Hirano M. Formation of complete solid solutions, $\text{Zn}(\text{Al}_x\text{Ga}_{1-x})_2\text{O}_4$ spinel nanocrystals via hydrothermal route. *Ceram. Inter.* 2014;40:15841–8.
- [623] DeVries RC, Roy R. Phase equilibria in the system $\text{BaTiO}_3\text{—CaTiO}_3$. *J. Am. Ceram. Soc.* 1955;38:142–6.
- [624] Muta H, Kurosaki K, Yamanaka S. Thermoelectric properties of doped $\text{BaTiO}_3\text{—SrTiO}_3$ solid solution. *J. Alloys Comp.* 2004;368:22–4.
- [625] Shirane G, Takeda A. Phase transitions in solid solutions of PbZrO_3 and PbTiO_3 (I) small concentrations of PbTiO_3 . *J. Phys. Soc. Japan* 1952;7:5–11.
- [626] Ning Z, Jiang Y, Jian J, Guo J, Cheng J, Cheng H, et al. Achieving both large piezoelectric constant and high Curie temperature in $\text{BiFeO}_3\text{-PbTiO}_3\text{-BaTiO}_3$ solid solution. *J. Eur. Ceram. Soc.* 2020;40:2338–44.
- [627] Isupov VA. Nonlinearity of the concentration dependence of the Curie temperature in ferroelectric perovskite solid solutions. *Phys. Stat. Solidi A* 2000;181:211–8.
- [628] Bera J, Rout SK. On the formation mechanism of $\text{BaTiO}_3\text{—BaZrO}_3$ solid solution through solid-oxide reaction. *Mater. Lett.* 2005;59:135–8.
- [629] Aydi A, Simon A, Michau D, von der Mühll R, Abdelmoula N, Khemakhem H. Elaboration and dielectric study of ferroelectric or relaxor ceramics in the ternary system $\text{BaTiO}_3\text{—NaNbO}_3\text{—BaSnO}_3$. *J. Alloys Comp.* 2011;509:7773–7.
- [630] Coffeen WW. Dielectric bodies in the quaternary system $\text{BaTiO}_3\text{—BaSnO}_3\text{—SrSnO}_3\text{—CaSnO}_3$. *J. Am. Ceram. Soc.* 1953;36:215–21.
- [631] Toyoda K, Kato T, Sakabe Y. Re-examination of the phase transitions in BaTiO_3 -based solid solutions. *Ferroelectrics* 1990;108:227–32.
- [632] Bratton RJ, Tien TY. Phase transitions in the system $\text{BaTiO}_3\text{-KNbO}_3$. *J. Am. Ceram. Soc.* 1967;50:90–3.
- [633] Aoyagi R, Rinaldi R, Sumiyama N, Iwata M, Maeda M. Electrical properties and phase transition behavior of $(\text{Li},\text{Na},\text{Ba})(\text{Nb},\text{Ti})\text{O}_3$ lead-free piezoelectric ceramics. *Key Eng. Mater.* 2009;421–422:42–5.
- [634] Qiao H, He C, Wang Z, Li X, Liu Y, Long X. Improved electrical properties of BaTiO_3 modified $\text{BiScO}_3\text{-PbTiO}_3$ ceramics with high Curie temperature. *Ceram. Int.* 2017;43:11463–8.
- [635] Morrison FD, Coats AM, Sinclair DC, West AR. Charge compensation mechanisms in La-Doped BaTiO_3 . *J. Electroceram.* 2001;6:219–32.
- [636] Kishi H, Kohzu N, Sugino J, Ohsato H, Iguchi Y, Okuda T. The effect of rare-earth (La, Sm, Dy, Ho and Er) and Mg on the microstructure in BaTiO_3 . *J. Eur. Ceram. Soc.* 1999;19:1043–6.
- [637] Makovec D, Samardžija Z, Drogenik M. Solid solubility of holmium, yttrium, and dysprosium in BaTiO_3 . *J. Am. Ceram. Soc.* 2004;87:1324–9.
- [638] Zhang H, Jo W, Wang K, Webber KG. Compositional dependence of dielectric and ferroelectric properties in $\text{BiFeO}_3\text{—BaTiO}_3$ solid solutions. *Ceram. Int.* 2014;40:4759–65.
- [639] Döhler F, Zschechel T, Kasch S, Schmidt T, Rüssel C. A glass in the system $\text{CaO/MgO/Al}_2\text{O}_3\text{/SiO}_2$ and the rapid laser sealing of alumina. *Ceram. Int.* 2017;43:4302–8.
- [640] Orsini PG, Buri A, Marotta A. Devitrification of glasses in the akermanite-gehlenite system. *J. Am. Ceram. Soc.* 1975;58:306–11.
- [641] Ventura JMG, Tulyaganov DU, Agathopoulos S, Ferreira JMF. Sintering and crystallization of akermanite-based glass-ceramics. *Mater. Lett.* 2006;60:1488–91.
- [642] Swainson IP, Dove MT, Schmahl WW, Putnis A. Neutron powder diffraction study of the akermanite-gehlenite solid-solution series. *Phys. Chem. Min.* 1992;19:185–95.
- [643] Merlini M, Gemmi M, Artioli G. Thermal expansion and phase transitions in åkermanite and gehlenite. *Phys. Chem. Min.* 2005;32:189–96.
- [644] Morioka M, Kamata Y, Nagasawa H. Diffusion in single crystals of melilite: III. Divalent cations in gehlenite. *Geochim. Cosmochim. Acta* 1997;61:1009–16.
- [645] Morioka M, Nagasawa H. Diffusion in single crystals of melilite: II. Cations. *Geochim. Cosmochim. Acta* 1991;55:751–9.
- [646] Thieme C, Rüssel C. Negative thermal expansion in $\text{Ba}_{0.5}\text{Sr}_{0.5}\text{Zn}_2\text{SiGeO}_7$. *Mater.* 2016;9:631.
- [647] Tyagi AK, Achary SN, Mathews MD. Phase transition and negative thermal expansion in $\text{A}_2(\text{MoO}_4)_3$ system ($\text{A}=\text{Fe}, \text{Cr}$ and Al). *J. Alloys Comp.* 2002;339:207–10.
- [648] Gilbu B, Fjellvag H, Kjekshus A. Properties of $\text{LaCo}_{1-x}\text{Cr}_x\text{O}_3$. *Acta Chem. Scand.* 1994;48:37–45.
- [649] Chesson DA, Zhu JH. Effect of off-stoichiometry on electrical conductivity in Ni-Fe and Mn-Co spinel systems. *J. Electrochem. Soc.* 2020;167:124515.
- [650] Paknahad P, Askari M, Ghorbanzadeh M. Characterization of nanocrystalline CuCo_2O_4 spinel prepared by sol-gel technique applicable to the SOFC interconnect coating. *Appl. Phys. A* 2015;119:727–34.
- [651] Xiao J, Zhang W, Xiong C, Chi B, Pu J, Jian L. Oxidation behavior of Cu-doped MnCo_2O_4 spinel coating on ferritic stainless steels for solid oxide fuel cell interconnects. *Int. J. Hydrogen Energy* 2016;41:9611–8.
- [652] Dugué A, Dymshits O, Cormier L, Loiko P, Alekseeva I, Tsenter M, et al. Structural transformations and spectroscopic properties of Ni-doped magnesium aluminosilicate glass-ceramics nucleated by a mixture of TiO_2 and ZrO_2 for broadband near-IR light emission. *J. Alloys Comp.* 2019;780:137–46.
- [653] Dymshits OS, Bukina VS, Ereemeev KN, Alekseeva IP, Tsenter MY, Khubetsov AA, et al. Spectral properties and structure of transparent glass-ceramics based on $\text{Fe:MgAl}_2\text{O}_4$ and $\text{Fe:ZnAl}_2\text{O}_4$ crystals. *J. Opt. Technol.* 2021;88:323–9.
- [654] Basyrova L, Bukina V, Balabanov S, Belyaev A, Drobotenko V, Dymshits O, et al. Synthesis, structure and spectroscopy of $\text{Fe}_{2+}:\text{MgAl}_2\text{O}_4$ transparent ceramics and glass-ceramics. *J. Lumin.* 2021;236:118090.
- [655] Glazunov IV, Malyarevich AM, Yumashev KV, Dymshits OS, Alekseeva IP, Tsenter MY, et al. Linear and non-linear optical properties of transparent glass-ceramics based on Co^{2+} -doped $\text{Zn}(\text{Al},\text{Ga})_2\text{O}_4$ spinel nanocrystals. *J. Non-Cryst. Solids* 2021;557:120627.
- [656] Stryak AJ, McMillan PW. Microstructure and properties of transparent glass-ceramics Part 1 The microstructure of spinel/transparent glass-ceramics. *J. Mater. Sci.* 1978;13:1275–81.
- [657] Barb D, Bărbulescu E, Bărbulescu A. Diffuse phase transitions and ferroelectric- paraelectric diagram for the $\text{BaTiO}_3\text{-SrTiO}_3$ system. *Phys. Stat. Sol.* 1982;74:79–83.
- [658] Kim SW, Choi HI, Lee MH, Park JS, Kim DJ, Do D, et al. Electrical properties and phase of $\text{BaTiO}_3\text{-SrTiO}_3$ solid solution. *Ceram. Inter.* 2013;39:S487–90.
- [659] Mathews T, Jacob KT. Seebeck coefficient of magnetite: a reinterpretation invoking Jahn-Teller entropy. *Solid State Commun.* 1992;84:975–8.
- [660] Dong J, Suwardi A, Tan XY, Jia N, Saglik K, Ji R, et al. Challenges and opportunities in low-dimensional thermoelectric nanomaterials. *Mater. Today* 2023;66:137–57.

- [661] Dubrovin V, Nikonorov N, Ignatiev A. Bromide photo-thermo-refractive glass for volume Bragg gratings and waveguide structure recording. *Opt. Mater. Express* 2017;7:425–30.
- [662] Dubrovin VD, Ignatiev AI, Nikonorov NV. Chloride photo-thermo-refractive glasses. *Opt. Mater. Express* 2016;6:1701–13.
- [663] Shinozaki K, Ishii Y, Sukenaga S, Ohara K. Ultrafast nanocrystallization of BaF₂ in oxyfluoride glasses with crystal-like nanostructures: implications for upconversion fiber devices. *ACS Appl. Nano Mater.* 2022;5:4281–92.
- [664] Xu X, Wen Z, Yang X, Zhang J, Gu Z. High lithium ion conductivity glass-ceramics in Li₂O–Al₂O₃–TiO₂–P₂O₅ from nanoscaled glassy powders by mechanical milling. *Solid State Ionics* 2006;177:2611–5.
- [665] Mariappan CR, Gellert M, Yada C, Rosciano F, Roling B. Grain boundary resistance of fast lithium ion conductors: comparison between a lithium-ion conductive Li–Al–Ti–P–O-type glass ceramic and a Li_{1.5}Al_{0.5}Ge_{1.5}P₃O₁₂ ceramic. *Electrochem. Commun.* 2012;14:25–8.
- [666] Ahmad N, Zhou L, Faheem M, Tufail MK, Yang L, Chen R, et al. Enhanced air stability and high Li-ion conductivity of Li_{6.988}P_{2.994}Nb_{0.2}S_{10.934}O_{0.6} glass–ceramic electrolyte for all-solid-state lithium–sulfur batteries. *ACS Appl. Mater. Interf.* 2020;12:21548–58.
- [667] Hammel JJ. Direct measurements of homogeneous nucleation rates in a glass-forming system. *J. Chem. Phys.* 1967;46:2234–44.
- [668] Hill RG, Goat C, Wood D. Thermal analysis of a SiO₂–Al₂O₃–CaO–CaF₂ glass. *J. Am. Ceram. Soc.* 1992;75:778–85.
- [669] Jin M, Zhou W, Ma W, Wang Q, Liang X, Zhang P, et al. The inhibition of CsPbBr₃ nanocrystals glass from self-crystallization with the assistance of ZnO modulation for rewritable data storage. *Chem. Eng. J.* 2022;427:129812.
- [670] Hu F, Chen W, Jiang Y, Song W, Wei R, Guo H. Tm³⁺-doped Na_{0.5-x}Yb_{0.5+x}F_{2+2x} self-crystallization glass-ceramics: Microstructure and optical thermometry properties. *J. Lumin.* 2019;214:116558.
- [671] Wan Z, Che D, Zhou Y, Huang P, Zhong J, Ding M, et al. Eu³⁺ and Er³⁺ doped NaLu_{1-x}Yb_xF₄ (x=0–1) solid-solution self-crystallization nano-glass-ceramics: Microstructure and optical spectroscopy. *J. Eur. Ceram. Soc.* 2015;35:3673–9.
- [672] Cao JK, Li XM, Wang ZX, Wei YL, Chen LP, Guo H. Optical thermometry based on up-conversion luminescence behavior of self-crystallized K₃YF₆:Er³⁺ glass-ceramics. *Sens. Actuators B: Chemical* 2016;224:507–13.
- [673] Guo L, Xin H, Li Y, Yu Y, Yan Z, Hu C, et al. Self-crystallization characteristics of calcium-magnesium-alumina-silicate (CMAS) glass under simulated conditions for thermal barrier coating applications. *J. Eur. Ceram. Soc.* 2020;40:5683–91.
- [674] Vogel W, Hoeland W, Naumann K, Gummel J. Development of machineable bioactive glass ceramics for medical uses. *Journal of non-crystalline solids* 1986; 80:34–51.
- [675] Vogel W. Phase separation in glass. *Journal of Non-Crystalline Solids* 1977;25:170–214.
- [676] Bussey JM, Weber MH, Smith-Gray NJ, Sly JJ, McCloy JS. Examining phase separation and crystallization in glasses with X-ray nano-computed tomography. *Journal of Non-Crystalline Solids* 2023;600:121987.